

**DOCTORAL THESIS**

**PROPOSAL OF SOUNDNESS ASSESSMENT METHOD OF REINFORCED  
CONCRETE STRUCTURES AFFECTED BY CARBONATION**

(炭酸化の影響を受けた鉄筋コンクリート構造物の健全性評価法の提案)

A Dissertation Presented

by

LUGE CHENG

成 璐 哿

せい れか

Submitted to the Graduate Department of the Architecture  
University of Tokyo in partial fulfillment  
of the requirements for the degree of

DOCTOR OF ENGINEERING

Directed by: Professor Ippei Maruyama

July 2022

Cheng Luge

[chengluge@g.ecc.u-tokyo.ac.jp](mailto:chengluge@g.ecc.u-tokyo.ac.jp)

sugurs\_20@hotmail.com

Graduate Department of the Architecture School of Engineering

The University of Tokyo

Building Material Engineering Lab.

B04 room

Engineering Bldg.1, 7 Chome-3-1 Hongo, Bunkyo City,

Tokyo, Japan, 113-8654.

Reviewer:

Prof. Ippei Maruyama

Co-reviewer:

Prof. Takafumi Noguchi

Prof. Tetsuya Ishida

Prof. Kazuo Yamada

Prof. Manabu Kanematsu



© Copyright by Cheng Luge 2022

All Rights Reserved

## ACKNOWLEDGMENTS

I would like to express my sincere gratitude to my supervisor Prof. Ippei MARUYAMA for your continuous support during my PhD course, and also your patience, enthusiasm, and immense knowledge. You always discussed and analyzed the research results with me patiently, gave me very constructive advice, and carefully guided me in conducting experiment and writing the academic papers, which made me grow and improve a lot than I imaged during these three years. I got many opportunities from you to participate in the academic research activities and communicate with excellent researchers, which helped me broaden my horizons and knowledge. As an excellent and leading researcher in the concrete research field, you never hesitated to praise my progress which always encouraged me along my PhD course. And your passion for research has gradually affected me, making me realize the enjoyment and meaning of doing research more and more, which will keep encouraging me in my career in the future.

I would also like to address my gratitude to Prof. Takafumi NOGUCHI for your precious guidance and valuable advice during my research. Thank you for giving me the opportunity to study in the University of Tokyo and accepting me as a member in BME laboratory, which changed my life and future totally.

Also, thanks to Prof. Kazuo YAMADA for your precious suggestions and insightful comments to improving this research work.

Thanks to Assoc. Prof. Atsushi TOMOYOSE and technical staff Masamichi TAMURA for aiding my experiment design, managing the affairs of the laboratory and creating an ideal research environment for us.

Many additional thanks to all my fellows for creating a good and pleasant working atmosphere. In particular, I want to thank Dr. Ryo KURIHARA, Dayoung OH, Daiki SAWA, Yajie YAN, Yuqi REN and Shota UMEKI for your advice, support and friendship.

A big thank goes to my boyfriend Xinghai LIANG for always being willing to take the time to check my research papers with your brilliant mind. Thank you so much for believing in me, pushing me forward and making me belly laugh when I needed it the most. And also, thanks to my best friend Biqing Jian for your patience in listening, it gave me a lot of courage and confidence Thank you to all my friends!

To my supportive, loving parents, Wu CHENG and Qingfang CHENG, thank you for everything you have gone through and sacrificed for. Thank you for raising me to be the person I am today. Another big thank you goes to my lovely sister Xiaolu CHENG for always staying with me, and encouraging me when I feel depressed.

Finally, I would like to thank myself for always staying healthy and always having a strong and optimistic mind that has kept me going so far.

A part of this study was supported by the Environment Research and Technology Development Fund (S-18-4(2) JPMEERF20S11816) of the Ministry of the Environment, Japan.

これからもよろしく申し上げます。

WORK HARD! STAY HUMBLE!

## TABLE OF CONTENTS

DOCTORAL THESIS .....	1
ACKNOWLEDGMENTS .....	iv
TABLE OF CONTENTS.....	v
LIST OF TABLES.....	ix
LIST OF FIGURES .....	x
1. INTRODUCTION .....	1
1.1 Background.....	1
1.2 Objective and scope of the research.....	4
1.3 Dissertation outline .....	5
2. LITERATURE REVIEW OF CARBONATION-INDUCED CORROSION.....	7
2.1 Concrete carbonation .....	7
2.2 Depassivation and corrosion mechanisms .....	8
2.3 Corrosion rate prediction methods for the propagation phase of the corrosion process.....	12
2.4 Summary .....	18
3. EFFECT OF RELATIVE HUMIDITY AND TEMPERATURE ON STEEL CORROSION IN CARBONATED MORTAR.....	20
3.1 Introduction.....	20
3.2 Experimental procedureaa .....	22

3.2.1 Material .....	22
3.2.2 Specimen design .....	23
3.2.3 Accelerated carbonation and environmental condition control .....	25
3.2.4 Electrochemical measurements .....	27
3.2.5 Microstructure of mortar .....	32
3.3 Experimental results .....	33
3.3.1 Electrical resistivity of carbonated mortar .....	33
3.3.2 The corrosion rate of steel rebar in carbonated mortar .....	34
3.3.3 Corrosion potential of steel rebar in carbonated mortar .....	36
3.3.4 Microstructure characterization of mortar .....	37
3.4 Discussion .....	39
3.4.1 Effect of RH and temperature on the electrical resistivity of carbonated mortar .....	39
3.4.2 Effect of RH and temperature on corrosion rate of steel rebar .....	44
3.4.3 Corrosion controlling mechanism of carbonation-induced corrosion .....	48
3.5 Summary .....	52
4. EFFECT OF COVER THICKNESS ON CARBONATION-INDUCED CORROSION RATE .....	55
4.1 Introduction .....	55
4.2 Experimental procedure .....	56
4.2.1 Material and specimen .....	56

4.2.2 Accelerated carbonation and environmental condition control .....	57
4.2.3 Electrochemical measurement .....	57
4.3 Experimental results of corrosion rate of steel rebar in the carbonated mortar with different cover thicknesses.....	58
4.4 Discussion .....	61
4.4.1 Effect of RH and temperature on corrosion rate with different cover thicknesses .....	61
4.4.2 Prediction of corrosion rate considering the cover thickness .....	62
4.5 Summary .....	64
5. VERIFICATION OF CORROSION RATE PREDICTION EQUATION BY CARBONATED SLAG-BASED MORTAR .....	65
5.1 Overview .....	65
5.2 Experimental procedure .....	65
5.2.1 Materials and proportions .....	65
5.2.2 Sample preparation and environment control .....	67
5.2.3 Electrochemical measurement .....	67
5.2.4 Characterization of Materials.....	67
5.3 Experimental results and discussion .....	69
5.3.1 Mortar properties .....	69
5.3.2 Electrochemical results of carbonated SCM-based mortar.....	72



5.3.3 Calculated results and measured results of the electrical resistivity of mortar and corrosion rate of rebar .....	72
5.4 Summary .....	78
6. SOUNDNESS ASSESSMENT FOR RC STRUCTURES.....	79
6.1 Motivations .....	79
6.2 Assessment object.....	79
6.3 Soundness assessment process.....	81
6.4 An example of residual service life of RC structure.....	93
6.5 Summary .....	105
7. CONCLUSIONS AND RECOMMENDATIONS FOR FUTURE WORK.....	106
7.1 Overview of contributions and conclusions.....	106
7.2 Originality .....	107
7.3 Recommendations for future work .....	108
APPENDIX A CARBONATION DEPTH CONFIRMATION AND CARBONATION DEGREES CALCULATED BY X-RAY DIFFRACTION (XRD)/RIETVELD ANALYSIS.....	109
APPENDIX B SATURATION DEGREE OF CARBONATED MORTAR AT DIFFERENT RH AND TEMPERATURE CONDITIONS .....	113
APPENDIX C EFFECT OF RH AND TEMPERATURE ON STEEL CORROSION IN CHLORIDE-CONTAINING MORTAR—COMPARISON WITH CARBONATION-INDUCED CORROSION.....	114
C.1 Experimental procedure .....	114

C.1.1 Material and specimen .....	114
C.1.2 Environmental condition control.....	115
C.1.3 Electrochemical measurements .....	115
C.1.4 Microstructure of chloride-containing mortar.....	116
C.2 Experiment Results .....	116
C.2.1 Electrical resistivity of chloride-containing mortar .....	116
C.2.2 Microstructure characterization of chloride-containing mortar .....	117
C.3 Discussion .....	124
C.3.1 The electrical resistivity of chloride-containing mortar.....	124
C.3.2 Prediction of electrical resistivity of chloride-containing mortar under different environmental conditions .....	126
C.3.3 Effect of RH and temperature on chloride-induced corrosion rate .....	129
C.4 Summary .....	136
APPENDIX D THE ESTIMATION OF CORROSION RATE OF STEEL REBAR IN CARBONATED MORTAR DURING RAINFALL.....	138
REFERENCE.....	139

## LIST OF TABLES

Table 2.1 Initial assumed parameters and main coefficient values at each model .....	17
Table 3.1 Chemical composition of ordinary Portland cement. ....	22
Table 3.2 Mineral composition of ordinary Portland cement. ....	22
Table 3.3 Mix proportion of mortar .....	22
Table 3.4 Chemical composition and mechanical properties of steel material used ...	25
Table 3.5 Relative humidity in the presence of saturated solution at 20 °C. ....	27
Table 4.1 The standard minimum cover thickness in RC members in JASS 5[96].....	55
Table 4.2 The standard minimum cover thickness in RC members in JSCE[97].....	55
Table 4.3 Mix proportions of mortar .....	56
Table 5.1 Chemical Compositions (%) of the Portland cement and blast-furnace slag .....	66
Table 5.2 Mineral Composition (wt%) of Ordinary Portland Cement .....	66
Table 5.3 Mortar mix proportion of slag-based mortar .....	66
Table 5.4 Initial values of $R_0$ and the calculated apparent activation energy $E_{app}$ for carbonated slag-based mortar .....	73
Table 5.5 Comparison between measured weight loss and corrosion amount calculated from $i_{corr}$ .....	77
Table 6.1 Elements and properties to be considered in selecting survey sites[113]....	82
Table 6.2 Deterioration states, countermeasures, and standard construction methods[97][114].....	83

Table 6.3 Setting value of $P_0$ considering the number of years of durability .....	87
Table 6.4 Finishing conditions for the exterior concrete members .....	95
Table 6.5 Maximum $CO_2$ concentration results in interior rooms.....	95
Table 6.6 Investigating results of cover thickness and carbonation depth .....	96
Table 6.7 Calculated parameters of cover thickness and carbonation depth of exterior and interior concrete members.....	96
Table 6.8 The duration of the corrosion initiation probability reached to limit value ( $t_p$ ) for each concrete member.....	98
Table 6.9 Water content of concrete near the steel rebar.....	98
Table 6.10 Standard values of unit coarse aggregate bulk volume for sand and gravel concrete for OPC.....	99
Table 6.11 Water content of mortar near the steel rebar.....	99
Table 6.12 Initial electrical resistivity ( $R_0$ ) of each concrete member.....	99
Table 6.13 The limited corrosion amount of each concrete member .....	103
Table 6.14 Corrosion amount evolution at the service life of every concrete member .....	104
Table 6.15 Residual service life of every concrete member.....	105
Table A.1 Phase composition determined through XRD/Rietveld analysis of the cement paste (mass%). .....	110
Table A.2 Carbonation degrees calculated from XRD and DTG .....	112
Table C.1 Mix proportion of chloride-containing mortar .....	115

Table D.1 The corrosion rate of steel rebar of each concrete member during rainfall days .....	138
--	-----

## LIST OF FIGURES

Figure 1.1 Schematic illustration of the service life of RC structure.....	3
Figure 1.2 Structure of the dissertation outline.....	6
Figure 2.1 A schematic illustration of the corrosion process in concrete .....	8
Figure 2.2 Relative Volumes of corrosion products .....	10
Figure 2.3 Degraded RC members in Gunkanjima Island, Nagasaki, Japan .....	11
Figure 2.4 Sequence of the carbonation-induced corrosion and degradation of RC structures .....	11
Figure 2.5 Corrosion state assessment according to different electrical resistivity of concrete .....	15
Figure 2.6 Calculated corrosion rate deduced from the empirical models .....	18
Figure 3.1 Polypropylene fiber .....	23
Figure 3.2 Steel rebar treatment process.....	24
Figure 3.3 The schematic diagram of the mortar specimen.....	25
Figure 3.4. Experiment process .....	26
Figure 3.5 Experimental setup of three-electrode cell setup for corrosion rate measurements.....	28
Figure 3.6 Physical models (a) and corresponding electrical circuit (b) for rebar in mortar.....	28
Figure 3.7 LCR arrangement for two-point electrical measurement .....	30
Figure 3.8 Randles electronic circuit for rebar in mortar.....	31

Figure 3.9 Setup of sample in the water bath.....	32
Figure 3.10 Range of pore sizes seen in different measurement techniques .....	33
Figure 3.11 Electrical resistivity of carbonated mortar at different RH and temperature conditions.....	34
Figure 3.12 Relationship of corrosion rate of steel rebar and RH in the carbonated mortar under variable temperature conditions .....	35
Figure 3.13 Relationship of corrosion rate of steel rebar and RH in the carbonated mortar under variable temperature conditions .....	35
Figure 3.14 The correlation between the corrosion rate and corrosion potential of steel rebar in the carbonated mortar under different temperatures for each RH condition (error bars represent the measured range).....	36
Figure 3.15 Pore size distribution and cumulative porosity of carbonated mortar and non-carbonated mortar .....	37
Figure 3.16 Water vapor sorption isotherms (a) and pore size distribution (b) determined from the water adsorption branch .....	38
Figure 3.17 Water content of carbonated mortar at different RH and temperature conditions.....	39
Figure 3.18 The role water content plays in electrical resistivity of mortar .....	41
Figure 3.19 Relationship of electrical resistivity and water content in the carbonated mortar under variable temperature conditions .....	41
Figure 3.20 Arrhenius plots of electrical resistivity of carbonated mortar .....	43
Figure 3.21 Relationship of corrosion rate of steel rebar and water content in the carbonated under variable temperature conditions .....	44

Figure 3.22 Steel rebar removed from carbonated mortar under 68% RH, 97% RH and 20 °C, 40 °C .....	47
Figure 3.23 Corrosion products removal procedure following standard systematic step .....	47
Figure 3.24 Steel corrosion propagation in concrete .....	48
Figure 3.25 Evans diagrams of the corrosion processes controlled by resistive control(a) and cathodic control(b) .....	49
Figure 3.26 Relationship between reciprocal of electrical resistivity and corrosion rate in carbonated mortar .....	50
Figure 3.27 Relationship between reciprocal of electrical resistivity and corrosion rate .....	51
Figure 4.1 The schematic diagram of the mortar specimen with different cover thicknesses .....	56
Figure 4.2 Mortar samples taped by waterproof tape .....	57
Figure 4.3 Setup of sample in water heating bath.....	58
Figure 4.4 Corrosion rate of rebar with different cover thicknesses under different RH conditions under 20°C.....	59
Figure 4.5 Relationship between corrosion rate and RH with four cover thicknesses	59
Figure 4.6 Relationship between corrosion rate and temperature with four cover thicknesses .....	60
Figure 4.7 Effect of cover thickness on corrosion rate under different RH and temperature conditions.....	60
Figure 4.8 Corrosion rate under 97%RH and 40°C with allometric fitted curve.....	62



Figure 5.1 Hydration degrees of cement and slag in 30SL and 70SL after 60 days' curing period .....	69
Figure 5.2 Water content of carbonated 30SL, 50SL, 60SL and 70SL at different RH conditions.....	70
Figure 5.3 Relationship between electrical resistivity of carbonated slag-based mortars and RH under different temperature conditions.....	71
Figure 5.4 Relationship between corrosion rate of steel rebar and RH under different temperature conditions.....	72
Figure 5.5 Electrical resistivity of carbonated slag-based mortar at different water content under 20°C.....	73
Figure 5.6 Comparison of measured electrical resistivity and predicted electrical resistivity.....	74
Figure 5.7 Comparison of measured corrosion rate and predicted corrosion rate (measured corrosion rate was overestimated by electrochemical measurement due to the oxidation of sulphide species).....	75
Figure 5.8 Steel rebar removed from the carbonated 60SL (a), 70SL(b) and OPC (c) mortar under 97%RH and 40°C .....	75
Figure 5.9 Comparison of modified corrosion rate and predicted corrosion rate .....	77
Figure 6.1 Deterioration evolution of RC buildings .....	80
Figure 6.2 Overall soundness assessment process flow.....	81
Figure 6.3 The relationship between the distribution of the carbonation depth progression over time and the distribution of the cover thickness.....	85
Figure 6.4 Carbonation depth progression and cover thickness .....	86

Figure 6.5 Difference between distribution of carbonation depth and cover thickness .....	87
Figure 6.6 Schematic configuration of two-point measurement.....	88
Figure 6.7 Schematic configuration of four-point measurement .....	89
Figure 6.8 A conceptual diagram of service life of RC buildings from carbonation progress .....	91
Figure 6.9 Summary of soundness assessment process .....	92
Figure 6.10 Average temperature every month in Tokyo per year.....	93
Figure 6.11 Average rainy days in Tokyo .....	94
Figure 6.12 Corrosion initiation probability evolution with time for each concrete member .....	97
Figure 6.13 Predicted electrical resistivity of concrete members every month.....	100
Figure 6.14 Predicted corrosion rate of steel rebar of concrete members every month at the first year .....	100
Figure 6.15 Predicted corrosion rate of steel rebar of concrete members every month at the second year.....	101
Figure 6.16 Predicted corrosion amount of steel rebar of concrete members every month at the first year (a) and second year (b).....	102
Figure 6.17 Corrosion amount evolution with age of every concrete member .....	103
Figure A.1 Cross-sections ( $20 \times 20 \text{ mm}^2$ ) of reference mortar specimens sprayed with 1% phenolphthalein solution: (a)non-carbonated; (b) carbonated.....	109
Figure A.2 Diffraction patterns of non-carbonated and carbonated mortar samples.	110

Figure A.3 DTG curves for the non-carbonated and carbonated mortar with the main decompositions labeled .....	112
Figure B.1 Pore saturation degrees of carbonated mortar at different RH and temperature conditions .....	113
Figure C.1 Electrical resistivity of chloride-containing mortar at different RH and temperature conditions .....	116
Figure C.2 Pore size distribution and cumulative porosity of chloride-containing mortar and carbonated mortar .....	117
Figure C.3 Water content of chloride-containing mortar at different RH and temperature conditions .....	118
Figure C.4 Pore saturation degrees of chloride-containing mortar at different RH and temperature conditions .....	119
Figure C.5 Relationship of corrosion rate of steel rebar and RH in the chloride-containing mortar under variable temperature conditions .....	119
Figure C.6 Relationship of corrosion rate of steel rebar and temperature in the chloride-containing mortar under variable RH conditions .....	120
Figure C.7 The correlation between the corrosion rate and corrosion potential of steel rebar in the chloride-containing mortar under different temperatures for each RH condition (error bars represent the measured range) .....	121
Figure C.8 BSE image at the steel/concrete interface in the chloride-containing mortar (a) and carbonated mortar. ....	123
Figure C.9 Relationship of electrical resistivity and water content in the chloride-containing mortar under variable temperature conditions .....	125

Figure C.10 Electrical resistivity of carbonated mortar saturated by sodium chloride solution with a concentration of 3.8% (consistent with the mix proportion in Table C.1 Mix proportion of chloride-containing mortar) and ionized water .....	126
Figure C.11 Arrhenius plots of electrical resistivity of chloride-containing mortars	127
Figure C.12 Relationship of corrosion rate of steel rebar and water content in the chloride-containing mortar (b) under variable temperature conditions .....	129
Figure C.13 Nyquist plots of steel rebar in chloride-containing mortar under 97% RH condition with the controlled temperature of 20 °C and 50 °C .....	131
Figure C.14 Steel rebar removed from chloride-containing mortar under 68% RH, 97% RH and 20 °C, 40 °C .....	132
Figure C.15 Relationship between reciprocal of electrical resistivity and corrosion rate in chloride-containing mortar .....	134
Figure C.16 Relationship between reciprocal of electrical resistivity and corrosion rate .....	135
Figure D.1 Corrosion rate evolution during the cyclic wetting-and-drying cycles ...	138

## INTRODUCTION

### 1. INTRODUCTION

#### 1.1 Background

Cement-based materials are composed of binder (hydrated cement) and aggregates of different compositions with different sizes. Cement is produced by heating a mixture of limestone and raw clay minerals[1]. Ordinary Portland Cement (OPC) has been the most commonly used cement in the world in the past decades, and other cement types have been designed to lower carbon dioxide emissions to ensure sustainable concrete production. Due to their high mechanical strength, concrete and cement-based materials are widely used in civil and industrial structures. Reinforcement with steel rebar can improve the performance of structural elements without modifying the macroscopic cementitious matrix properties. Reinforced concrete (RC) is a kind of highly durable material as the concrete is a protective barrier for the steel reinforcing bars (rebars), which allows the development of RC structures, such as buildings, bridges, dams, or nuclear power plants. However, such materials deteriorate over time, causing the consumption of energy and materials in the societal and economic fields due to the maintenance and repairment.

The corrosion of steel rebars, one of the most common causes of degradation of RC structures, has received increasing attention in recent decades[2]. The corrosion of steel rebar is initiated by the influence of aggressive agents, including chloride( $Cl^-$ ) and carbon dioxide( $CO_2$ )[3]. The degradation of the protective layer formed on steel rebar surface in sound concrete results in accelerated corrosion, affecting the performance of RC structures progressively. The resulting corrosion products precipitate and then generate tensile stress, promoting the appearance of cracks to an unacceptable level regarding their service life[4]. Such a deterioration process frequently causes significant structural problems and eventually collapse of RC structures[5]. When the first cracks are noticed on the concrete surface, corrosion has generally reached an advanced stage, and maintenance action is required. Premature degradation concerns the safety and quality of human life; the repair work also negatively affects the environment[6].

## INTRODUCTION

The energy and material cost due to the corrosion in RC structures are caused by a severe lack of fundamental and clear understanding of corrosion-related degradation exposed to the widely variable exposure situations, the different controlling mechanisms of the corrosion process, the insufficient engineering application in the field, and the gap between laboratory and real conditions. The engineering strategies dealing with degraded RC structures rely on experience and are mainly empirical. On the other hand, the cost-effective maintenance of aging RC structures and new sustainable structures increase the demand for achieving sustainable development goals[7]. Therefore, a knowledge-based approach, reliable durability assessments, and service-life predictions of RC structures are necessary, which are crucial for monitoring the performance and determining the maintenance planning of existing RC structures and designing durable and sustainable new RC structures.

A well-known schematic service life model of RC structures was proposed by Tutti [5], as shown in Figure 1.1, which distinguishes between two stages: the initiation stage describes the transport of the corrosive agents through the concrete to the steel until conditions are met for corrosion initiation, and the propagation stage describes the process of corrosion and accumulation of related damage until a limit state is reached, and thus the end of the service life is reached. During the initiation stage, in the case of carbonated concrete, it is generally assumed that corrosion is initiated as the carbonation front reaches the steel rebar with a pH value lower than 10. In the case of chloride-induced corrosion, a critical chloride content with a limited chloride concentration ( $C_{th}$ ) on the steel rebar surface was proposed to be associated with corrosion initiation[8][9][10][11][12]. On the other hand, the propagation stage can be described as an electro-chemical process involving anodic dissolution of iron and cathodic oxygen reduction with a pore solution in concrete acting as the electrolyte. Precipitation of corrosion products in the concrete pores caused by this electro-chemical process may give rise to expansion stress and lead to concrete cracking. The occurrence of cracks is undesirable because it usually causes the people's panic and promotes further ingress of species that may trigger additional deterioration, which leads to the final state of concrete degradation: concrete spalling. Since the period between cracking

## INTRODUCTION

occurrence and final state of concrete degradation is short, corrosion-induced cracking is considered as the limit state in service life.

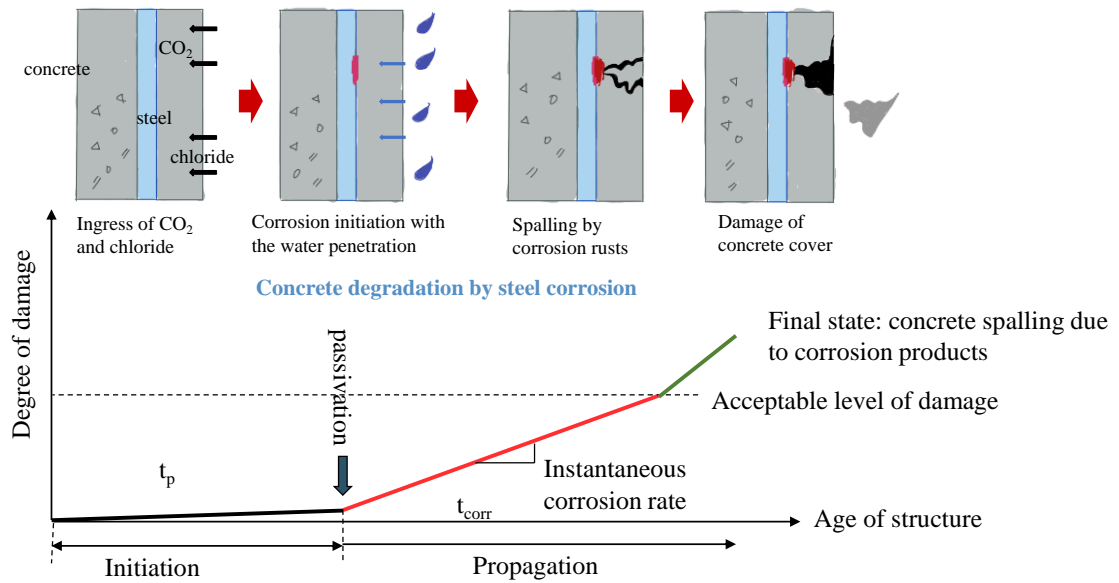


Figure 1.1 Schematic illustration of the service life of RC structure

Because the chemical degradation of concrete owing to chloride ingress or carbonation is well known, the depassivation initiation period in terms of pH decrease and chloride concentration has been accurately investigated by many researchers [13][14][15][16]. In the *Standard Specifications for Concrete Structures* [17] published by the Japan Society of Civil Engineers, advanced reactive transport models based on carbon dioxide and chloride ion diffusion and penetration were established to predict the carbonation front and chloride concentration on the steel surface with a maximum water-soluble chloride ion content ( $C_{th}$ ), which can be calculated according to the water-to-cement ratio(w/c), through the concrete cover.

Currently, the service life of carbonated RC structures and chloride-containing RC structures was predicted by probabilistic carbonation assessment method and critical chloride content prediction only considering the initiation phase. However, at the end of the initiation phase, the RC structure may still have adequate residual serviceability and strength. Furthermore, the propagation phase in the corrosion-inhibited conditions (lack of chloride content or carbon dioxide, dry condition, etc.) may be sufficiently long

## INTRODUCTION

and hence be part of the service life of RC structures. Therefore, to meet the durability requirements of corrosion-affected RC structures, service life prediction after the initiation phase is now receiving more attention. As a result, there have been trends towards extending the service life definition of RC structures prone to steel corrosion.

In fact, by far most of the research addressed carbonation of the cementitious phases and only a few studies focused on the related corrosion behavior during the propagation stage of service life[2]. Evaluating the corrosion rate of steel rebars in concrete during the propagation stage is challenging because the mechanism controlling the corrosion process is not well understood.

### **1.2 Objective and scope of the research**

The purpose of this study is mainly focusing on the carbonation-induced corrosion in RC structures and propose a prediction method of corrosion rate of steel rebar in carbonated mortar based on the corrosion controlling mechanisms under variable controlling environmental conditions, and propose a soundness assessment for RC structures with the consideration phase of the corrosion process. Therefore, the main objectives of this study are:

- To clarify the carbonation-induced corrosion behaviors under different environmental conditions based on the change of electrical resistivity of mortar, corrosion potentials, and corrosion rate of steel rebar.
- To clarify the corrosion controlling mechanisms in the viewpoint of the electrochemical and cement chemistry under specific environmental conditions.
- To propose a prediction method of carbonation-induced corrosion rate according to the corrosion controlling mechanisms with different relative humidity (RH) and temperature conditions.
- To clarify the effect of cover depth on corrosion behavior of steel rebar and propose a more accurate and theoretically meaningful prediction method of corrosion rate.



## INTRODUCTION

- To verify the prediction method of carbonation-induced corrosion rate by the measured corrosion results of steel rebar embedded in supplementary cementitious materials.
- To propose a feasible soundness assessment of RC structures considering the effect of carbonation.

This study contributes to the evaluation of the soundness and service life of RC structures considering the effect of carbonation in a more reliable theory-based way. It should be understood that the limitation is set up for corrosion of RC structures focused on the effect of carbonation, mainly considering the effect of environmental factors including RH and temperature. The effect of chloride content on corrosion behaviors as an additional content is in APPENDIX C.

### 1.3 Dissertation outline

The structures of the dissertation outline are shown in Figure 1.2, which is divided into eight chapters as explained as follows:

**Chapter 1** provides an introduction intending to present the background of this study as well as the objectives.

**Chapter 2** gives a theoretical background about the carbonation of concrete and carbonation-induced corrosion. In addition, the proposed corrosion rate prediction models were reviewed.

**Chapter 3** provides the results and discussion about the RH and temperature dependence of carbonation-induced corrosion and clarifies the corrosion controlling mechanisms under specific exposure conditions. A prediction method for corrosion rate was proposed, which is helpful in evaluating the soundness and the service life of RC members affected by carbonation.

## INTRODUCTION

**Chapter 4** clarifies the effect of cover thickness on corrosion behaviors of steel rebar and proposes a more accurate and reliable prediction method of corrosion rate considering the different cover thicknesses in real cases.

**Chapter 5** is to verify the proposed corrosion rate prediction method by using the electrochemical results of steel rebar embedded in supplementary cementitious materials.

**Chapter 6** provides a feasible soundness assessment process for real RC structures based on the proposed corrosion rate prediction method in this study and existing Japan standard specifications.

**Chapter 7** conveys a summary, conclusions, and recommendations for research work in the future.

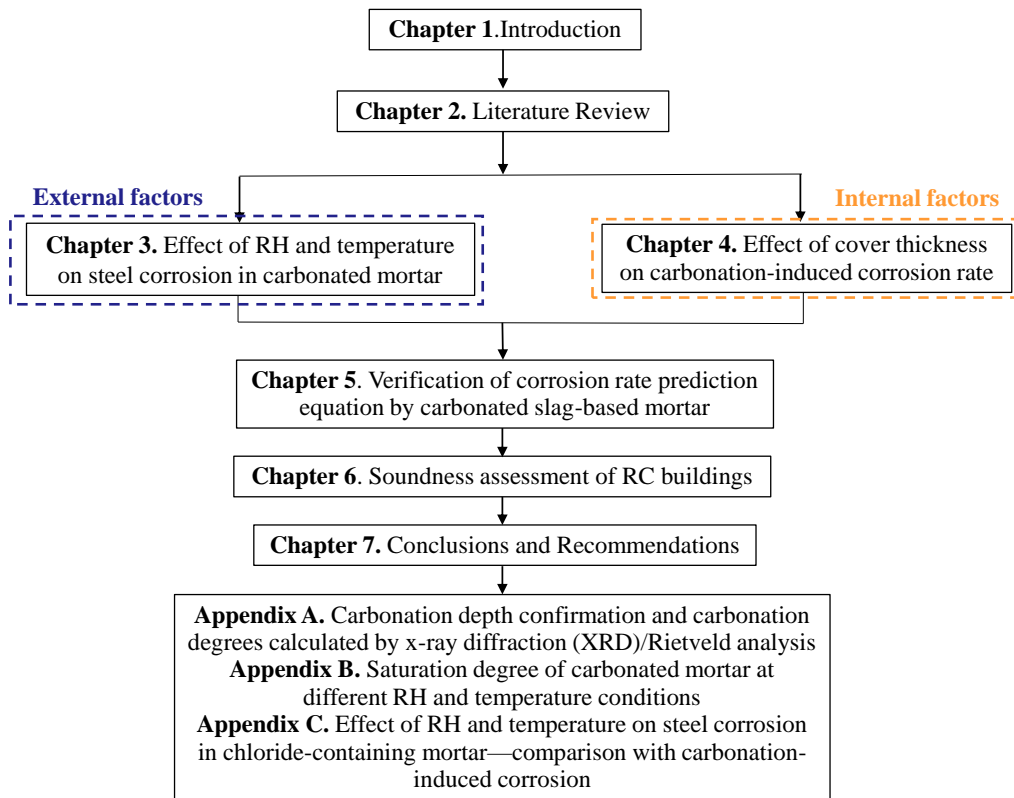


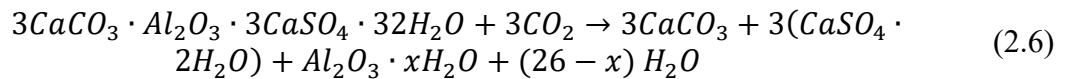
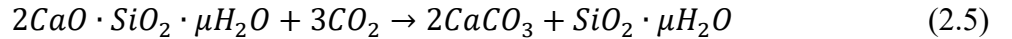
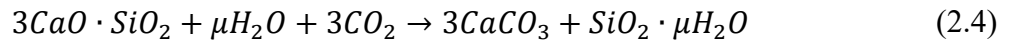
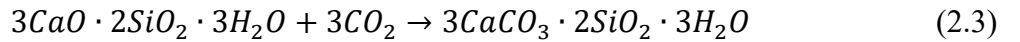
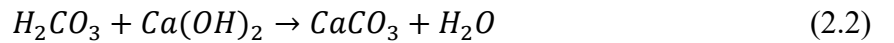
Figure 1.2 Structure of the dissertation outline

## 2. LITERATURE REVIEW OF CARBONATION-INDUCED CORROSION

### 2.1 Concrete carbonation

The carbonation of concrete has attracted more attention due to global climate change[18]. Carbonation of concrete in realistic conditions takes place in a low process mainly due to the low concentration of carbon dioxide ( $CO_2$ ) in the atmosphere of 0.03% to 0.04%, but will be faster in urban, industrial environments, and people gathered interior where the rise in  $CO_2$  concentration is higher than 0.04%[19][20]. Nevertheless, it eventually leads to the initiation of corrosion of the embedded steel rebar and subsequently the corrosion propagation, resulting in corrosion-induced damage, including delamination, cover cracking, and spalling. Therefore, it deserves much attention, especially when considering the durability design of RC structures, especially in metropolitan areas[21].

Carbonation of concrete is the chemical reaction involving the dissolution of  $CO_2$  in the form of weak carbonic acid ( $H_2CO_3$ ) and calcium hydroxide (portlandite,  $Ca(OH)_2$ ) in the pore solution, resulting in the precipitation of mostly calcium carbonate (calcite,  $CaCO_3$ ) in the concrete pores as shown in Eqs. (2.1) and (2.2).



## LITERATURE REVIEW OF CARBONATION-INDUCED CORROSION

Depletion of hydroxyl ions ( $\text{OH}^-$ ) lowers the pore water pH from above 12.5 to 9.0. Other calcium-bearing phases ( $\text{C-S-H}$ ,  $\text{C}_2\text{S}$  and  $\text{C}_3\text{S}$ ) are also susceptible to carbonation, as shown in Eqs. (2.3)-(2.6), and possible products include aragonite and vaterite[22][23]. Besides, ettringite and aluminate decomposed upon reaction with  $\text{CO}_2$ , resulting in formation of gypsum and alumina gel as shown in Eq. (2.6) [24].

### 2.2 Depassivation and corrosion mechanisms

Concrete usually provides a non-aggressive environment for steel rebar, and the steel rebar in concrete is protected against corrosion by a stable passive film due to the high alkalinity of the pore solution [18]. Such passivation is initiated by the formation of adsorbed substances ( $\text{FeOH}$  and  $\text{Fe}(\text{OH})^-$ ),  $\text{FeO}_2^-$  and  $\text{Fe}(\text{OH})_2$ [19], and the aging of such passive film results in a progressive decrease of corrosion rate, which is attributable to the thickening of the film, leading to the oxidation of magnetite  $\text{Fe}_3\text{O}_4$  to  $\text{Fe}(\text{III})$  oxide and oxyhydroxide ( $\text{Fe}_2\text{O}_3$  or  $\text{FeOOH}$ )[20][21][22].

However, as the thickness of the passive film is only tens of angstroms [23], it can be easily destroyed by the carbonation of the medium. Carbonation depletes the hydroxyl ions in the alkaline concrete pore solution. It, therefore, leads to a reduction of pH (loss of alkalinity) in carbonated concrete from 12.5 to as low as 9.0. The drop in pH leads

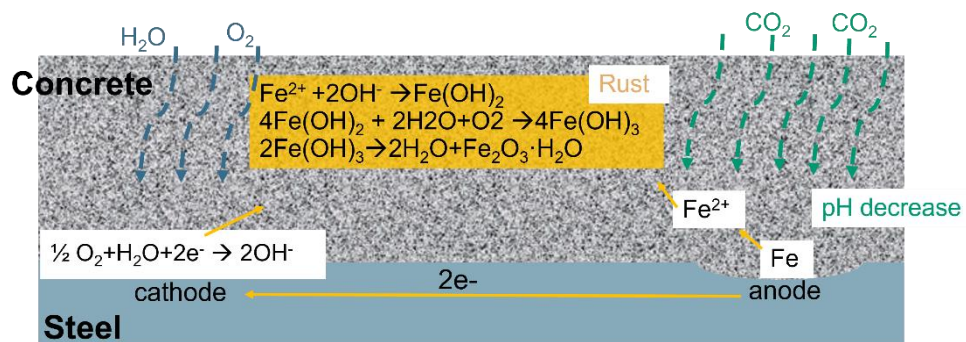
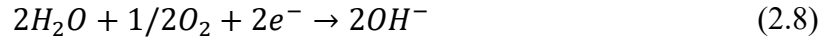


Figure 2.1 A schematic illustration of the corrosion process in concrete

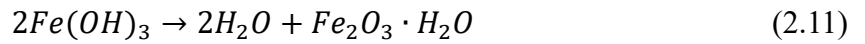
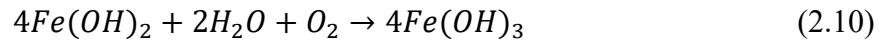
## LITERATURE REVIEW OF CARBONATION-INDUCED CORROSION

to the destruction of the thin protective film on the steel surface and significantly increases the risk of steel corrosion initiation.

The corrosion of steel reinforcement in concrete is an electrochemical process [24] and comprises two half-cell reactions: anodic and cathodic. The different electro-chemical potentials on the steel rebar surface lead to separate anodic and cathodic sites, as shown in Figure 2.1. At the anodic site, electrons are produced, associated with the dissolution of iron (Eq. (2.7)); electrons are consumed, and hydroxyl ions are produced as a result of the reduction of oxygen at the cathodic site (Eq. (2.8)):



$Fe^{2+}$  ions react within the pore solution to form common rust. The following reactions (Eqs. (2.9) to (2.11)) represent the formation of the so-called red rust ( $Fe_2O_3$ ) after iron dissolution occurs at the anodic sites on the reinforcement:



Besides the red rust, other types of rust formed in corrosion have a significant impact on the cracking and spalling of concrete surrounding the reinforcement due to the different volume expansion of corrosion products, as shown in Figure 2.2 [25][26]. The typical examples of the cracking and spalling behavior in corrosion-induced RC member degradation are shown in Figure 2.3.

## LITERATURE REVIEW OF CARBONATION-INDUCED CORROSION

The mechanisms and kinetics of the corrosion of steel rebar in concrete are usually assessed in terms of various electrochemical indicators, namely, the electrical resistivity of concrete ( $R_\Omega$ ), corrosion potential ( $E_{\text{corr}}$ ), and corrosion rate ( $i_{\text{corr}}$ ) of steel rebar.

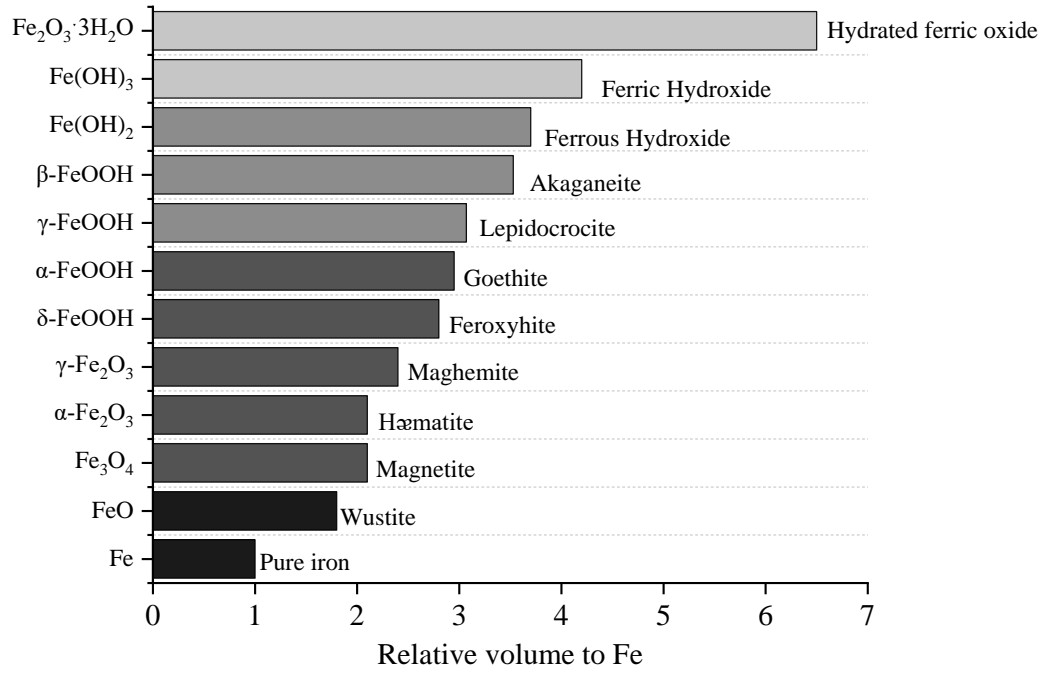


Figure 2.2 Relative Volumes of corrosion products

The concrete electrical resistivity indicates the ease or difficulty of the flow of corrosion current. The corrosion potential, also called an open circuit or rest or half-cell potential, is used as a qualitative index for ascertaining the corrosion risk. The corrosion rate, usually expressed in terms of corrosion current density, is a quantitative index representing an overall estimate of the rate of corrosion attack on the reinforcement.

As described above, Figure 2.4 Sequence of the carbonation-induced corrosion and degradation of RC structures summarizes the sequence of the carbonation-induced corrosion and degradation of RC structures, including the carbonation penetrating from the concrete surface, corrosion of steel rebar initiated due to the decrease of pH, corrosion propagation of steel rebar, and degradation of RC structure caused by accelerated corrosion products.



Figure 2.3 Degraded RC members in Gunkanjima Island, Nagasaki, Japan

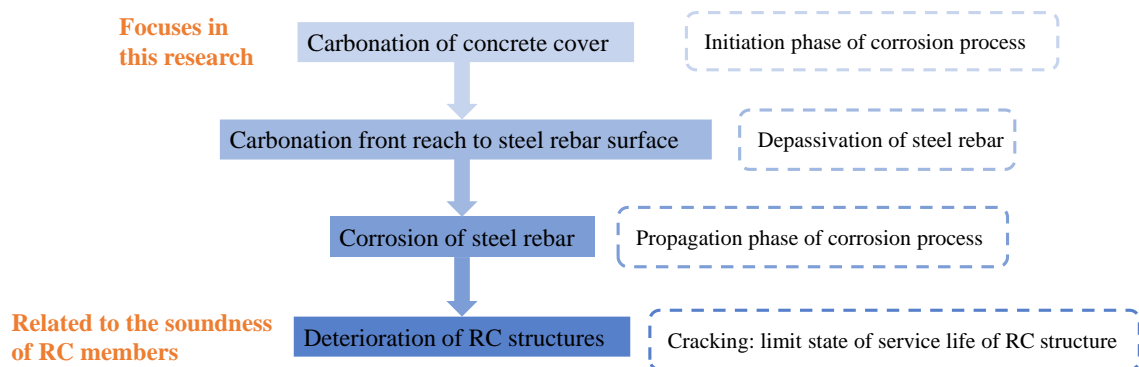


Figure 2.4 Sequence of the carbonation-induced corrosion and degradation of RC structures

### 2.3 Corrosion rate prediction methods for the propagation phase of the corrosion process

In the past study, models have been developed to predict the progress of carbonation front in concrete to predict the time to steel corrosion initiation[27][28][29]. However, the studies on the propagation phase prediction are still lacking, and this study is trying to fill this gap.

Some different forecast models estimating the service life have been introduced, including empirical and numerical models.

Empirical models are based on direct relationships between basic parameters of the concrete properties or the exposed environment and measured corrosion rate without considering the mechanism of the corrosion process.

Morinaga[30] proposed an empirical equation for the corrosion rate based on the analysis of experimental results, considering the carbonation-induced corrosion, and environmental conditions with input parameters w/c ratio, the diameter of reinforcing steel, cover depth as the internal factors, and relative humidity, temperature, oxygen concentration as the external factors. The derived carbonation-induced corrosion rate prediction equation: was presented as:

$$i_{corr} = 21.84 - 1.35X_1 - 35.43X_2 - 234.76X_3 + 2.33X_4 + 4.42X_5 + 250.55X_6 \quad (2.12)$$

where,

$i_{corr}$ : rate of corrosion due to carbonation ( $10^{-4}$  g/cm<sup>2</sup>/year),

$X_1$ : temperature (°C),

$X_2$ : relative humidity (%/100),

$X_3$ : oxygen concentration (%/100),

$X_4$ :  $X_1 \times X_2$  (interaction between  $X_1$  and  $X_2$ ),

$X_5$ :  $X_1 \times X_3$  (interaction between  $X_1$  and  $X_3$ ),

$X_6$ :  $X_2 \times X_3$  (interaction between  $X_2$  and  $X_3$ ).



## LITERATURE REVIEW OF CARBONATION-INDUCED CORROSION

Ahmad and Bhattacharjee[31] developed a prediction model for chloride-induced corrosion rate of the steel rebar under normal exposure at an early age, considering the main factors of w/c ratio, cement content, and the chloride content of concrete. A standard statistical experimental design was adopted to evaluate the simultaneous effects of these factors on steel rebar corrosion, and the possible interaction was identified through analysis of variance (*ANOVA*). The empirical models for corrosion rate were fitted in terms of the effective factors and interactions, using the method of least squares. The original treatment levels of cement content (*A*), w/c ratio (*B*), and a chloride content (*C*) were reduced to simplified coded levels as 1, 0, and +1, through the following relationships:

$$A = \frac{\text{cement content}(kg/m^3) - 300}{50} \quad (2.13)$$

$$B = \frac{\text{w/c ratio}(by weight of cement) - 0.65}{0.075} \quad (2.14)$$

$$C = \frac{\%CaCl_2(by weight of cement) - 2.5}{1.25} \quad (2.15)$$

The final term of the fitted model after omitting the insignificant terms through T-tests for  $I_{corr}$  was given as:

$$i_{corr} = 37.726 + 6.120C + 2.231A^2B + 2.722B^2C^2 \quad (2.16)$$

where  $i_{corr}$  is in  $nA/cm^2$ .

Yamaguchi and Oshida[32] reported a corrosion rate equation by modifying the Stern-Geary equation, taking the effects of cement type, w/b ratio, cover thicknesses, and RH into account, as shown below:

$$i_{corr} = A \cdot S(H) \cdot K_{95}/R_{ct} \quad (2.17)$$

## LITERATURE REVIEW OF CARBONATION-INDUCED CORROSION

where,

$i_{corr}$ : corrosion current density ( $\mu A/cm^2$ ),

$R_{ct}$ : polarization resistance,

$A$ : coefficient of the material, mix proportion, and cover depth,

$S(H)$ : relative humidity correction value,

$H$ : relative humidity,

$K_{95}$ :  $K$  value of 95%RH

$$A = A_1 \cdot A_2 \cdot A_3 \cdot A_4 \quad (2.18)$$

where,

$A_1$ : coefficient of cement type (OPC=0.48, Moderate-heat Portland cement=0.55,

20% replacement ratio of fly ash=1.0),

$A_2$ : coefficient of  $W/B$  ratio ( $= -29 \left(\frac{W}{B}\right)^2 + 33.4(W/B) - 8.58, 0.45 \leq$

$W/B \leq 0.65$ ),

$A_3$ : coefficient of chloride content ( $= 2.50(Cl^-) + 1.0, 0 \leq Cl^- \leq 2.4$ )

$A_4$ : coefficient of cover depth (mm) ( $= 0.025T + 0.5, 20 \leq T \leq 50$ )

Other empirical models considered the electrical resistivity of concrete serves as the significant parameter [33][34]. The corrosion risk is classified according to the electrical resistivity of mortar in[35][36][37][38], as shown in **Error! Reference source not found.** There are different criteria of the corrosion state assessment with the corresponding electrical resistivity of material, which may contribute to the different cement types, concrete properties, exposed local environmental conditions, and even the electrochemical measurement method.

## LITERATURE REVIEW OF CARBONATION-INDUCED CORROSION

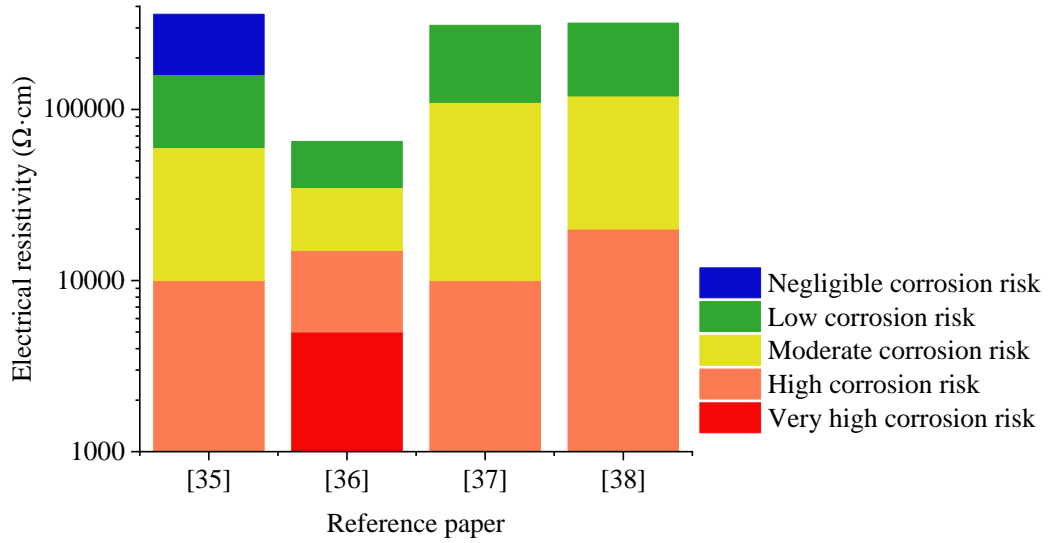


Figure 2.5 Corrosion state assessment according to different electrical resistivity of concrete

Saeki and Otuki[39] proposed an empirical expression for corrosion rate considering the effect of hydration degree, temperature, and water content on electrical resistivity as below:

Saturated concrete electrical resistivity ( $R_H$ ):

$$R_H = -430 - 2710 \log(V/0.431) \quad (2.19)$$

where  $V$  is the pore volume between 75-75000 Å

Ratio to the saturated concrete resistivity ( $R_w$ ):

$$R_w = 49.4 - 1.66w + 0.0195w^2 - 0.0000764w^3 \quad (2.20)$$

where  $w$  is relative water content (%)

Temperature correction coefficient reference to electrical resistivity at 20°C ( $R_T$ ):

$$R_T = 2.5 \times 10^{-0.02T} \quad (2.21)$$

## LITERATURE REVIEW OF CARBONATION-INDUCED CORROSION

where  $T$  is the temperature ( $^{\circ}\text{C}$ )

Mortar electrical resistivity ( $R_m$ ):

$$R_m = R_H \times R_w \times R_T \quad (2.22)$$

Corrosion current density ( $i_{corr}$ ):

$$i_{corr} = 2.2 \times 10^{-0.000064R_m} \quad (2.23)$$

Nevertheless, other authors mentioned that such clarification of resistive control lacks a theoretical basis [40][41][42].

In addition, several papers [42][43] proposed a novel hypothesis from a new perspective that the area of metal in contact with the liquid phase controls the magnitude of the corrosion rate of the steel rebar. Based on such a hypothesis, Stefanoni and Angst[44] developed a quantitative model for the corrosion rate in porous media considering the influencing factors, including porosity, moisture conditions, and pore liquid chemistry, as the following equation:

$$i_{corr,app} = i_{corr,eff_{max}} \times 1/2 \left( 1 + \frac{(P - P_{crit})}{\sqrt{k + (P - P_{crit})^2}} \right) \times P_{sat} \quad (2.24)$$

where,

$P$ : porosity,

$P_{crit}$ : critical porosity (=0.185 for cement-based material),

$P_{sat}$ : water-filled porosity volume fraction,

$k$ : constant (=0.001 for cement-based material),

$i_{corr,eff_{max}}$ : maximum effective corrosion current density.

In the same concrete and steel properties and environmental conditions, the corrosion rate values of steel rebar can be determined following models mentioned above, respectively. The assumed known parameters are shown in Table 2.1, and the calculated

## LITERATURE REVIEW OF CARBONATION-INDUCED CORROSION

results of the relationship between the corrosion rate and relative humidity are shown in Figure 2.6 except the Ahmad model due to the absence of effect of environmental factors. The corrosion rate of steel rebar varies significantly in value deduced from purely empirical models of Morinaga model and Yanaguchi model, even to one to three orders of magnitude difference. Such results indicate that since the mechanism of the corrosion process is not taken into account, the prediction based on empirical models is less reliable. Saeki model and Stefanoni model considered the electrical resistivity related to the microstructure of materials. There is still an order of magnitude difference between the two calculated corrosion rates of steel rebar. Saeki's model considers the effect of temperature and RH on electrical resistivity separately, which is not consistent with the interacted effect of RH and temperature in the real case. Besides, the saturation degree of mortar under each temperature is difficult to obtain in the real field. Stefanoni model needs the detailed microstructure information of concrete, which is difficult to obtain in the real case. Also, the effect of temperature and RH on the electrochemical reaction off steel were not be considered in this model.

Table 2.1 Initial assumed parameters and main coefficient values at each model

Concrete properties	w/c=0.6
	s/c=2
	cover thickness=20 mm
Environmental conditions	RH=74, 84, 91, 97%
	T=20, 30, 50°C

Numerical models vary from complex two- or three- dimensional finite element (FEM) or boundary element models (BEM) [45][46][47][48][49][50], based on the corrosion process simulation. However, such theoretical models are complex, and the necessary input parameters of concrete properties and environmental conditions are difficult to ascertain and need more effort for testing methods.

## LITERATURE REVIEW OF CARBONATION-INDUCED CORROSION

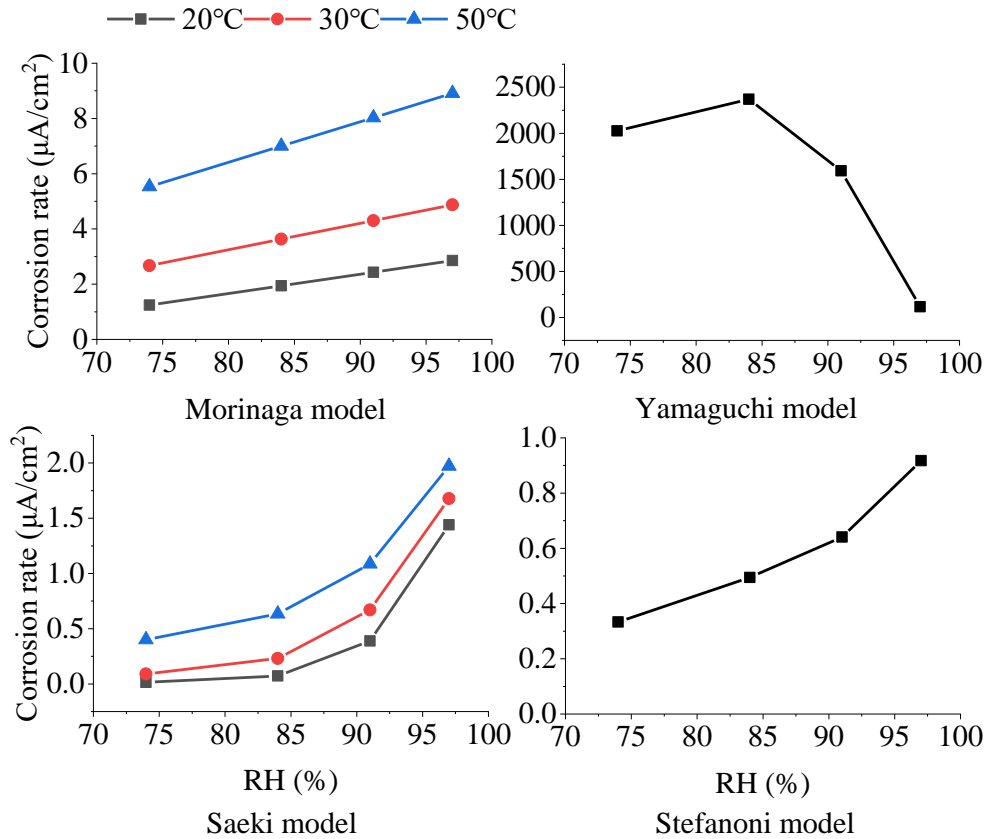


Figure 2.6 Calculated corrosion rate deduced from the empirical models

### 2.4 Summary

The service life prediction and soundness assessment of RC structures affected by carbonation are necessary, especially in the purpose of extending the service life duration of RC structures to the propagation phase of the corrosion process which is lack in the application in the field. The feasible and reliable prediction method of corrosion rate needs to be proposed based on the clarification of corrosion controlling mechanism. Therefore, this study obtained electrochemical parameters in carbonated miniaturized mortar samples exposed to variable environmental conditions to clarify the controlling mechanisms of the corrosion process under specific conditions. A corrosion rate prediction method based on the corrosion controlling mechanisms and a feasible soundness assessment method for existing RC structures are expected to be proposed, contributing to the evaluation of the performance of RC structures.

## LITERATURE REVIEW OF CARBONATION-INDUCED CORROSION

**Chapter 3** considers the effect of environmental conditions on corrosion behavior in carbonated mortar. A prediction method for the corrosion rate of steel rebar was proposed based on the corrosion controlling mechanism under specific conditions. **Chapter 4** focuses on the effect of cover depth on corrosion behavior of steel rebar and corrects the predicted values of corrosion rate considering the cover depth in the real case. **Chapter 5** uses supplementary cementitious material to verify the reliability of the proposed prediction method of corrosion rate of steel rebar presented in **Chapter 3**. Finally, based on the comprehensive analysis in **Chapters 3, and 4** accompanied by Japan Specification Standard, a soundness assessment method for existing RC structures affected by carbonation was offered in **Chapter 6**. As additional information, the corrosion behaviors of steel rebar in the chloride-containing mortar were presented in **Appendix C**.

## EFFECT OF RELATIVE HUMIDITY AND TEMPERATURE ON STEEL CORROSION IN CARBONATED MORTAR

### 3. EFFECT OF RELATIVE HUMIDITY AND TEMPERATURE ON STEEL CORROSION IN CARBONATED MORTAR

#### 3.1 Introduction

Extending the service life of RC structures that exposed to variable environmental conditions to the propagation phase of the corrosion process is challenging because the mechanism controlling the corrosion process is not well understood. In previous studies that discussed the corrosion controlling mechanisms, several authors [30][31] stated that steel corrosion in carbonated concrete is controlled primarily by concrete resistivity and thus is under resistive control based on the relation between the corrosion rate and electrical resistivity. Nevertheless, other authors mentioned that such clarification of resistive control lacks a theoretical basis [32][33][34]. Because the critical role of the liquid phase in the corrosion process of steel rebars was well known [35], a statement that the corrosion process is controlled by the amount and composition of the electrolyte present in the carbonated concrete was proposed [36]. In other cases, the whole cathodic process was evaluated as a function of the water saturation degree [37], taking into account the oxygen reduction and diffusion, and it stated that the cathodic reaction was under diffusion control when water saturation was over 0.9, while under mixed reaction and diffusion control when saturation degree was between 0.8 and 0.9 and under reaction control when saturation degree was under 0.8. In addition, several critical relative humidity (RH) values were proposed based on the change in corrosion rate among the variable environmental conditions: a critical minimum of 50%RH produced a severe corrosion rate when carbonation or chloride existed [38], while others [35] stated that chloride-induced corrosion stopped when pore saturation was below 35% and was under resistive control when pore saturation was below 70%. Hornbostel et al. [26] pointed out that anodic resistance prevented corrosion onset without chloride or carbonation and also considered extreme conditions such as the corrosion processes were controlled by the cathodic reaction when concrete was submerged in water and



## EFFECT OF RELATIVE HUMIDITY AND TEMPERATURE ON STEEL CORROSION IN CARBONATED MORTAR

controlled by concrete resistance in a dry environment. And several papers [34][39] proposed and verified a novel hypothesis from a new perspective that the area of metal in contact with the liquid phase controlled the magnitude of the corrosion rate of the steel rebar.

On the other hand, in Japan, the standards for construction materials or construction methods of reinforced concrete have been established based on research studies and vast experience under mild temperature conditions (around 20°C). These standards are now being used and followed by some RC members without enough local environment investigations. the corrosion progress is based on the diffusion and electrochemical reactions, the deterioration progress should also be considered as having temperature dependence However, there are only a few studies discussed the effect of temperature on the corrosion process[51][52][53], while without the analysis the combined effect of temperature and RH. Therefore, the change of temperature is discussed as a factor of the environmental conditions in this study.

In the current study, carbonated miniaturized reinforcement mortar samples were exposed to various environmental conditions with six different RHs and six different temperature conditions. Electrochemical parameters, including the electrical resistivity of mortar, corrosion potential, and corrosion rate of steel rebar, were measured to clarify the RH and temperature dependence of corrosion behaviors concerning the microstructure and pore solution of mortar and then corrosion control mechanisms under different environmental conditions are proposed.

Based on the proposed corrosion controlling mechanisms under specific environmental conditions, the corrosion rate prediction method is proposed, which is helpful in evaluating the soundness and the service life of RC members under several environmental conditions.

# EFFECT OF RELATIVE HUMIDITY AND TEMPERATURE ON STEEL CORROSION IN CARBONATED MORTAR

## 3.2 Experimental procedure

### 3.2.1 Material

Ordinary Portland cement (OPC) was used throughout the experiment, the chemical and mineral compositions of which are shown in Table 3.1 and Table 3.2, respectively. Two sizes of silica sand (UBE INDUSTRIES 5A and 7) with a density of  $2.6 \text{ g/cm}^3$  were used as fine aggregates for all the mortar mixes. In addition, cracks may occur due to the expansion caused by shrinkage during the drying operation and the carbonation process (refer to Section 3.2.3), which are harmful to the homogenous corrosion process and deteriorate the suitable condition for analyzing corrosion rate. Polypropylene fibers with a length of 6 mm and a diameter of 0.028 mm were added to the mortar material, as shown in Figure 3.1, to prevent cracking. A w/c ratio of 0.60 was chosen to enhance the transport coefficient of carbon dioxide to shorten the carbonation duration and environmental controlling period by the higher porosity of the cement paste matrix. The mortar mix proportions are listed in Table 3.3

Table 3.1 Chemical composition of ordinary Portland cement.

Chemical composition (wt.%)										
Ig.loss(%)	SiO <sub>2</sub>	Al <sub>2</sub> O <sub>3</sub>	Fe <sub>2</sub> O <sub>3</sub>	CaO	MgO	SO <sub>3</sub>	Na <sub>2</sub> O	K <sub>2</sub> O	Cl-	Total
2.72	20.35	5.19	2.97	64.10	1.84	2.09	0.30	0.40	0.012	99.97

Table 3.2 Mineral composition of ordinary Portland cement.

Mineral composition (wt.%)								
C <sub>3</sub> S	C <sub>2</sub> S	C <sub>4</sub> AF	C <sub>3</sub> A	Calcite	Gypsum	Bassanite	Anhydrite	Total
65.2±0.8	11.9±0.4	11.0±0.6	4.6±0.3	3.2±0.1	2.2±0.3	1.09±0.2	0.32±0.1	99.52

Table 3.3 Mix proportion of mortar

Specimen	W/C (%)	S/C	Water (kg/m <sup>3</sup> )	Cement (kg/m <sup>3</sup> )	Sand (kg/m <sup>3</sup> )		Fiber (kg/m <sup>3</sup> )	Sodium chloride (2 wt % of cement)
					1.7-0.2 mm	< 0.2 mm		
Carbonated	60	2	320	534	534	534	0.91	-

## EFFECT OF RELATIVE HUMIDITY AND TEMPERATURE ON STEEL CORROSION IN CARBONATED MORTAR



Figure 3.1 Polypropylene fiber

### 3.2.2 Specimen design

In traditional corrosion experiments of steel rebar in concrete, the samples are typically large in size. As a result, a large amount of time is needed for carbonation to having the required depth reaching the steel rebar surface and for a relative humidity equilibrium to be established. On the other hand, the miniaturized specimens have been used in a few papers. Stefanoni et al. embedded the steel wire into a thin mortar specimen which acted as a working electrode[54]. However, the formation of corrosion products during the corrosion process may break the steel wires due to the small diameter of the steel wire. García-Alonso et al. put different types of steel rebars in a small mortar specimen to evaluate their different corrosion behaviors [55]. But the macrocell corrosion may occur among these steel rebars embedded in the same medium due to the different equivalent potentials. Also, because the part of the extended steel rebar outside the mortar was exposed to a different environment from the embedded part of the steel rebar, it will influence the accuracy of corrosion rate evaluation.

This study uses a novel accelerated test method to overcome these limitations. Miniaturized sample size can reduce the time required for equilibrium between the inside of a mortar sample and environmental RH. For thin mortar covers, carbonation can reach the required depth quickly with little carbonation degradation in the cover layer, thus excessive high CO<sub>2</sub> concentrations are unnecessary. The design of mortar size makes the relative homogeneous state of electrical condition can be achieved, thus improve the accuracy of electrochemical measurement.

## EFFECT OF RELATIVE HUMIDITY AND TEMPERATURE ON STEEL CORROSION IN CARBONATED MORTAR

The SGD 400 rebars classified by JIS G 3132 [56] were embedded in a mortar with a diameter of 10 mm and a length of 30 mm, which is proper for the mortar size. The chemical compositions and mechanical properties of steels used are given in Table 3.4. The insulation layer of the copper wire was scraped off at the front 1 cm. Then copper wires were welded to both sides of the rebar using eutectic solder for electrical connection before a 1 mm thick to avoid corrosion at the connection part. Finally, the steel bars were degreased with acetone immediately before being placed in the mold. The steel rebars were fixed and adjusted to a specific position in the mold by setting welded copper wires at both ends of the mold. The detailed process is shown in Figure 3.2. All the necessary electrochemical tests were successfully and efficiently carried out using this miniaturized sample design and published in [57].



(a) copper wires were welded to both sides of the rebar using eutectic solder



(b) insulation epoxy was glued



(c) the steel rebars were fixed and adjusted to a specific position in the mold

Figure 3.2 Steel rebar treatment process

## EFFECT OF RELATIVE HUMIDITY AND TEMPERATURE ON STEEL CORROSION IN CARBONATED MORTAR

Table 3.4 Chemical composition and mechanical properties of steel material used

Chemical compositions		Tensile strength (N/mm <sup>2</sup> )	Elongation (%)
P	<0.045%	400-510	20-22
S	<0.045%		

The dimensions of the mortar were designed as 20×20×40 mm<sup>3</sup> with enough top surface to place a reference electrode and a counter electrode on it during the electrochemical measurement process. The configuration for the specimens with reinforcing bars is shown in Figure 3.3. The mortar cover depth was 5 mm, and the area exposed to the mortar for each rebar was 9.42 cm<sup>2</sup>.

### 3.2.3 Accelerated carbonation and environmental condition control

All the samples were set and hardened in the mold for one day at 20±2 °C before being

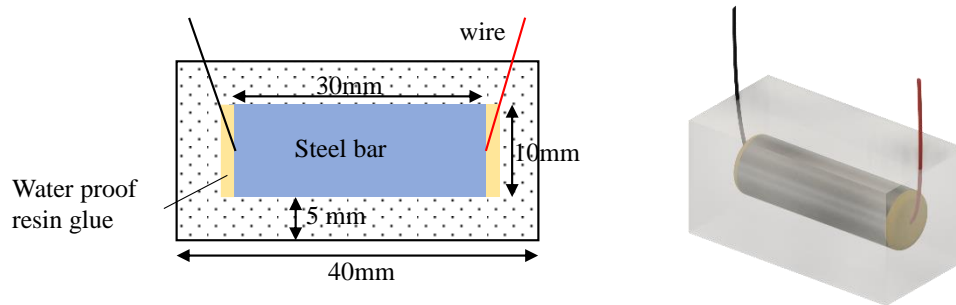


Figure 3.3 The schematic diagram of the mortar specimen

demolded, then were sealed in a curing room at 20±2 °C for 28 days. After curing, mortar specimens were dried in an oven at 105 °C until they reached a constant weight so that carbon dioxide could penetrate more easily without evaporable water inside the mortar during the accelerated carbonation process. The dried specimens were then moved to an accelerated carbonation chamber (Standard accelerated carbonation test equipment (MARUI) MIT-639-305) with a 5% CO<sub>2</sub> concentration and 60% RH, which could represent carbonation in a natural environment. Dummy samples were cast, cured, and carbonated under the same conditions without steel rebar. They were used to verify the carbonation depth by a phenolphthalein test and carbonation degrees by X-ray diffraction (XRD)/Rietveld analysis in Appendix A.

## EFFECT OF RELATIVE HUMIDITY AND TEMPERATURE ON STEEL CORROSION IN CARBONATED MORTAR

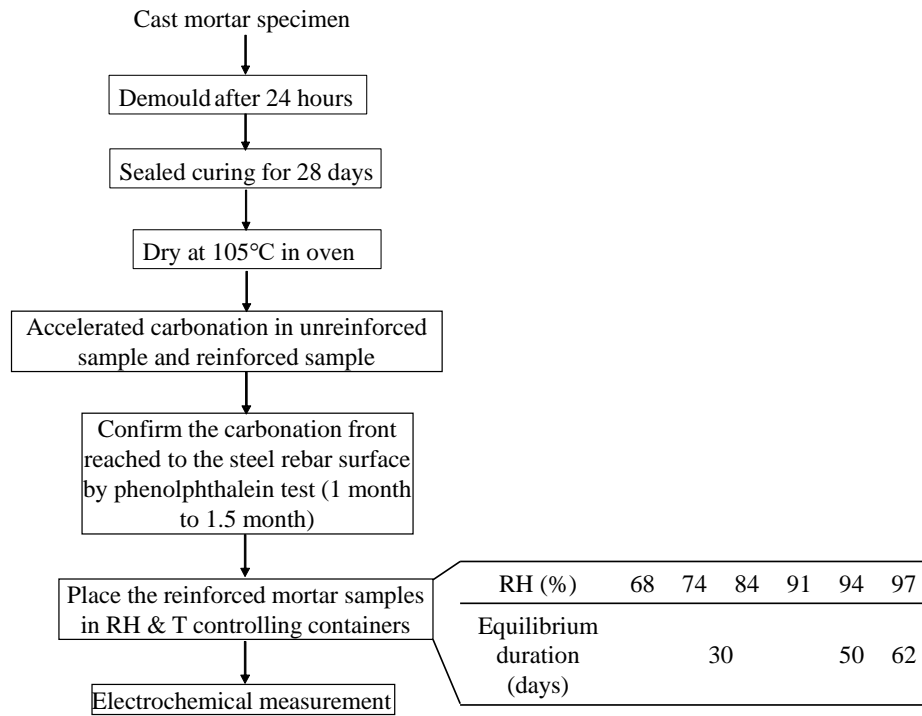


Figure 3.4. Experiment process

After confirming that all sectional areas of the dummy mortar specimens were carbonated, the reinforced specimens were placed under different experimental conditions. For environmental condition control, for RH controlling, the samples were placed in sealed boxes with certain saturated salt solutions, as shown in Table 3.5, to reach the desired RH conditions higher than 60%, which are 68%, 75%, 84%, 91%, 94%, and 97% at  $20 \pm 1$  °C [58]. Subsequently, the sealed containers were placed in a temperature-controlled chamber of 30 °C, 35 °C, 40 °C, 45 °C, and 50 °C. The mass of the samples under each environmental condition was monitored at regular intervals throughout the exposure period to check whether the equilibrium of the conditions inside and outside the mortar samples reached or not. Samples reached a stable state when the difference in weight between two consecutive measurements was within 0.03%. The stable state was obtained after the 30 days for the mortar samples exposed to 68% to 91% RH and after 50 days and 62 days for those exposed to 94% RH and 97%RH, respectively. Then electrochemical measurements were performed after the

## EFFECT OF RELATIVE HUMIDITY AND TEMPERATURE ON STEEL CORROSION IN CARBONATED MORTAR

stable state was achieved. It should be noted that no water condensation occurs in the containers by keeping the temperature constant at each environmental condition. The experimental process is illustrated in Figure 3.4.

Table 3.5 Relative humidity in the presence of saturated solution at 20 °C.

Salt solution	K <sub>2</sub> SO <sub>4</sub>	KNO <sub>3</sub>	BaCl <sub>2</sub>	KCl	NaCl	KI
RH (%)	97	94	91	84	74	68

The water content under each environmental condition was determined by cutting sample fragments from the unreinforced mortar specimens. The mass of the mortar fragments,  $m_s$ , under each environmental condition was measured using a balance with a resolution of 1 mg. Subsequently, the mortar fragments were oven-dried at 105 °C for twenty-four hours. The weights of the specimens after oven-drying ( $m_d$ ) were measured and recorded. The percentage of water content,  $w$ , in the mortar fragments under different environmental conditions after the samples reached relative humidity equilibrium can be expressed as:

$$w = \frac{m_s - m_d}{m_d} \times 100\% \quad (3.1)$$

### 3.2.4 Electrochemical measurements

Corrosion current density ( $i_{corr}$ ) measurements of rebar embedded in mortar samples were performed using an electrochemical potentiostat (HOKUTO HZ-7000) with a three-electrode system, as shown in Figure 3.5, where Ag/AgCl as the reference electrode, the stainless plate (SUS 304-JIS G 3601) acted as a counter electrode, and the steel rebar acted as a working electrode. Intimate contact between the specimen and the reference electrode was achieved using a sponge saturated with conductive gel (a solution of distilled water, sodium carboxymethyl cellulose, and sodium chloride in a weight ratio of 94:3:3 [59]).

## EFFECT OF RELATIVE HUMIDITY AND TEMPERATURE ON STEEL CORROSION IN CARBONATED MORTAR

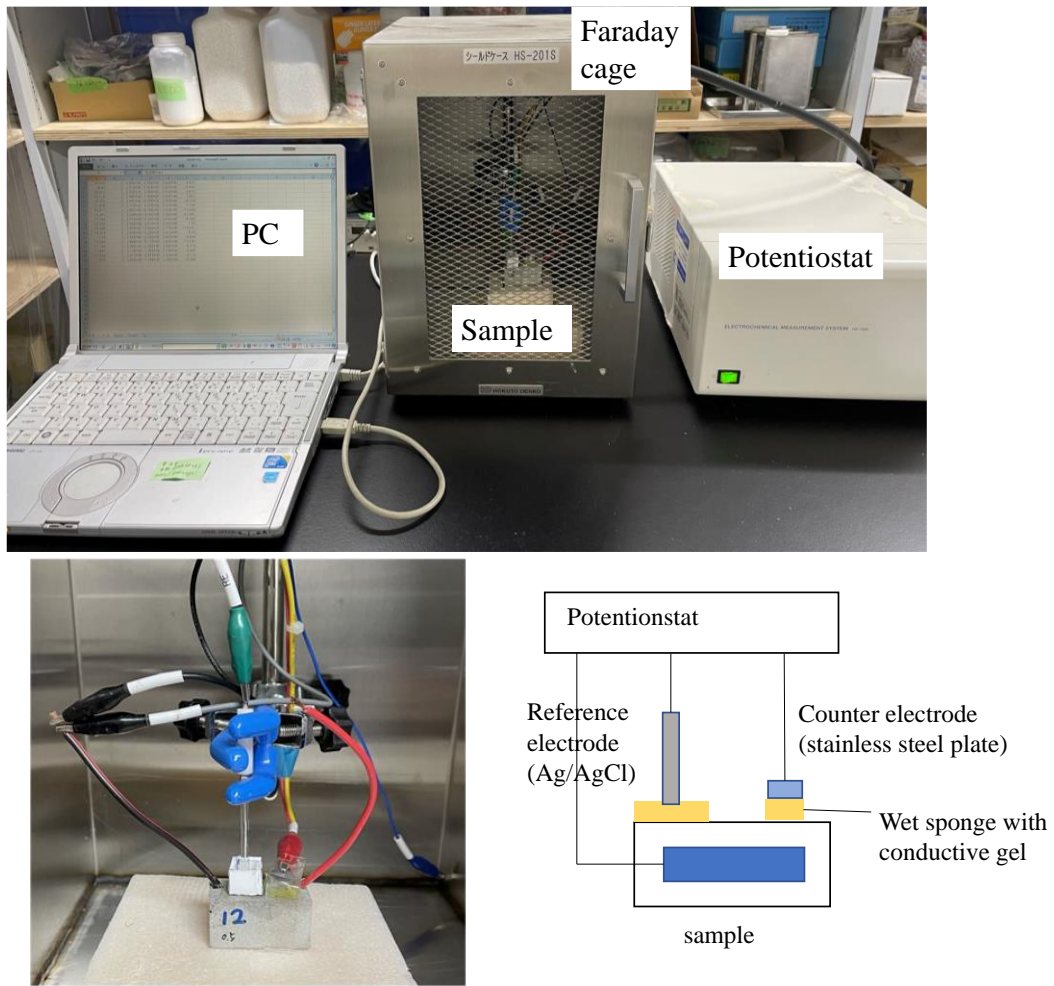


Figure 3.5 Experimental setup of three-electrode cell setup for corrosion rate measurements

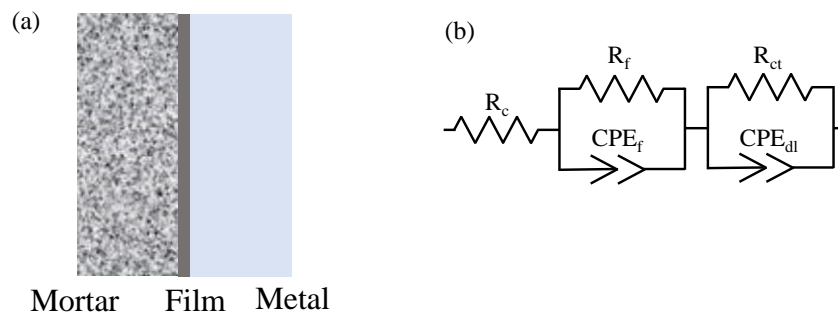


Figure 3.6 Physical models (a) and corresponding electrical circuit (b) for rebar in mortar



## EFFECT OF RELATIVE HUMIDITY AND TEMPERATURE ON STEEL CORROSION IN CARBONATED MORTAR

Electrochemical impedance spectroscopy (EIS) was performed using a 10-mV amplitude sine wave signal in the 0.1 Hz - 100 kHz frequency range with 20 points per decade based on the corrosion potential ( $E_{corr}$ ) measured by the electrochemical potentiostat before every scanning. The Nyquist curve was analyzed using an electrical circuit model [60], as shown in Figure 3.6.  $R_c$  refers to the solution resistance, in this case, the electrical resistance of the mortar.  $R_f$  denotes the resistance of the passive film, respectively.  $CPE_{dl}$  represents the constant phase element of the double electrical layer provided by the charged ions on the surface of the rebar.  $R_{ct}$  is the charge transfer resistance, representing the ease with which charged iron ions leave the metal surface and enter the solution.

Distributed CPEs are widely used in data fitting to allow for depressed semicircles caused by irregularities and roughness on the steel rebar surface, associated with an irregular distribution of the applied potential of 10 mV. The impedance of CPE ( $Z_{CPE}$ ) can be calculated by[61][62]:

$$Z_{CPE} = Z_P(jw)^n \quad (3.2)$$

where,

$Y_0$ : a real adjustable constant used in the non-linear least-squares fitting

$j$ : the imaginary unit

$w$ : the angular frequency

$n$ : the deviated capacitance degree of the electrode from a pure capacitor. CPE is an inductor when  $n=1$ , a resistor when  $n=0$ , and a Warburg admittance when  $n=0.5$ .

The obtained charge transfer resistance ( $R_{ct}$ ) can be used to calculate the corrosion current according to the Stern-Geary equation [63]:

$$I_{corr} = \frac{B}{R_{ct}} \quad (3.3)$$

## EFFECT OF RELATIVE HUMIDITY AND TEMPERATURE ON STEEL CORROSION IN CARBONATED MORTAR

where  $B$  is a constant, which can be assumed to be 26 mV for actively corroding steel or 52 mV when no significant corrosion occurs [64]. Assuming homogeneous corrosion, the corrosion current density  $i_{corr}$  which represents the corrosion rate can be calculated as:

$$i_{corr} = \frac{I_{corr}}{A} \quad (3.4)$$

where  $A$  is the exposed area of the steel rebar.

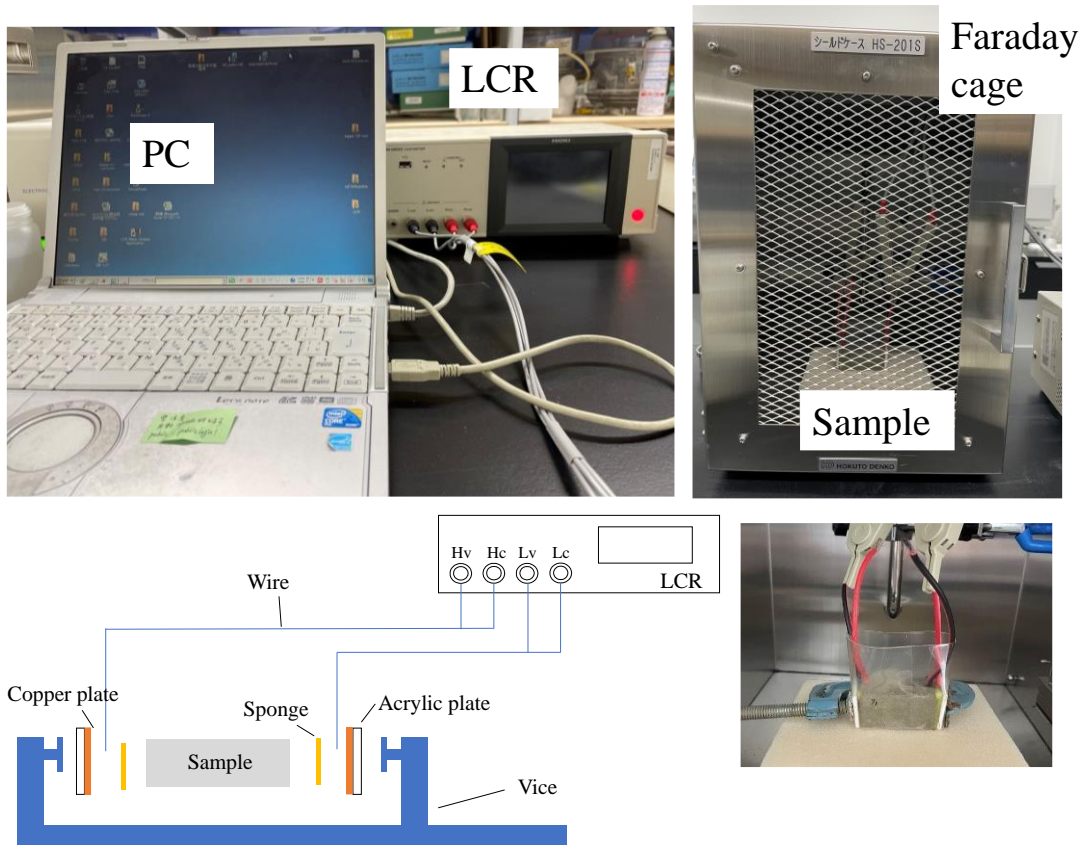


Figure 3.7 LCR arrangement for two-point electrical measurement

## EFFECT OF RELATIVE HUMIDITY AND TEMPERATURE ON STEEL CORROSION IN CARBONATED MORTAR

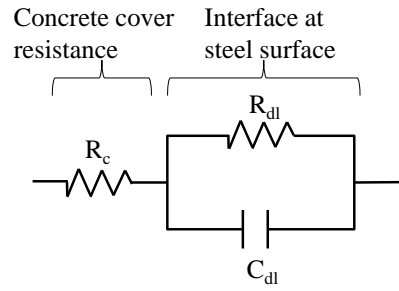


Figure 3.8 Randles electronic circuit for rebar in mortar

The electrical resistivity of the mortar was monitored using an LCR meter (IM3533-HIOKI) over a frequency range of 0.1 Hz to 100 kHz by applying an AC perturbation with an amplitude voltage of 50 mV. A schematic of this process is shown in Figure 3.7. In this arrangement, copper and acrylic plates were placed against the two opposite faces of the mortar specimen as two parallel electrodes. The faces were thoroughly cleaned with emery paper to remove deposits. All impedance spectra were fitted to a Randles equivalent circuit [65], considering the interface of the steel rebar (refer to Figure 3.8) using the EIS Spectrum Analyzer software. The resistance of the steel rebar can be ignored because it is too small compared to that of mortar. As the parallel plate ensures volume electrical conduction, the resistivity of the mortar specimen,  $R_\Omega$ , can then be evaluated as [66]:

$$R_\Omega = \frac{R_c \cdot A_s}{L} \quad (3.5)$$

where,

$R_c$ : the mortar resistance measured by the LCR,

$A_s$ : the cross-sectional area of the specimen,

$L$ : the distance between the electrodes.

## EFFECT OF RELATIVE HUMIDITY AND TEMPERATURE ON STEEL CORROSION IN CARBONATED MORTAR

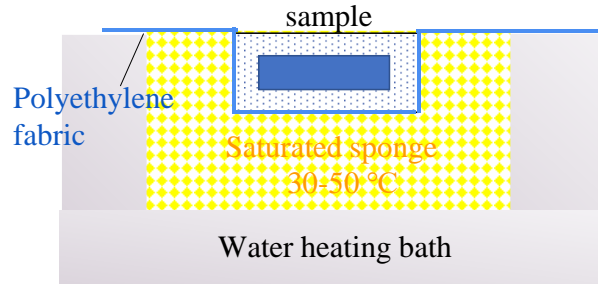


Figure 3.9 Setup of sample in the water bath

For the electrochemical experiment under the higher temperatures than room temperature, the samples are emerged into a water bath (AS ONE TB-1N) with the setting of the requested temperatures to keep the temperature during the measurement duration. The heat transfer medium is the saturated sponge between the mortar sample and the water bath. The setup is shown in Figure 3.9.

### 3.2.5 Microstructure of mortar

Mercury intrusion porosimetry tests were conducted to determine the porosity and pore-size distribution of carbonated mortar specimens. All samples were initially oven-dried at 80 °C for 24h. Mercury intrusion porosimetry was conducted using an Autopore III 9410 W (Shimadzu) with a peak pressure of 206 MPa. The contact angle and surface tension values used during the measurements were 130° and 0.485 N/m, respectively. The relationship between pressure and pore diameter was calculated as follows [67]:

$$d = \frac{-4\gamma(\cos\theta)}{p} \quad (3.6)$$

where,

$d$ : the pore diameter,

$p$ : the applied pressure,

$\gamma$ : the surface tension of mercury,

$\theta$ : the contact angle between the specimen and the mercury.

## EFFECT OF RELATIVE HUMIDITY AND TEMPERATURE ON STEEL CORROSION IN CARBONATED MORTAR

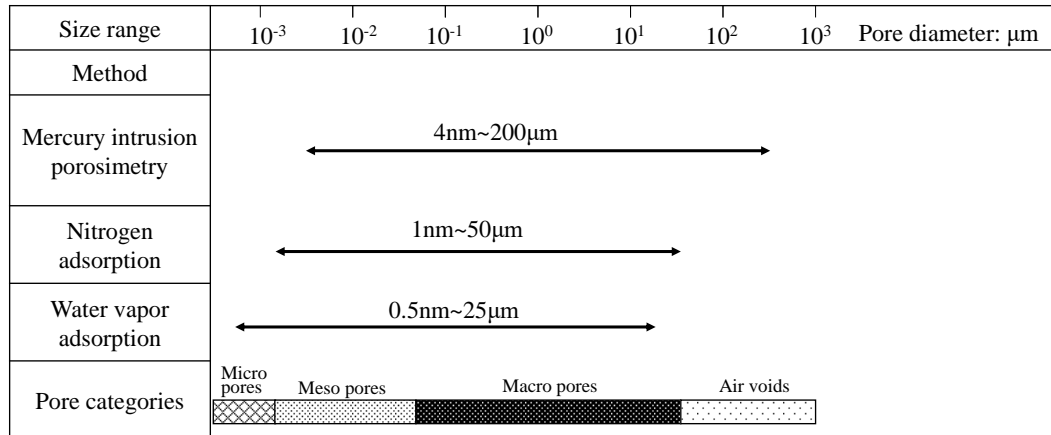


Figure 3.10 Range of pore sizes seen in different measurement techniques

The range of measurable pore size of each method is limited to only a part of the full pore structure of mortar. Figure 3.10 summarizes the approximate range of pore size of several different methods[68]. Since the range of measurable pore sizes of MIP is limited to 4 nm and larger, water vapor sorption and nitrogen sorption were performed as complementary measurements to provide information on micropores that are less well reflected by MIP.

As a pretreatment, the ground powders (sizes of the particle are between 25 and 75  $\mu\text{m}$ ) of the mortar samples were dried under a vacuum condition at 20 °C. Water vapor sorption measurements were then conducted using the volumetric method with a water vapor sorption analyzer (VSTAR, Quantachrome instrument). A sample of 200 $\pm$ 2 mg was used for each measurement at 20 °C.

### 3.3 Experimental results

#### 3.3.1 Electrical resistivity of carbonated mortar

This section presents the results of the obtained electrochemical parameters, including the electrical resistivity of the mortar, corrosion rate, corrosion potential of the steel

## EFFECT OF RELATIVE HUMIDITY AND TEMPERATURE ON STEEL CORROSION IN CARBONATED MORTAR

rebar under different environmental conditions, and the related microstructure characterization of the carbonated mortar.

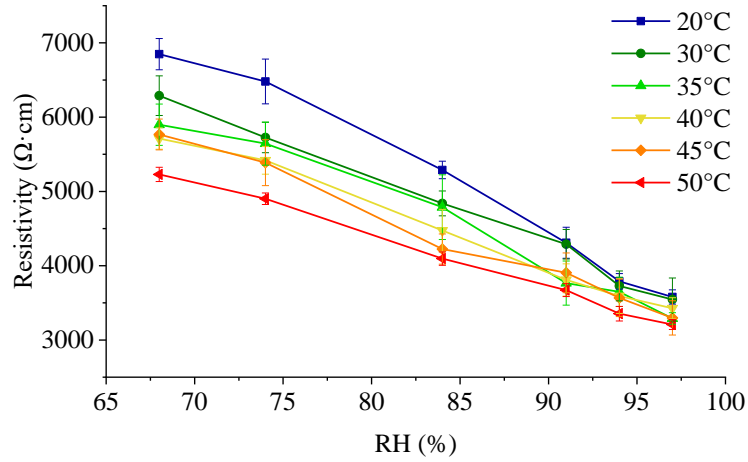


Figure 3.11 Electrical resistivity of carbonated mortar at different RH and temperature conditions

Figure 3.11 shows the electrical resistivity of the carbonated mortar under different RH and temperature conditions, in which the data correspond to the average value of two or three replicates. As expected, increases in the relative humidity and temperature were accompanied by decreases in the electrical resistivity of the mortar specimens. The minimum values of electrical resistivity of 3209  $\Omega\cdot\text{cm}$  occurred at the highest RH and temperature conditions (RH=97%, T=50°C), whereas the maximum values of electrical resistivity of 6468  $\Omega\cdot\text{cm}$  were observed at the lowest RH and temperature conditions (RH=68%, T=20 °C).

### 3.3.2 The corrosion rate of steel rebar in carbonated mortar

Figure 3.12 shows the evolution of the corrosion rate of steel rebar in the carbonated mortar at temperatures ranging from 20°C to 50°C under different RH conditions, in which each point refers to the average value obtained from four replicates. As expected, the corrosion rates of the steel rebar increased with increasing RH values. A sudden increase in the carbonation-induced corrosion rate from an RH turning point of 94% was observed, especially at higher temperatures of 40°C, 45°C, and 50°C. The mortar

## EFFECT OF RELATIVE HUMIDITY AND TEMPERATURE ON STEEL CORROSION IN CARBONATED MORTAR

saturation degree at the turning point was 47.8% to 68.2% under all temperature conditions (show in Appendix B).

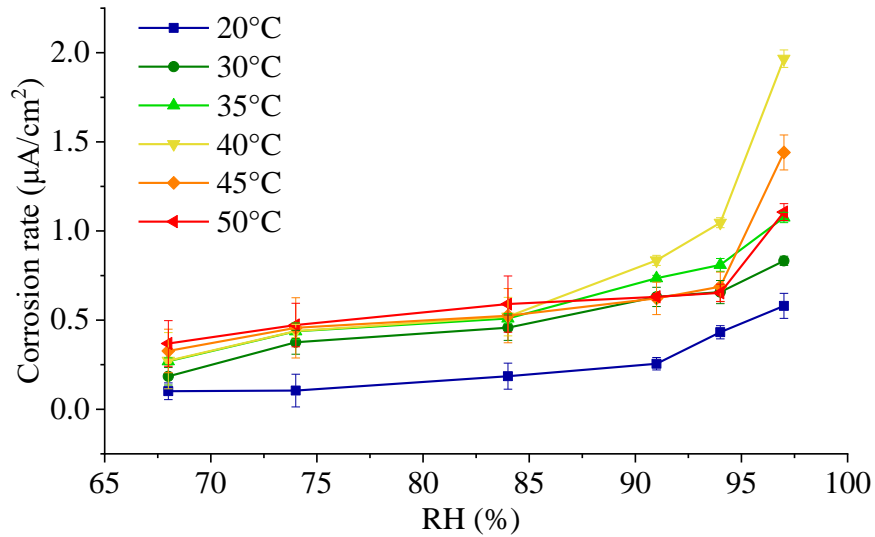


Figure 3.12 Relationship of corrosion rate of steel rebar and RH in the carbonated mortar under variable temperature conditions

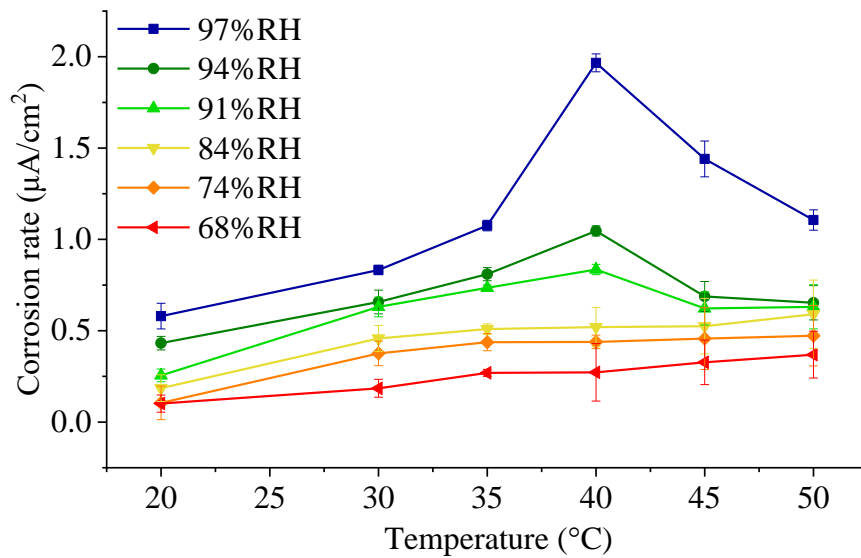


Figure 3.13 Relationship of corrosion rate of steel rebar and RH in the carbonated mortar under variable temperature conditions

Figure 3.13 shows the evolution of the corrosion rate of the steel rebar in the carbonated mortar under variable temperature conditions. When the temperature was over 40°C,

## EFFECT OF RELATIVE HUMIDITY AND TEMPERATURE ON STEEL CORROSION IN CARBONATED MORTAR

the corrosion rate of steel rebar under higher RH conditions (91%, 94%, 97%) showed a continuous attenuation, which indicates the peak value of temperature was 40°C, where the highest corrosion rate had occurred. The corrosion rate increased approximately 4-10 times before reaching the peak value. However, such a temperature peak was not apparent when RH was lower than 84%.

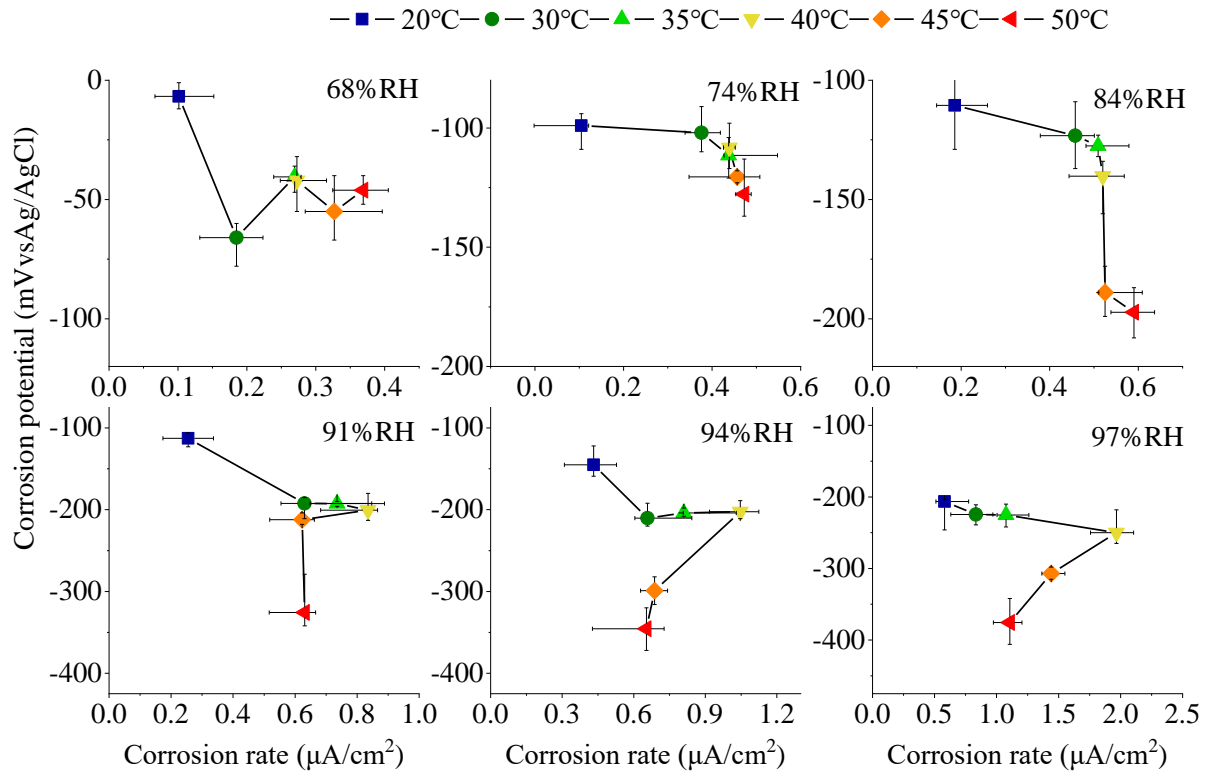


Figure 3.14 The correlation between the corrosion rate and corrosion potential of steel rebar in the carbonated mortar under different temperatures for each RH condition (error bars represent the measured range)

### 3.3.3 Corrosion potential of steel rebar in carbonated mortar

The correlations between the corrosion rate and corrosion potential of steel rebar in the carbonated mortar under different environmental conditions are shown in Figure 3.14. An increase in the corrosion rate can be generally found with corrosion potential shifting more negatively in spite of exposed environmental conditions. On the other hand, the exceptions occurred under 91%, 94%, and 97%RH with 45°C and 50°C, where the corrosion rate decreased while the corrosion potential getting more negative.



## EFFECT OF RELATIVE HUMIDITY AND TEMPERATURE ON STEEL CORROSION IN CARBONATED MORTAR

It should be mentioned that the greater variation observed in the corrosion potential at 68%RH conditions might be due to the more inhomogeneity of mortar under dry conditions.

### 3.3.4 Microstructure characterization of mortar

Figure 3.15 illustrates the pore size distributions and accumulated pore volumes of the non-carbonated and carbonated mortars. The porosity of the carbonated mortar was 16.1%, which is lower than that of the non-carbonated mortar (22.5%). The volume of the pores ranging from 4 to 50 nm corresponded to capillary mesopores [69] in carbonated mortar is smaller than that in non-carbonated mortar owing to the clogging effect of the pores occupied by the calcium carbonation formed from calcium hydroxide (CH) and calcite-silicate-hydrate (C-S-H) [70][71]. In addition, carbonation products are also capable of producing larger capillary 50-100 nm pores, which appear between calcium carbonate crystals and the porous structure of silica gel [72][73], increasing the pore volume of the carbonated mortar. Because the range of measurable pore sizes of MIP is limited to 4 nm and larger, water vapor sorption was performed as

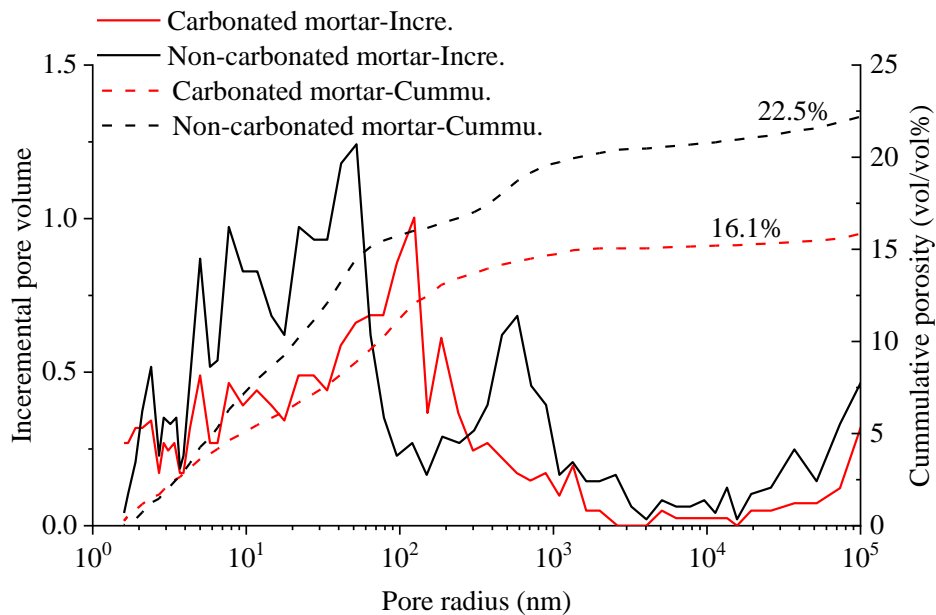


Figure 3.15 Pore size distribution and cumulative porosity of carbonated mortar and non-carbonated mortar

## EFFECT OF RELATIVE HUMIDITY AND TEMPERATURE ON STEEL CORROSION IN CARBONATED MORTAR

complementary measurements to provide information on micropores ranging from 1 to 10 nm that are less well reflected by MIP

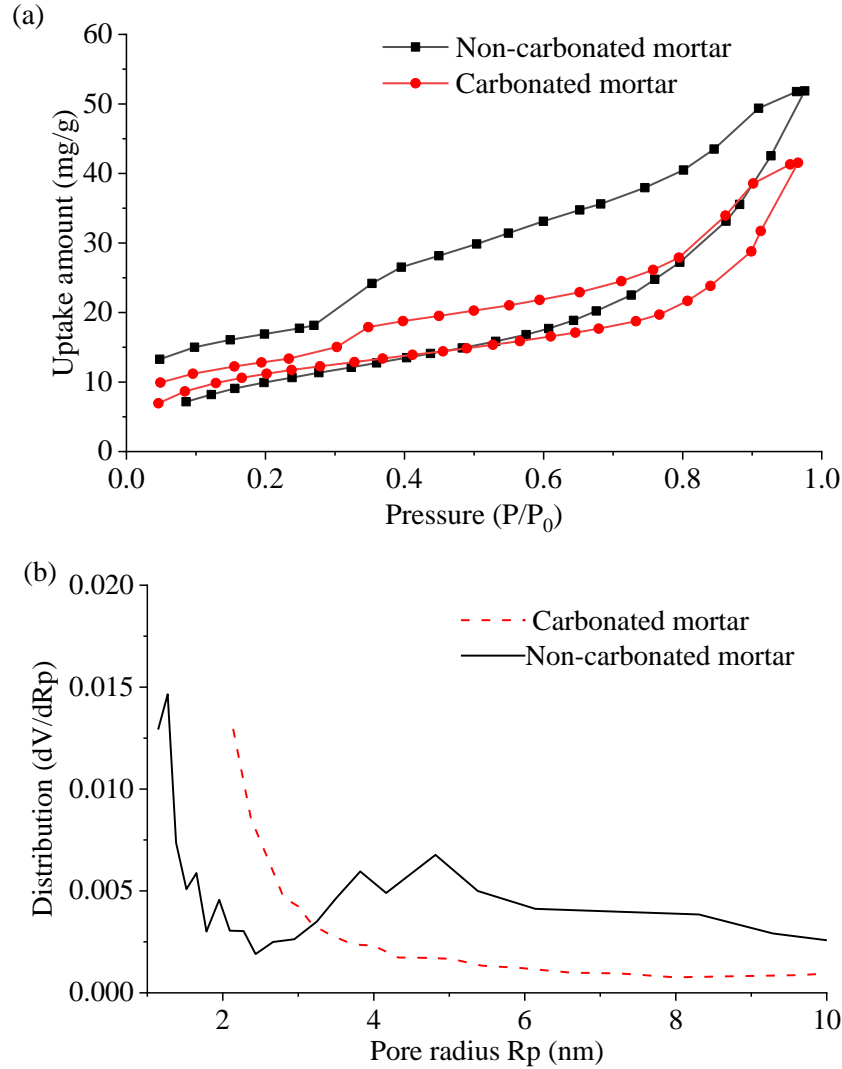


Figure 3.16 Water vapor sorption isotherms (a) and pore size distribution (b) determined from the water adsorption branch

The water vapor sorption isotherms of the non-carbonated and carbonated mortar were shown in Figure 3.16 (a). The pore size distributions shown in Figure 3.16 (b) were determined by sorption isotherms based on the BJH method [74], assuming cylindrical pores with a thickness of adsorption by the BET model [75] for water sorption isotherm.

## EFFECT OF RELATIVE HUMIDITY AND TEMPERATURE ON STEEL CORROSION IN CARBONATED MORTAR

It is evident that the micropore volume with pore sizes ranging from 1 to 10 nm in the non-carbonated mortar was higher than that in the carbonated mortar because of the calcium carbonation clogging effect.

Figure 3.17 shows water content changes in the carbonated mortar in different RH conditions. As expected, the water content increased with RH due to more liquid water condensed in the pores, while it decreased with temperature because of the increasing water vapor pressure. The water content increased when RH increased, which is in agreement with the increased capillary pore volume in Figure 3.15.

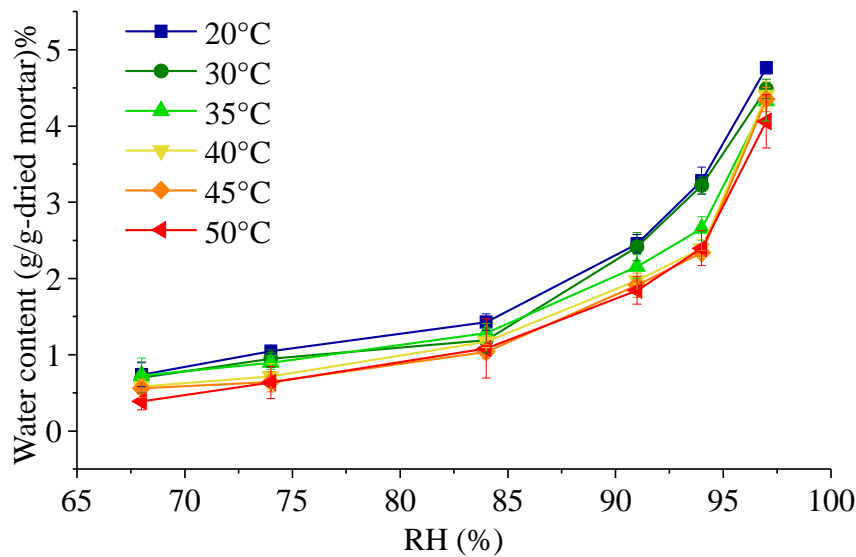


Figure 3.17 Water content of carbonated mortar at different RH and temperature conditions

### 3.4 Discussion

#### 3.4.1 Effect of RH and temperature on the electrical resistivity of carbonated mortar

It was suggested that the conduction through mortar depends on two parts: one is the electrolyte, in which the principal ions are  $\text{Ca}^{2+}$ ,  $\text{Na}^+$ ,  $\text{K}^+$ ,  $\text{OH}^-$ , and  $\text{SO}_4^{2-}$  [76], and the other is an electric solid phase, such as the hydroxide ions in the mesopores in C-S-H

## EFFECT OF RELATIVE HUMIDITY AND TEMPERATURE ON STEEL CORROSION IN CARBONATED MORTAR

[77] and conductive AFm phase via the weakly-bonded anions exchange ( $\text{OH}^-$ ,  $\text{SO}_4^{2-}$ , and  $\text{CO}_3^{2-}$ )[78]. Relative humidity influences electrolyte condensation. For a certain temperature, the condensation maximum radius corresponding to the relative humidity can be determined by Kelvin's equation [79]:

$$\ln \frac{P}{P_0} = -\frac{2V\gamma}{rRT} \quad (3.7)$$

where,

$\frac{P}{P_0}$ : the partial pressure of water vapor,

$V$ : the molar volume of water,

$\gamma$ : the water surface tension

$r$ : the pore radius,

$R$ : the universal gas constant,

$T$ : the absolute working temperature.

According to this equation, each RH has a matching critical pore radius, below which pores remain water-saturated and above which water will evaporate. The evaporation establishes preferential aeration channels for the penetration of oxygen through vapor-phase diffusion with a coefficient  $10^4$  times greater than in a liquid phase [80]. Therefore, under the same temperature conditions, as the maximum radius increases with increasing RH, the amount of electrolyte in the pore system increases with increasing RH for a certain mortar microstructure (Figure 3.17).

As shown in Figure 3.18, water content within the pore system plays an essential role for the passage of electrical current when the electrical resistivity of mortar is measured by two electrodes, through which electrical resistivity can be determined. The lack of

## EFFECT OF RELATIVE HUMIDITY AND TEMPERATURE ON STEEL CORROSION IN CARBONATED MORTAR

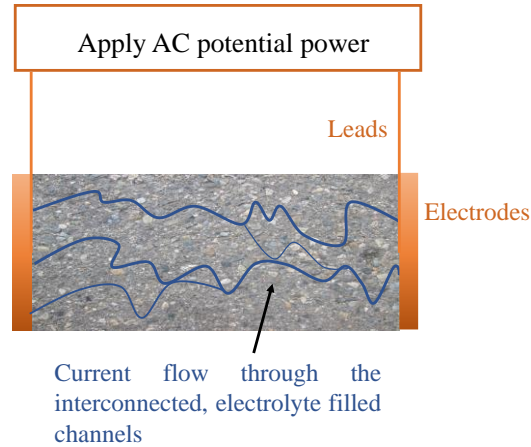


Figure 3.18 The role water content plays in electrical resistivity of mortar

water content will restrict the current flow and increase the electrical resistivity of mortar.

The relationship between the electrical resistivity and water content in the carbonated mortar under each temperature condition is shown in Figure 3.19. As expected, the electrical resistivity of the carbonated mortar decreased as the water content increased. A similar changing trend of the electrical resistivity of mortar concerning RH or water content was also reported in [41][81].

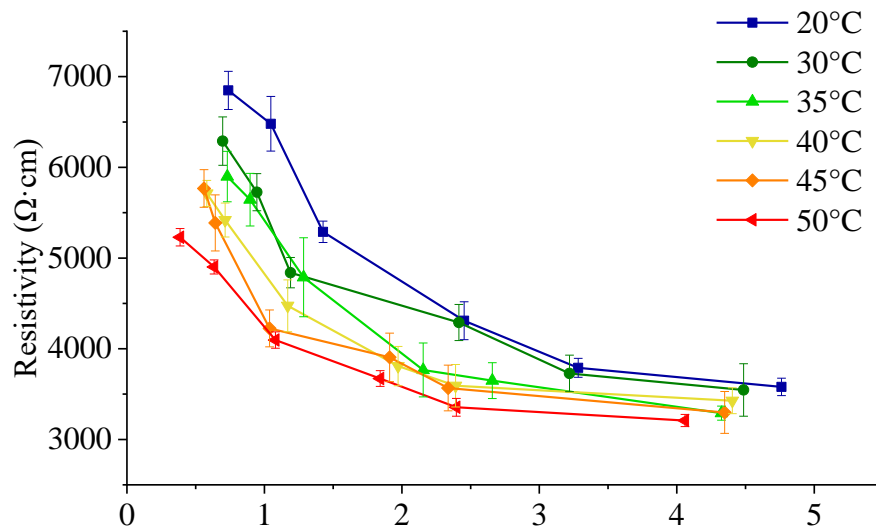


Figure 3.19 Relationship of electrical resistivity and water content in the carbonated mortar under variable temperature conditions

## EFFECT OF RELATIVE HUMIDITY AND TEMPERATURE ON STEEL CORROSION IN CARBONATED MORTAR

Concerning the effect of temperature on the electrical resistivity of mortar, the elevated temperature increases the mobility of free ions through the pore electrolyte and the conductivity of the silica, alumina, and interlayer calcium ions weakly bound by C-S-H [77], weakly-bonded anions on AFm phases (hydroxide, sulphide and carbonate)[78], and alkali metal hydroxides (sodium and potassium hydroxide), resulting in a reduction in the electrical resistivity of carbonated mortar (Figure 3.19). The decreasing trend of the electrical resistivity of the cement material with increasing temperature was also verified in other studies [82][83]; however, the effect of water content on temperature dependence was not considered. The temperature dependence of the electrical resistivity can be determined from the value of the apparent activation energy  $E_{app}$  in the Arrhenius equation [52]:

$$R = a e^{-\frac{E_{app}}{R_g T}} \quad (3.8)$$

where  $R$  is the electrical resistivity,  $a$  is a constant frequency factor,  $R_g$  is the ideal gas constant (8.314 J/K), and  $T$  is the absolute temperature (K). The larger the  $E_{app}$  is, the larger the electrical resistivity change per degree of temperature. Figure 3.20 presents the logarithm of the electrical resistivity of mortars against the reciprocal of the absolute temperature ( $1/T$ ) at each water content in carbonated, in which the electrical resistivity of mortar at each water content was determined by polynomial curve fitting of the data points in Figure 3.19. The linear relationship between the logarithms of the electrical resistivity of the mortars and the reciprocal of the absolute temperature can be explained by the Arrhenius plot, which was derived by taking the log of both sides of Eq. (3.8):

$$\log R = A \left( \frac{1}{T} \right) + B \text{ with } A = -\frac{E_{app}}{R_g} \cdot \log_{10} e \text{ and } B = \log a \quad (3.9)$$

Thus, the apparent activation energy  $E_{app}$  can be determined from the slope of the regression line.

# EFFECT OF RELATIVE HUMIDITY AND TEMPERATURE ON STEEL CORROSION IN CARBONATED MORTAR

$$E_{app} = -\frac{R_g}{\log_{10}e} \cdot A = -19.14 \cdot A \quad (3.10)$$

The apparent activation energy  $E_{app}$  of the electrical resistivity of the carbonated mortar with each amount of water content determined by Eq. (3.10) is also presented at the end of each line in Figure 3.20. In the carbonated mortar, a decreasing tendency of  $E_{app}$  with an increase in water content was observed. One possible reason is that the denser microstructure is modified by the carbonation process [84]: the gel pores and interlayer space inside the C-S-H clusters collapsed, while new capillary pores appeared owing to the porous structure of the formed silica gel and mesopores between calcium carbonate crystals [85] (Figure 3.15), and the denser pore system enhanced the effect of water content change on interconnectivity. In this case, the higher degree of interconnectivity of the electrolyte increases through the pore systems as the water content increases. Eventually, the temperature dependence of the electrical resistivity decreased because the effect of water content was more predominant than the effect of temperature. This changing trend of  $E_{app}$  in this study is similar to the results of previous studies [51]

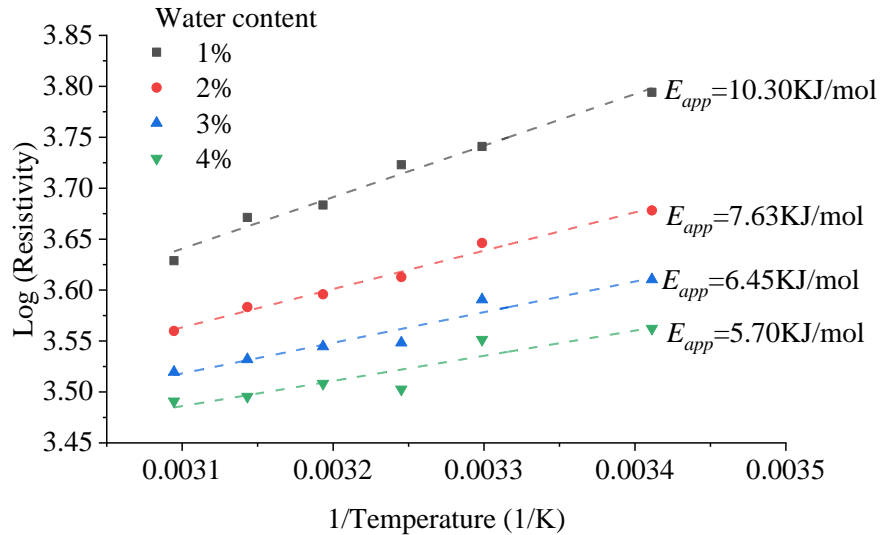


Figure 3.20 Arrhenius plots of electrical resistivity of carbonated mortar

## EFFECT OF RELATIVE HUMIDITY AND TEMPERATURE ON STEEL CORROSION IN CARBONATED MORTAR

### 3.4.2 Effect of RH and temperature on corrosion rate of steel rebar

Since only liquid water participates in the corrosion reaction, which is influenced by RH and temperature simultaneously, the water content is considered in the discussion of the corrosion rate in the carbonated mortar. Figure 3.21 shows the relationship between the corrosion rate of the steel rebar and the water content in the carbonated mortar. As the ion flow is promoted by the increased water content in the pore system, the corrosion rate increases in the carbonated mortar as expected.

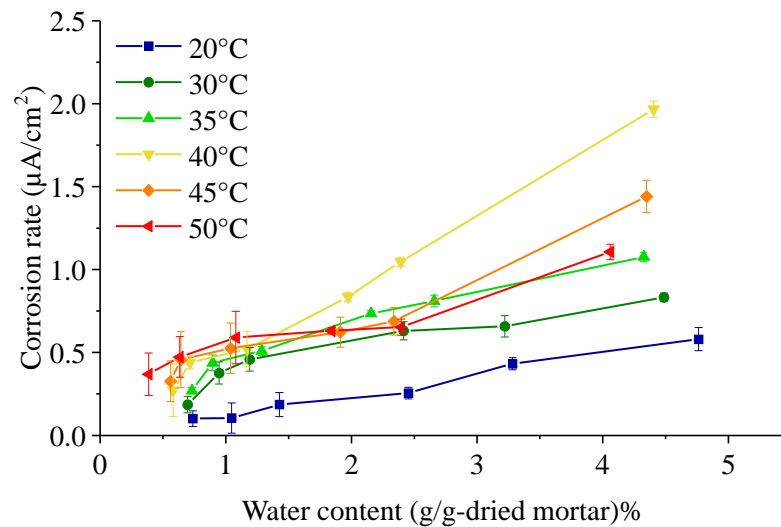
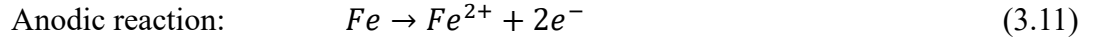


Figure 3.21 Relationship of corrosion rate of steel rebar and water content in the carbonated under variable temperature conditions

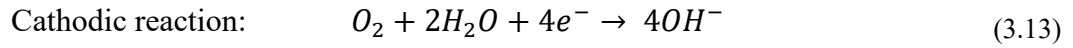
The turning point of 94%RH in carbonated mortar is shown in Figure 3.12 due to the interconnectivity of electrolytes and anodic reaction in the corrosion process. The concentrations of  $Fe^{2+}$  and  $O_2$  on the steel rebar surface affect the reversible potential of the anodic and cathodic reactions in which they are involved, respectively, which can be described by the Nernst equations [86]:



# EFFECT OF RELATIVE HUMIDITY AND TEMPERATURE ON STEEL CORROSION IN CARBONATED MORTAR



$$E_{Fe/Fe^{2+}} = E_a^0 + \frac{RT}{2F} \ln[Fe^{2+}] \quad (3.12)$$



$$E_{O_2/OH^{-}} = E_c^0 + \frac{RT}{4F} \ln \frac{[O_2]}{[OH^{-}]} \quad (3.14)$$

where,

$E_{Fe/Fe^{2+}}$  and  $E_{O_2/OH^{-}}$ : the anodic and cathodic reversible potentials, respectively,

$E_a^0$  and  $E_c^0$ : the standard equilibrium potentials of the anodic and cathodic reactions,

$F$ : the Faraday constant,

$R$ : the gas constant,

$T$ : the absolute temperature,

$[Fe^{2+}]$ ,  $[O_2]$  and  $[OH^{-}]$ : the corresponding concentrations.

According to Nernst equation Eq.(3.12), when the interconnectivity of electrolytes in the pore system is established under high RH conditions, the formed interconnectivity of the electrolyte drastically increases the possible diffusion of iron ions released by the anodic reaction, leaving the steel rebar surface to the bulk. The reduction of the iron ion concentration at the steel rebar surface decreases the anodic reversible potential, resulting in a significant increase in the corrosion rate.

The corrosion reaction of steel represents an electrochemical reaction; thus, the ion diffusion rate is dependent on the ambient temperature, that is, the elevated temperature accelerates the corrosion rate of the steel rebar. In addition, an increase in temperature accelerates the permeability of oxygen, which is essential for the cathodic reaction, and

## EFFECT OF RELATIVE HUMIDITY AND TEMPERATURE ON STEEL CORROSION IN CARBONATED MORTAR

increases the corrosion rate (Figure 3.12). This result was also confirmed by the experimental results of the carbonated mortar/concrete [39][87][88] exposed to the temperature conditions ranging from 20°C to 40°C. Regarding the temperature peak value shown in the relation between temperature and steel corrosion rate in previous literature, Abdulrahman et al. [89] stated an increase in corrosion mass loss of steel in chloride-containing concrete from 30°C to 40°C and then decreases at 50°C temperature conditions under 85%RH conditions; V.Zivica et al.[53] also reported a significant decrease in the corrosion rate of steel rebar in chloride-containing mortar when the temperature was over 40°C under 90% RH. Nevertheless, neither of these studies considered the role of water content in the temperature effect on the corrosion behavior of steel and did not verify the reason for such attenuation of the corrosion rate. In addition, to the best of our knowledge, there has been no discussion of the temperature peak value of corrosion rate in carbonated mortar. In the current experiments, the temperature peak values were 40°C in carbonated mortar under higher RH conditions (Figure 3.12). The decrease in the corrosion rate of steel when the temperature was above the peak temperature could be attributed to the decrease in the concentration of dissolved oxygen in the electrolyte. According to the Nernst equation Eq. (3.14), the decreased concentration of dissolved oxygen leads to a reduction in the cathodic reversible potential  $E_c^0$ , the difference in reversible potential between the anode and

## EFFECT OF RELATIVE HUMIDITY AND TEMPERATURE ON STEEL CORROSION IN CARBONATED MORTAR

cathode decreases, which represents the driving force of the corrosion reaction, thus resulting in a decrease in the corrosion rate.

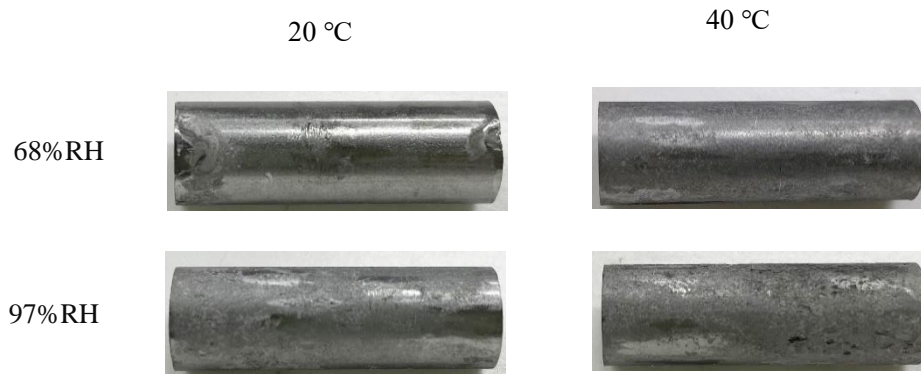


Figure 3.22 Steel rebar removed from carbonated mortar under 68% RH, 97% RH and 20 °C, 40 °C



Figure 3.23 Corrosion products removal procedure following standard systematic step

Figure 3.22 shows the steel rebar removed from carbonated mortar under 68%RH and 97%RH with a lower temperature of 20°C and higher temperature of 40°C conditions, and then the rust on the surface was chemically and ultrasonic cleaned following standard systematic step [90] as shown in Figure 3.23: immerse the steel rebars in a specific solution (1000 mL hydrochloric acid, 20g antimony trioxide and 50 g stannous

## EFFECT OF RELATIVE HUMIDITY AND TEMPERATURE ON STEEL CORROSION IN CARBONATED MORTAR

chloride), which is designed to remove the corrosion products with the minimal dissolution of any base metal. It can be observed that the corrosion state and corroded surface of steel rebar are the most serious and larger at 40 °C and 97%RH than the others, which is consistent with the corrosion rate results shown in Figure 3.12 and Figure 3.13.

### 3.4.3 Corrosion controlling mechanism of carbonation-induced corrosion

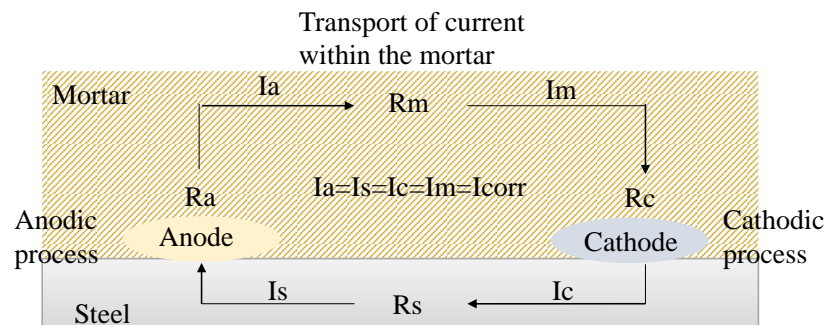


Figure 3.24 Steel corrosion propagation in concrete

For the corrosion control mechanism, the propagation of steel corrosion embedded in mortar is an electrochemical reaction consisting of four separate processes, as shown in Figure 3.24: the anodic process, transport of current within the mortar, cathodic process, and transport of current within the steel. Each step represents the resistance against the current flow in the system. The resistance was connected in series, and consequently, the highest resistance limited the corrosion current. The current flow resistance through the steel ( $R_s$ ) was low compared to the other three processes. Accordingly, either the cathodic ( $R_c$ ), anodic ( $R_a$ ), or mortar resistance ( $R_m$ ) limits the corrosion rate, which depends on the environmental and material properties. As the corrosion of steel was initiated by the carbonation and the chloride content, the step-limiting corrosion can be deduced from the correlation between the corrosion potential and the corrosion rate of steel rebar, and the correlation between the electrical resistivity of the mortar and the corrosion rate.

## EFFECT OF RELATIVE HUMIDITY AND TEMPERATURE ON STEEL CORROSION IN CARBONATED MORTAR

Evans diagrams in Figure 3.25 show the two corrosion controlling mechanisms. Figure 3.25 (a) illustrates the resistive control where the corrosion rate increases from  $I_{corr}$  to  $I'_{corr}$  when the resistance decreases from  $R$  to  $R'$ . Since the increase of water content facilitates the anodic process, the anodic Tafel slope decreases[91][41], leading to the anodic branch changing from line I to line II. Correspondingly, the corrosion potential shift to more negative from  $E_{corr}$  to  $E'_{corr}$ . Such a negative correlation between corrosion rate and corrosion potential can be found in carbonated mortar (see from Figure 3.14), which indicates that the corrosion process is under resistive control in the specified environmental conditions. Similar correlation between corrosion rate and corrosion rate were also reported in several papers[92][93]. Figure 3.25 (b) illustrates the cathodic control where the corrosion rate decreases from  $I_{corr}$  to  $I'_{corr}$  with the corresponding changes in the corrosion potential from  $E_{corr}$  to  $E'_{corr}$ , which are resulted from the cathodic depolarization, leading to the cathodic branch changes from line III to line IV. From Figure 3.14, the phenomenon that corrosion potential decreased with the decreased corrosion rate occurred under 91%, 94% and 97%RH with 45°C and 50°C in carbonated mortar, which indicates the corrosion processes were under cathodic control.

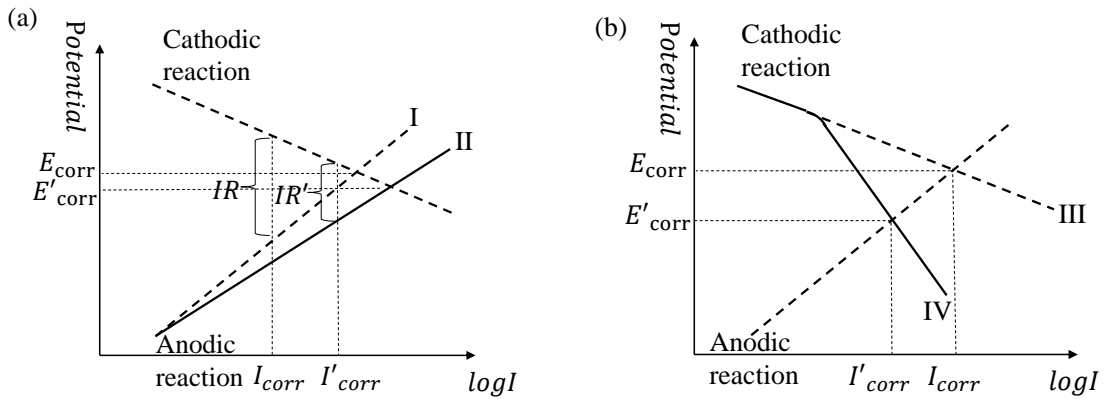


Figure 3.25 Evans diagrams of the corrosion processes controlled by resistive control(a)  
and cathodic control(b)

## EFFECT OF RELATIVE HUMIDITY AND TEMPERATURE ON STEEL CORROSION IN CARBONATED MORTAR

In addition, as shown in Figure 3.26, the strongly correlated linear relationship between the corrosion rate and the reciprocal of electrical resistivity indicates that the corrosion process is under resistive control in most environmental conditions, as suggested by several authors [94][91][95]. However, the temperature effect is scarcely discussed. Some corrosion processes were under cathodic control owing to the limitation of oxygen supply when the temperature was over 40 °C with high water content states, which are circled by dashed lines in the figure. The regression dashed line was presented in Figure 3.27 when corrosion process is under resistive control in carbonated mortar as:

$$\log i_{corr} = 2.12 \times \log \left( \frac{1}{R} \right) + 7.48 \quad (3.15)$$

$$i_{corr} = 10^{2.12 \times \log \left( \frac{1}{R} \right) + 7.48} \quad (3.16)$$

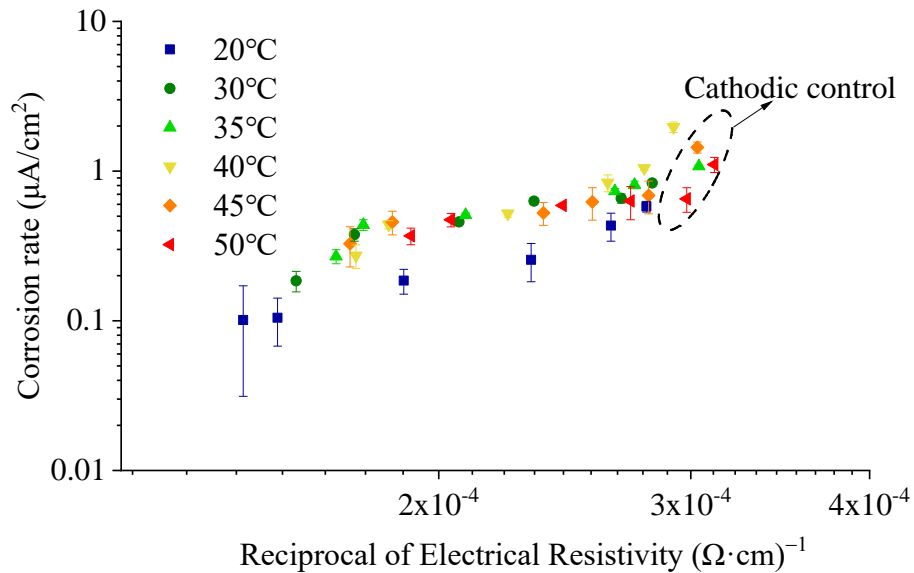


Figure 3.26 Relationship between reciprocal of electrical resistivity and corrosion rate in carbonated mortar

## EFFECT OF RELATIVE HUMIDITY AND TEMPERATURE ON STEEL CORROSION IN CARBONATED MORTAR

Such a resistive controlling mechanism of the corrosion process can be applied in the estimation of the corrosion rate of steel rebars under different environmental conditions using the relationships among the electrical resistivity of cement materials in RC structures, water content, and temperature. For the linear relationship between the logarithm of the electrical resistivity ( $\log R$ ) and the reciprocal of temperature ( $1/T$ ), the electrical resistivity ( $R_0$ ) of mortar at 20 °C (273.15K) can be used as the initial value of the line, whereas the slope is determined by activation energy  $E_{app}$  (Eq. (3.10)). First, the estimation equations for  $R_0$  in the carbonated mortar can be derived using the water content  $w$  as the independent variable:

$$R_0 = 6224w^{-0.39}, R^2 = 0.97 \quad (3.17)$$

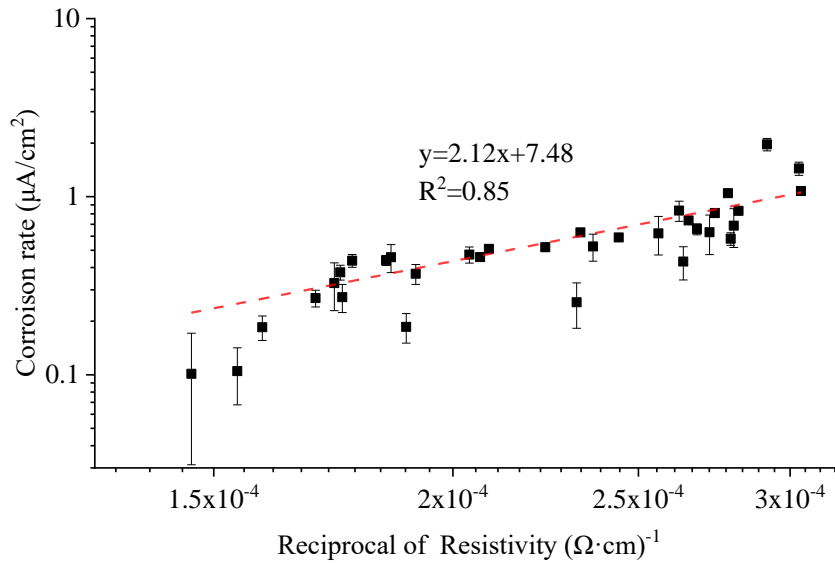


Figure 3.27 Relationship between reciprocal of electrical resistivity and corrosion rate

Second, following the relationship between the  $E_{app}$  of electrical resistivity and water content  $w$  in the carbonated mortar (Figure 3.19), the value of  $E_{app}$  can be determined by the expressions below:

## EFFECT OF RELATIVE HUMIDITY AND TEMPERATURE ON STEEL CORROSION IN CARBONATED MORTAR

$$E_{app} = 10.3w^{-0.43}, R^2 = 0.99 \quad (3.18)$$

In the end, with the known values of the initial value  $R_0$  at 20 °C (273.15K) and apparent activation energy  $E_{app}$ , the electrical resistivity of carbonated mortar can be calculated for the given water content and temperature; consequently, the corrosion rate of steel rebar exposed to variable environmental conditions can be estimated following the linear relationship between corrosion rate and the reciprocal of electrical resistivity by Eq. (3.16).

Having determined the corrosion rate, the residual service life of corrosion distressed RC structure can be approximately assessed by calculating the remaining time at which the radial expansion of rust on the periphery of rebar would produce cracks through the cover.

This calculation procedure, which should be expanded and validated by other steel rebar types, cement types, and mixture proportions, can be applied to estimate the corrosion rate, which can be used as a fundamental value for the soundness evaluation of reinforced concrete members whose relationship between the corrosion amount and performance of the member is known. In other words, the calculation procedure can be applied to estimate the service life of reinforced concrete members.

### 3.5 Summary

This section clarified the RH and temperature dependence of carbonation-induced corrosion behaviors by considering the microstructure and water content of mortar. The conclusions are summarized as follows.

For carbonation-induced corrosion, the decreasing trend of the electrical resistivity of carbonated mortar and the increasing trend of the corrosion rate of steel occurred with increasing temperature and RH conditions because of the mobile ions in the pores and the increased condensed electrolyte. The temperature dependence of electrical



## EFFECT OF RELATIVE HUMIDITY AND TEMPERATURE ON STEEL CORROSION IN CARBONATED MORTAR

resistivity decreased with increasing water content in the mortar. The turning point of RH was 94%, where a significant increase in corrosion occurred owing to the interconnectivity of electrolytes and the decreased anodic reversible potential. The temperature peak value for the increase in corrosion rate was 40 °C under high RH conditions, caused by the decreased dissolved oxygen content.

The corrosion control mechanisms were verified by the correlation between the corrosion potential and corrosion rate of the steel rebar, and the correlation between electrical resistivity of the mortar and the corrosion rate. The linear relationship between the reciprocal of electrical resistivity and carbonation-induced corrosion rate, and the increase of the corrosion rate with the corrosion potential shifting more negatively indicate that the corrosion process in carbonated mortar is under resistive control in most cases. The cases of corrosion process under cathodic control under specific conditions can also be verified by the decreased corrosion rate of steel rebar accompanying a negative shift of corrosion potential.

The linear regression trend line of the data detected in the carbonated mortar roughly indicates that the corrosion process is under resistive control. The regression analysis model of the electrical resistivity of cement materials enables an engineering application to estimate the corrosion rate of steel rebars under different exposure conditions. The linear correlation between the reciprocal of the electrical resistivity of the mortar and the corrosion rate of the steel rebar can be established when the corrosion process is under resistive control within specific exposed conditions. In this section, the resistive controlled corrosion process was under 68% to 84%RH with temperatures ranging from 20°C to 50°C, and 91% to 97% RH with temperatures ranging from 20°C to 40°C for carbonation-induced corrosion. In addition to measuring the electrical resistivity of mortar in the field, the corrosion rate can also be obtained by estimating the electrical resistivity of mortar based on the water content and exposure temperature. Our study provides an idea for estimating the service life of reinforced concrete members with the known relationship between the corrosion amount and performance

## EFFECT OF RELATIVE HUMIDITY AND TEMPERATURE ON STEEL CORROSION IN CARBONATED MORTAR

of the member. Future work will focus on validating cement type, steel type, mix proportions, and chloride content.

In addition, as another main cause of corrosion initiation factor, the effect of RH and temperature on chloride-induced corrosion behaviors are presented in APPENDIX C, the sample design and electrochemical measurement process are the same as the carbonated mortar sample in Chapter 3. Finally, the estimation method for chloride-induced corrosion rate is proposed according to the controlling mechanism of the corrosion process.

## EFFECT OF COVER THICKNESS ON CARBONATION-INDUCED CORROSION RATE

### 4. EFFECT OF COVER THICKNESS ON CARBONATION-INDUCED CORROSION RATE

#### 4.1 Introduction

Since cover thickness plays an essential role in protecting from reinforcement corrosion in RC members[2], the minimum cover thicknesses are specified according to exposed environmental conditions or locations as shown in Table 4.1 and Table 4.2 in [96][97]:

Table 4.1 The standard minimum cover thickness in RC members in JASS 5[96]

RC members location			No finish	With finish
The parts that do not touch the soil	Roof slabs	Exterior	30	20
	Floor slab	Interior	30	20
	Non-strength bearing wall	Exterior	30	30
		Interior	40	30
	Protective wall		40	40
The parts touch the soil	Columns			
	Beams		40	40
	Floor slabs			
	Load-bearing wall			
	Foundation, Retaining wall		60	60

Table 4.2 The standard minimum cover thickness in RC members in JSCE[97]

Conditions	Slab	Beam	Column
Not exposed to wind and rain	10	15	20
Important structures with big size and exposed to wind and rain	20	25	30
Locations without an effective protective layer under the chemical ingress of smoke, acid, oil, and salts	30	35	40

Therefore, the thickness of cover layer in real RC structures are varied from 10 mm to 40 mm, though cover thicknesses sometimes are thinner than standard values due to the casting or construction errors. Therefore, the corrosion rate predicted followed by the proposed equations (refer to Eq.(3.16)) based on the experiment results with cover thickness of 5 mm in Chapter 3 may be overestimated due to the inhibiting effect of cover layer on steel corrosion. This section is to clarify the role of cover thickness plays

## EFFECT OF COVER THICKNESS ON CARBONATION-INDUCED CORROSION RATE

in steel corrosion under different RHs and temperatures, and proposes a more precise and conservative corrosion rate prediction equation with the consideration of the effect of cover thickness based on the results of with a cover thickness of 5 mm in Chapter 3

### 4.2 Experimental procedure

#### 4.2.1 Material and specimen

The mortar used for all specimens was cast with the mixture proportions presented in Table 4.3 with a water/cement ratio of 0.6. Polypropylene fibers (length of 6 mm, diameter of 0.028 mm) were used to prevent cracking in the mortar cover caused by the shrinkage caused by drying and carbonation.

Table 4.3 Mix proportions of mortar

W/C (%)	S/C	Water (kg/m <sup>3</sup> )	OPC cement (kg/m <sup>3</sup> )	Sand (kg/m <sup>3</sup> )		Fiber (kg/m <sup>3</sup> )
				1.7-0.2 mm	< 0.2 mm	
60	2	355	593	593	593	0.91

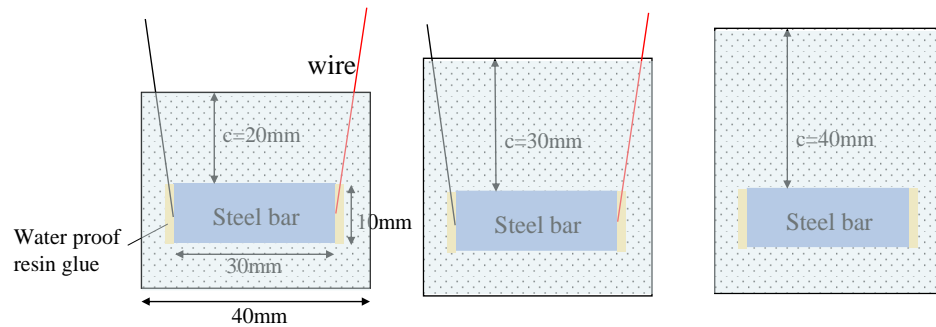


Figure 4.1 The schematic diagram of the mortar specimen with different cover thicknesses

Reinforced mortar samples were prepared with Ø10mm rebar (SGD-400D) placed in 20×40×50 mm<sup>3</sup>, 20×40×60 mm<sup>3</sup>, and 20×40×70 mm<sup>3</sup> molds with cover thicknesses of 20 mm, 30 mm, and 40 mm as shown in Figure 4.1. Copper wires were welded as the

## EFFECT OF COVER THICKNESS ON CARBONATION-INDUCED CORROSION RATE

electrical connection on both sides of the rebar. The welds were protected with waterproof glue, and the rebar surface area of  $9.42 \text{ cm}^2$  was exposed to mortar.

### 4.2.2 Accelerated carbonation and environmental condition control

After casting for 24 hours, the specimens were removed from the molds and sealed in a curing room at  $20 \pm 2 \text{ }^\circ\text{C}$  for 28 days. After the curing period, all specimens were transferred to an oven at  $105^\circ\text{C}$  until they reached a constant weight, then placed in an accelerated carbonation chamber with the condition of 5%  $\text{CO}_2$ , 60% RH, and  $20^\circ\text{C}$ . All the specimens were taped with waterproof tape on the surfaces except the top surface to allow the  $\text{CO}_2$  can penetrate only from one direction, as Figure 4.2 shows. Meanwhile, reference unreinforced specimens under the same conditions were prepared to verify the carbonation depth by a phenolphthalein test during the accelerated carbonation duration.

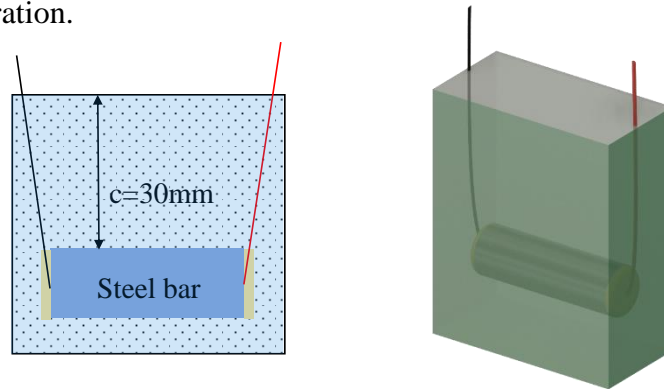


Figure 4.2 Mortar samples taped by waterproof tape

As carbonation depth reached each cover thickness, the mortar specimens were subject to the four RH conditions controlled by KCl (84%RH),  $\text{BaCl}_2$  (91%RH),  $\text{KNO}_3$  (94%), and  $\text{K}_2\text{SO}_4$  (97% RH) saturated solution in sealed cases and three temperatures ( $20^\circ\text{C}$ ,  $30^\circ\text{C}$ ,  $40^\circ\text{C}$ ) controlled by the chamber until the mass equilibrium of samples was reached.

### 4.2.3 Electrochemical measurement

Corrosion current density ( $i_{\text{corr}}$ ) measurement was performed using an electrochemical potentiostat (HOKUTO HZ-7000). The electrochemical impedance spectroscopy (EIS) method was performed using a 10mV amplitude sine wave signal ranging from 0.1 Hz

## EFFECT OF COVER THICKNESS ON CARBONATION-INDUCED CORROSION RATE

to 100 kHz with twenty points per decade. The charge transfer resistance was measured with a three electrodes cell setup (Ag/AgCl is the reference electrode, stainless plate acts as a counter electrode, rebar acts as a working electrode) and used for calculation of corrosion current density by the Stern-Geary equation.

For the electrochemical experiment under higher temperatures than room temperature, the samples are emerged into a water bath (AS ONE TB-1N), setting the requested temperatures to keep the temperature during the measurement duration. The heat transfer medium is the saturated sponge between the mortar sample and the water bath. The setup is shown in Figure 4.3.

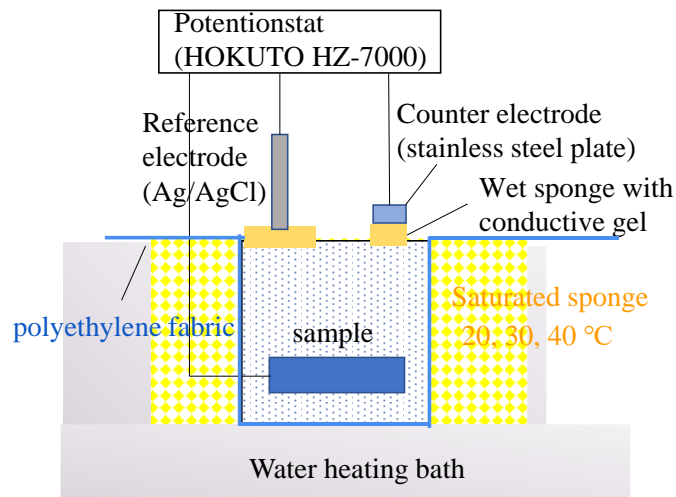


Figure 4.3 Setup of sample in water heating bath

### 4.3 Experimental results of corrosion rate of steel rebar in the carbonated mortar with different cover thicknesses

Figure 4.4 shows the relationship between the corrosion rate of steel with four different cover thicknesses and four RH conditions for each thickness at 20°C (corrosion rate data of steel rebar with a cover thickness of 5 mm is taken from the experiment in Chapter 3). It is obvious that the corrosion rate of steel with a 5 mm cover thickness is much higher than the other cover thicknesses. From the relationship between the corrosion rate of steel rebar and RH at every temperature condition with four cover

## EFFECT OF COVER THICKNESS ON CARBONATION-INDUCED CORROSION RATE

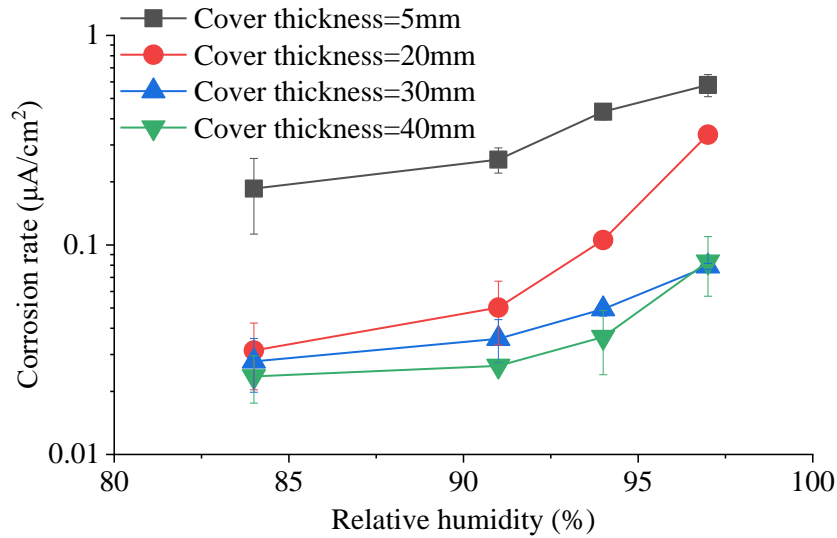


Figure 4.4 Corrosion rate of rebar with different cover thicknesses under different RH conditions under 20°C

thicknesses shown in Figure 4.5, the corrosion rate increased remarkably when RH was higher than 90% regardless of the cover thickness. Furthermore, it should be noticed that when cover thickness increases from 5 mm to 40 mm, the difference in corrosion rate at different temperature conditions reduces with increasing cover thickness.

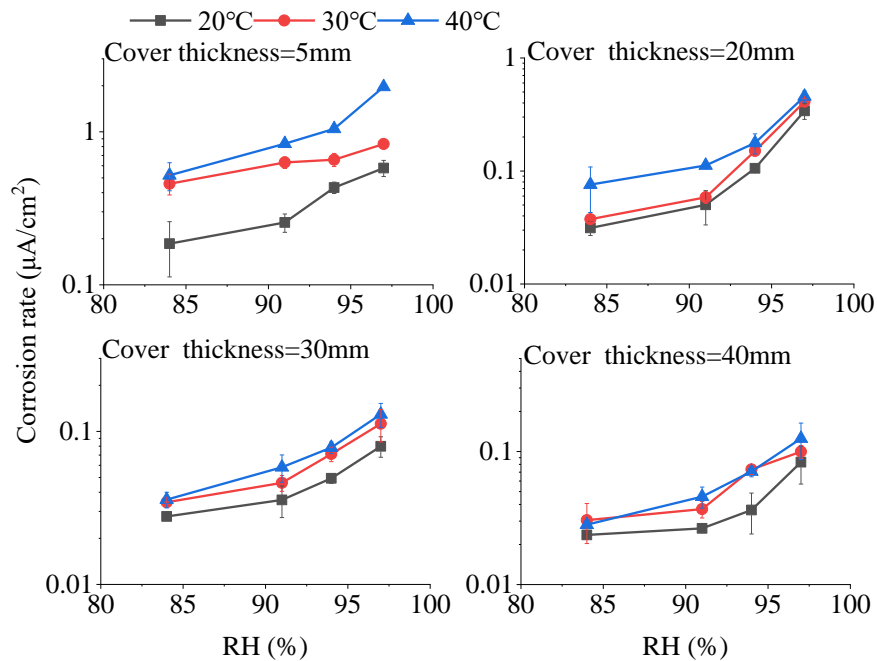


Figure 4.5 Relationship between corrosion rate and RH with four cover thicknesses

## EFFECT OF COVER THICKNESS ON CARBONATION-INDUCED CORROSION RATE

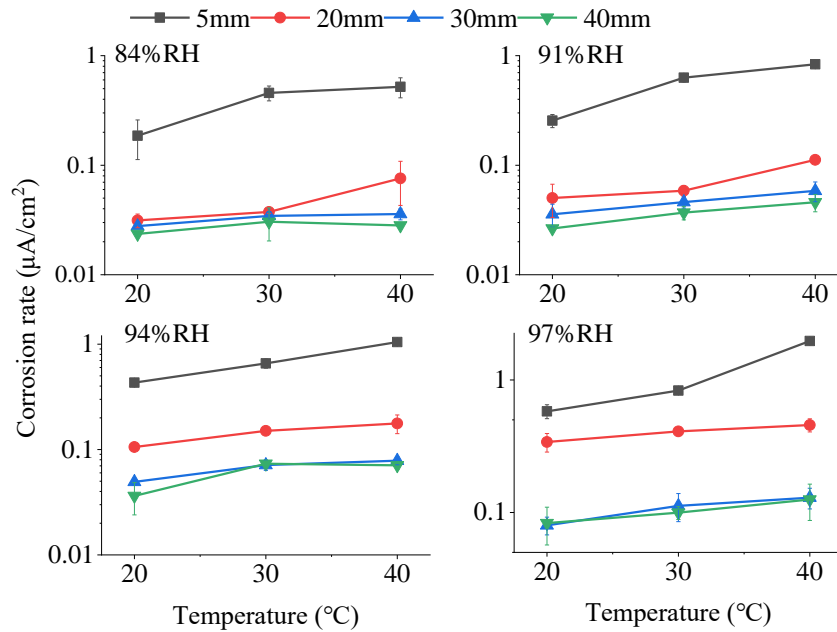


Figure 4.6 Relationship between corrosion rate and temperature with four cover thicknesses

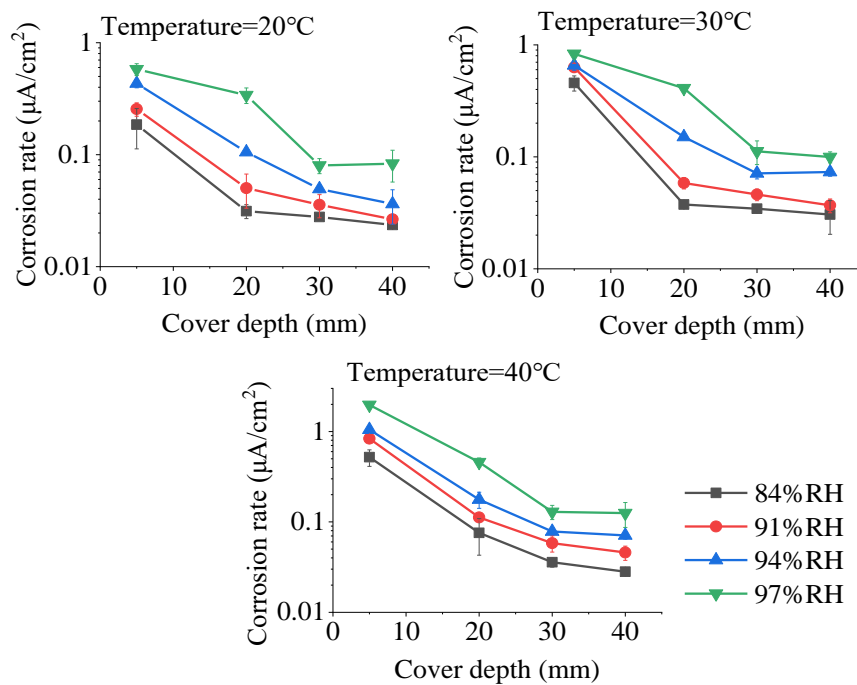


Figure 4.7 Effect of cover thickness on corrosion rate under different RH and temperature conditions



## EFFECT OF COVER THICKNESS ON CARBONATION-INDUCED CORROSION RATE

Figure 4.6 shows the relationship between the corrosion rate of steel rebar and temperature with four different cover thicknesses. It shows that when the temperature increased from 20°C to 40°C, the corrosion rate increased under each RH condition and cover thickness. It is obvious that the corrosion rate of steel rebar with 30 mm cover thickness was similar to that with 40 mm cover thickness.

In summary, Figure 4.7 shows the effect of cover thickness on corrosion rate under different RH and temperature conditions.

### 4.4 Discussion

#### 4.4.1 Effect of RH and temperature on corrosion rate with different cover thicknesses

The corrosion rate of steel rebar decreases with the increase in cover thickness (refer to Figure 4.4), which was caused by the increase in the effective thickness of the diffusion layer for the oxygen and water content. As a result, the supply of oxygen and water content on the steel surface is inadequate for cathodic reaction, slowing the corrosion rate. For the effects of RH on corrosion rate with four cover thicknesses (refer to Figure 4.5), corrosion rate increases significantly when RH is higher than 90% due to the increase of condensed water content and interconnectivity of electrolyte as mentioned in Chapter 3, where the ions transport and channels increase, then the corrosion process is promoted. For the increasing effect of temperature on the corrosion rate of steel rebar with four cover thicknesses (refer to Figure 4.6), the elevating temperature increases the ion mobility of electrochemical reaction and the diffusion of oxygen[52], then promoted the corrosion process.

The difference between corrosion rate getting smaller with increasing cover thickness, and the corrosion rate values getting similar for the cover thicknesses of 30 and 40 mm indicate that the effects of RH and temperature on corrosion rate decrease as the cover thickness increases. It is because the water content and oxygen penetration in mortar would remain at a depth ranging from 30 mm to 40 mm[98]. In other words, an adequate

## EFFECT OF COVER THICKNESS ON CARBONATION-INDUCED CORROSION RATE

cover thickness of around 30 to 40 mm could inhibit the penetration of water content and oxygen.

### 4.4.2 Prediction of corrosion rate considering the cover thickness

Based on the relationship between the corrosion rates with the different cover thicknesses and the corrosion rate prediction method proposed in Chapter 3, a more precise and empirical corrosion rate prediction method considering cover thickness can be derived. Since the highest corrosion rate of steel rebar in carbonated mortar shows at 97%RH and 40°C in this experiment, and the changing trends are similar no matter what RHs and temperatures are (refer to Figure 4.5), to ensure the safety of corrosion evaluation, these highest values are used as the representative values when considering the effect of cover thickness. Figure 4.8 shows the highest corrosion rate ( $i_{corr}$ ) data with different cover thicknesses ( $D$ ), and the equation in the figure was determined by allometric curve fitting.

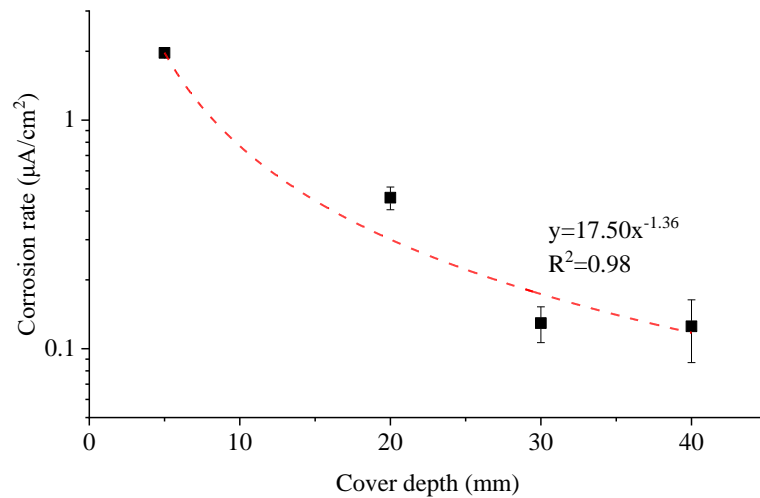


Figure 4.8 Corrosion rate under 97%RH and 40°C with allometric fitted curve

The relationship between the corrosion rates of 5 mm cover depth and another cover depth can be calculated as:

## EFFECT OF COVER THICKNESS ON CARBONATION-INDUCED CORROSION RATE

$$Ratio = \frac{i_c}{i_5} = \frac{17.50 \times D^{-1.36}}{17.50 \times 5^{-1.36}} = 8.92D^{-1.36} \quad (4.1)$$

where,

$i_5$ : the corrosion rate value with the cover depth of 5 mm on the fitting curve in Figure 4.8,

$i_c$ : the corrosion rate with a given cover thickness  $D$ .

The ratio to the reference value ( $i_5$ ) will be used in the corrosion rate prediction for the given cover thickness. First, the corrosion rate  $i_r$  of steel rebar with a cover thickness of 5 mm for the given RH and temperature can be predicted (refer to Chapter 3, and the reliability will be verified in Chapter 5). Then the corrosion rate of steel rebar ( $i_{corr,D}$ ) considering the cover thickness ( $D$ ) can be obtained based on  $i_r$  and the ratio calculated by Eq.(4.1) as below:

$$i_{corr,D} = i_r \times Ratio \quad (4.2)$$

In this case, the corrosion rate can be estimated considering the cover thickness more precisely and safely.

Although the enhanced corrosion rate protection model presented in this chapter considered the effect of cover thickness on the corrosion process, the effect of the w/c ratio on the changing trend between corrosion rate and cover thickness was not considered. The effect of cover thickness on corrosion rate is more significant in the mortar with a lower w/c ratio than that with a higher w/c ratio due to the denser microstructure, which inhibits the water content and oxygen diffusion through the cover layer. Therefore, the fitting equation in Figure 4.8 may also be changed. However, it should be mentioned that the estimated corrosion rate of steel rebar in the mortar with a w/c ratio of 0.6 is still conservative and on the safe side.

## EFFECT OF COVER THICKNESS ON CARBONATION-INDUCED CORROSION RATE

### **4.5 Summary**

The increase of cover thickness inhibits the corrosion rate of steel rebar due to the increase of effective diffusion layer for oxygen and water content, causing the lack of oxygen and water content for corrosion reaction. When the cover thickness increases, the effect of RH and temperature on corrosion rate decreases due to the water content and oxygen penetration in mortar would remain at a depth ranging from 30 to 40 mm.

A more precise and safe corrosion rate prediction equation considering the effect of cover thicknesses was proposed based on the relationship of corrosion rates with different cover thicknesses, and the reference values of corrosion rate obtained in Chapter 3.

## VERIFICATION OF CORROSION RATE PREDICTION EQUATION BY CARBONATED SLAG-BASED MORTAR

### 5. VERIFICATION OF CORROSION RATE PREDICTION EQUATION BY CARBONATED SLAG-BASED MORTAR

#### 5.1 Overview

Nowadays, there is a strong trend of using an alternative to Portland cement clinker, substituting a part of the cement with supplementary cementitious materials (SCM). It is desirable that ordinary Portland cement (OPC) is replaced with alternative materials, including blast furnace slag (BFS) and fly ash (FA), with lower carbon dioxide emissions to ensure sustainable concrete production[99]. Some research indicated that SCM exhibited a dense microstructure and the chemical reaction products that can reduce chloride mobility, thus having a high corrosion resistance[100]. However, a reduced capacity to buffer the pH in the alkaline range on exposure to carbon dioxide was reported[101][102][103]. And because the lower pH destroys the passive layer on the steel rebar surface and promotes active corrosion, the protection by the alkaline environment in concrete to avoid corrosion during the service life of a reinforced concrete structure is no longer feasible. Therefore, the corrosion rate of steel rebar in carbonated slag-based material is necessary to be predicted and monitored accurately. This section aims to verify the corrosion rate prediction method proposed in Chapter 3 in applying carbonated slag-based mortar with four different replacement ratios of BFS (30%, 50%, 60%, and 70%) exposed to different RH and temperature conditions.

#### 5.2 Experimental procedure

##### 5.2.1 Materials and proportions

OPC was used throughout the experiment. SCM that BFS was used as a replacement of the weight of the cement with 30%, 50%, 60%, and 70% replacement ratios, denoted by 30SL, 50SL, 60SL, and 70SL, respectively. The chemical compositions of the cement and slag are shown in Table 5.1, while

# VERIFICATION OF CORROSION RATE PREDICTION EQUATION BY CARBONATED SLAG-BASED MORTAR

Table 5.2 shows the mineral composition of OPC. Two sizes of silica sand (UBE INDUSTRIES 5A and 7) with a density of 2.6 g/cm<sup>3</sup> were used as fine aggregate for all mortar mixes. Polypropylene fibers (length of 6 mm, diameter of 0.028 mm) were used to prevent cracking in the mortar cover caused by corrosion products. The water-to-binder ratio (W/B) of 0.60 and sand-to-binder ratio (S/B) of 2 were constant throughout the experimental program. The mortar mix proportions as shown in

Table 5.3.

Table 5.1 Chemical Compositions (%) of the Portland cement and blast-furnace slag

Oxide (wt%)	OPC	BFS
CaO	64.10	43.92
SiO <sub>2</sub>	20.35	33.34
Al <sub>2</sub> O <sub>3</sub>	5.19	14.63
Fe <sub>2</sub> O <sub>3</sub>	2.97	0.26
MgO	1.84	5.74
K <sub>2</sub> O	0.40	0.28
Na <sub>2</sub> O	0.30	0.28
TiO <sub>2</sub>	-	0.54
SO <sub>3</sub>	2.09	-
S	-	0.72
MnO	-	0.14
Cl	0.012	0.005
P <sub>2</sub> O <sub>5</sub>	-	0.01
LOI	2.93	-

Table 5.2 Mineral Composition (wt%) of Ordinary Portland Cement

C3S	C2S	C4AF	C3A	Calcite	Gypsum	Bassanite	Anhydrite	SUM
65.2±0.8	11.9±0.4	11.0±0.6	4.6±0.3	3.2±0.1	2.21±0.3	1.09±0.2	0.32±0.1	99.52

Table 5.3 Mortar mix proportion of slag-based mortar

Mortar	OPC (kg/m <sup>3</sup> )	BFS (kg/m <sup>3</sup> )	Water (kg/m <sup>3</sup> )	Sand (kg/m <sup>3</sup> )		Fiber (kg/m <sup>3</sup> )
				1.7-0.2 mm	<0.2 mm	
30SL	413	177	354	590	590	0.91
50SL	294	294	353	589	589	0.91

## VERIFICATION OF CORROSION RATE PREDICTION EQUATION BY CARBONATED SLAG-BASED MORTAR

60SL	235	353	353	588	588	0.91
70SL	176	411	352	587	587	0.91

### 5.2.2 Sample preparation and environment control

The specimen design (20×20×40 mm) and accelerated carbonation process for slag-based mortar samples are the same as the OPC mortar samples in Chapter 3 except for the mortar mix proportion. As carbonation depth reached the cover depth of 5 mm, the mortar specimens were subject to the three different RH conditions controlled by saturated KCl (84%RH), BaCl<sub>2</sub> (91%), and K<sub>2</sub>SO<sub>4</sub> (97% RH) solutions in desiccators at three temperatures of 20, 30 and 40°C until the mass equilibrium of mortars. The water content by mass  $w$  (%) was calculated after the samples of reference mortar fragments in different RH conditions reached relative humidity equilibrium, given as Eq. (3.1) in Chapter 3.

### 5.2.3 Electrochemical measurement

The electrical resistivity ( $R_\Omega$ ) of mortar and corrosion rate ( $i_{\text{corr}}$ ) of steel rebar were measured using a three-electrode cell setup and a two-electrode setup, respectively. The treatment of the sample and calculation process was described in detail in Section 3.2.4.

### 5.2.4 Characterization of Materials

Since the hydration of slag-based cement paste is much slower than OPC cement paste, it is necessary to determine the hydration degree with a stable value to ensure sufficient hydration after the curing period. The phase compositions were identified by powder X-ray diffraction (XRD), using a RIGAKU Mini Flex diffractometer with Cu  $\alpha$  radiation, using a  $2\theta$  can range of 5°-70° and a scan speed of 2°/min. XRD-Reitveld analysis detected the hydration degree of slag and cement of 30SL and 70SL mortar samples after sixty days' curing to confirm the sufficient hydration achieved before the accelerated carbonation process. The mass fraction of every phase in anhydrous cement was converted from the W/B ratio and BFS replacement ratio. For hydration degree of cement ( $\alpha_c$ ), the phase alite (C<sub>3</sub>S), belite (C<sub>2</sub>S), cubic (C<sub>3</sub>A), ferrite phase (C<sub>4</sub>AF), gypsum, bassanite, anhydrite, and calcite, as well as hydrated phases portlandite and

## VERIFICATION OF CORROSION RATE PREDICTION EQUATION BY CARBONATED SLAG-BASED MORTAR

aragonite were considered in XRD-Reitveld analysis, and  $\alpha_c$  can be expressed by the mass fraction of typical cement minerals ( $C_3S$ ,  $C_2S$ ,  $C_4AF$ , and  $C_3A$ ) as follows:

$$\alpha_c = R_{C_3S} \times (\%C_3S) + R_{C_2S} \times (\%C_2S) + R_{C_4AF} \times (\%C_4AF) + R_{C_3A} \times (\%C_3A) \quad (5.1)$$

where,

$R_a$ : the hydration degree of mineral phase  $a$ .

$\%a$ : the ratio of mineral phase  $a$  in original cement shown in

Table 5.2.

For hydration degree of slag, heat treatment of heating the sample powder to 900°C for 30 min is necessary to crystallize the unreacted slag to Gehlenite ( $C_2AS$ ), Akermanite ( $C_2MS_2$ ), and Merwinite ( $C_3MS_2$ ), which can be quantified by XRD-Reitveld analysis. The hydration degree of the slag ( $\alpha_s$ ) can be calculated by the ratio of the quantified amount of unreacted slag in hydrated slag-based mortar to the amount of slag in the unhydrated mixed cement and slag as follows:

$$\alpha_s = 1 - \frac{\sum'(\%C_2AS + \%C_2MS_2 + \%C_3MS_2)}{\sum(\%C_2AS + \%C_2MS_2 + \%C_3MS_2)} \quad (5.2)$$

where,

$\sum'b$  : the sum of the ratio of mineral phases  $b$  in hydrated materials

$\sum b$ : the sum of the ratio of mineral phases  $b$  in materials before hydration.



## VERIFICATION OF CORROSION RATE PREDICTION EQUATION BY CARBONATED SLAG-BASED MORTAR

### 5.3 Experimental results and discussion

#### 5.3.1 Mortar properties

Table 5.2 shows the hydration degrees of cement and slag in 30SL and 70SL after sixty days' curing period. A higher hydration degree of cement was revealed in 70SL mortar than that in 30SL because the water to cement ratio increases with the increase in the replacement ratio of BFS even at the constant water-to-binder ratio, and the

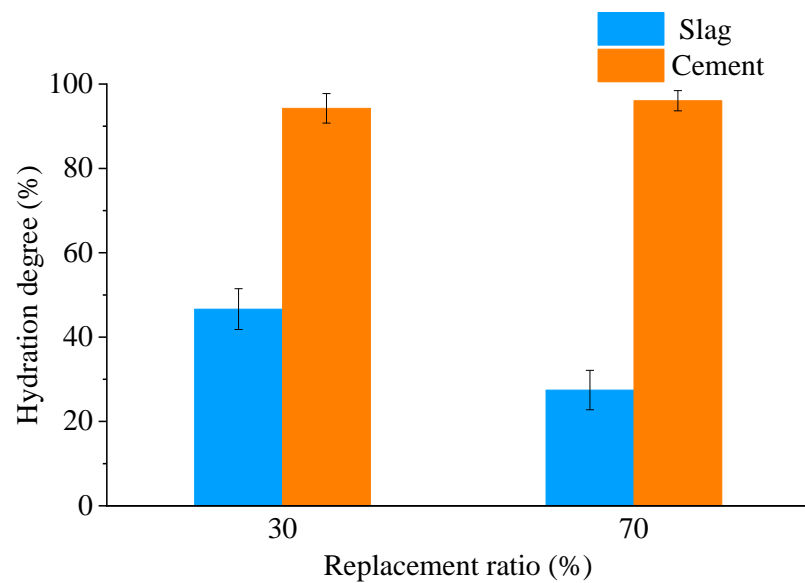


Figure 5.1 Hydration degrees of cement and slag in 30SL and 70SL after 60 days' curing period

precipitation of hydrated product on the BFS surface accelerates the hydration of cement[104]. Both hydration degrees of cement in 30SL and 70SL were over 95%, which indicates a sufficient hydration period for the cement. The hydration degrees of slag of 46.6% and 27.4% occurred in 30SL and 70SL, respectively, suggesting that the hydration degree of slag has a decreasing trend as the slag replacement ratio increases. The hydration degrees of slag in 30SL and 70SL became stable after sixty days' curing period, which can be verified by previous literature [105].

## VERIFICATION OF CORROSION RATE PREDICTION EQUATION BY CARBONATED SLAG-BASED MORTAR

Figure 5.2 shows the results of water content change in carbonated 30SL, 50SL, 60SL, and 70SL with different RH at 20°C. As expected, the water content increases with increasing RH due to the more liquid water condensed in the pores and decreases with increasing temperature due to the higher evaporable pressure. The water content significantly increases when RH is over 91%, attributed to the significantly increased capillary pore volume.

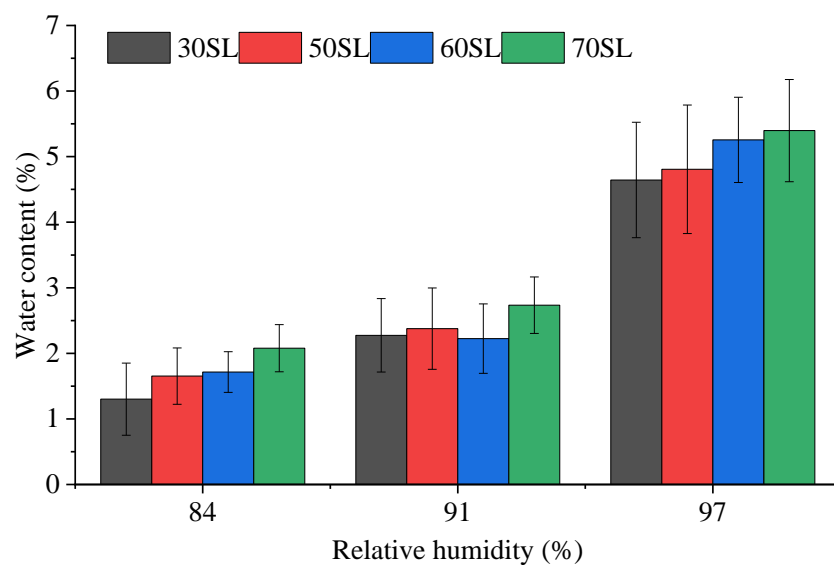


Figure 5.2 Water content of carbonated 30SL, 50SL, 60SL and 70SL at different RH conditions

## VERIFICATION OF CORROSION RATE PREDICTION EQUATION BY CARBONATED SLAG-BASED MORTAR

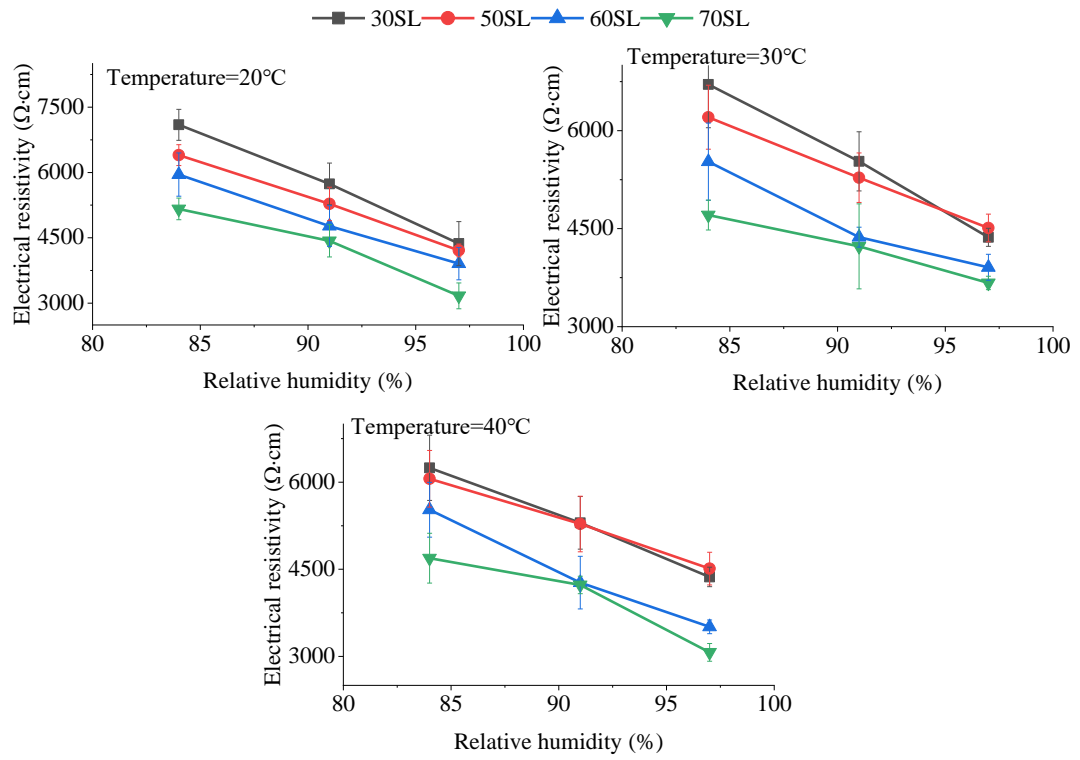


Figure 5.3 Relationship between electrical resistivity of carbonated slag-based mortars and RH under different temperature conditions

## VERIFICATION OF CORROSION RATE PREDICTION EQUATION BY CARBONATED SLAG-BASED MORTAR

### 5.3.2 Electrochemical results of carbonated SCM-based mortar

Figure 5.3 shows the relationship between the electrical resistivity of carbonated slag-based mortars and RH under different temperature conditions. The corresponding corrosion rate of the steel rebar is shown in Figure 5.4.

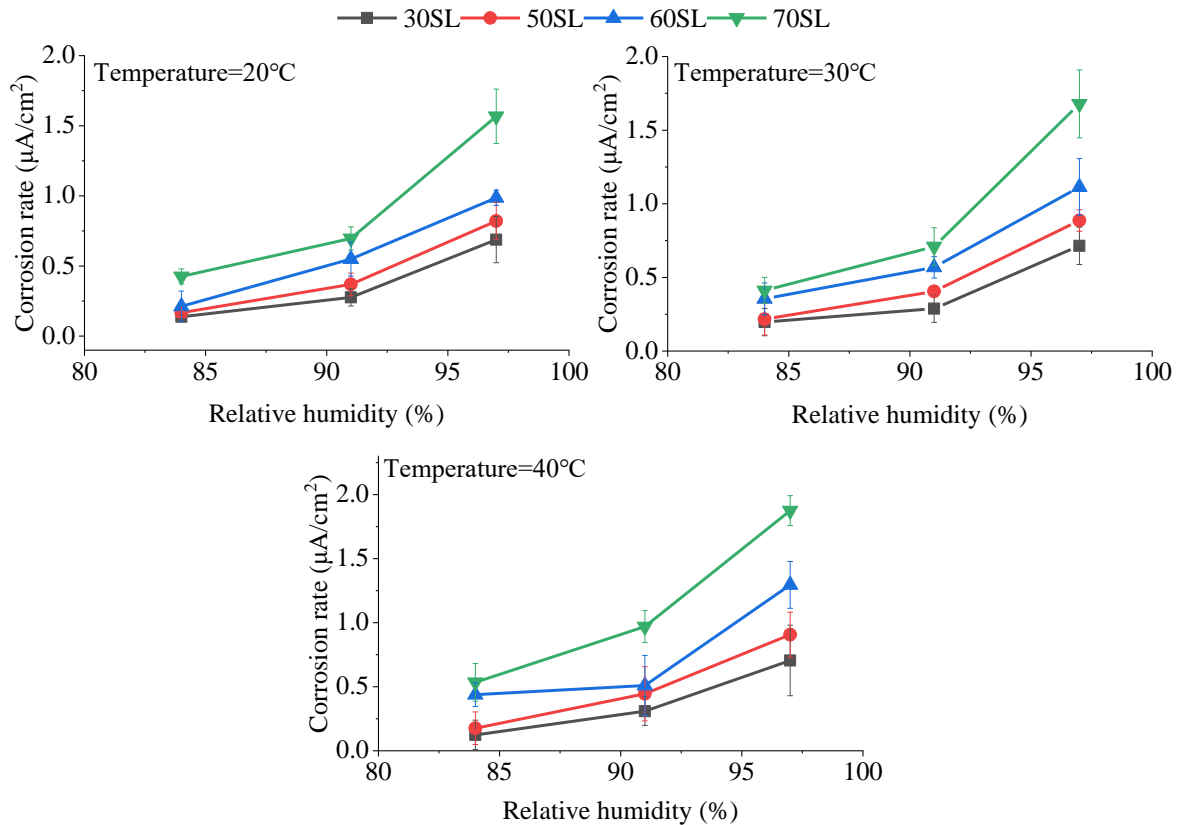


Figure 5.4 Relationship between corrosion rate of steel rebar and RH under different temperature conditions

### 5.3.3 Calculated results and measured results of the electrical resistivity of mortar and corrosion rate of rebar

Since the measurement in the real field is more feasible to be conducted at 20°C, the verification of the electrical resistivity of mortar samples and the corrosion rate of the steel rebar prediction method proceeded under 20°C. Figure 5.5 shows the measured electrical resistivity data of carbonated slag-based mortars under different water content at 20°C.

## VERIFICATION OF CORROSION RATE PREDICTION EQUATION BY CARBONATED SLAG-BASED MORTAR

The apparent activation energy ( $E_{app}$ ) of each water content could be calculated followed Eq.(3.18) (Chapter. 3). The measured initial value of  $R_0$  at 20°C (273.15 K) and the calculated apparent activation energy  $E_{app}$  can be determined as Table 5.4.

Table 5.4 Initial values of  $R_0$  and the calculated apparent activation energy  $E_{app}$  for carbonated slag-based mortar

Carbonated slag-based mortar	RH (%)	Measured values		Calculated value
		Water content (w)	Electrical resistivity at 20°C ( $R_0$ )	Apparent activation energy ( $E_{app}$ ) $E_{app} = 10.3w^{-0.43}$
30SL	84	1.302	7094	9.28
50SL		1.653	6400	8.37
60SL		1.712	5952	8.24
70SL		2.078	5164	7.59
30SL	91	2.274	5736	7.30
50SL		2.376	5280	7.16
60SL		2.224	4770	7.37
70SL		2.735	4430	6.74
30SL	97	4.643	4367	5.37
50SL		4.806	4211	5.29
60SL		5.256	3908	5.09
70SL		5.397	3169	5.03

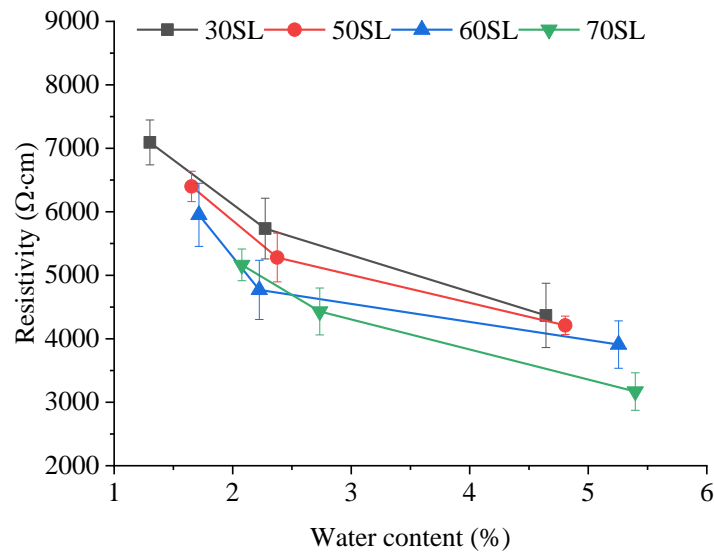


Figure 5.5 Electrical resistivity of carbonated slag-based mortar at different water content under 20°C

## VERIFICATION OF CORROSION RATE PREDICTION EQUATION BY CARBONATED SLAG-BASED MORTAR

Then the electrical resistivity of carbonated slag-based mortar at 30°C and 40°C can be calculated according to the linear relationship between the logarithm of the electrical resistivity ( $\log R$ ) and the reciprocal of temperature ( $1/T$ ) followed by (refer to Figure 3.20):

$$\log(R) = \log(R_0) - \left( \frac{1000 \times E_{app}}{19.14} \right) \times (1/T_0 - 1/T) \quad (5.3)$$

$$R = 10^{\log(R_0) - (52.23 \times E_{app}) \times (1/T_0 - 1/T)} \quad (5.4)$$

A comparison of the electrical resistivity of carbonated slag-based mortar obtained by electrochemical measurement and calculated by Eq. (5.4) is given in Figure 5.6. This shows that there is generally good agreement between measured and calculated data, irrespective of cement types, indicating that the electrical resistivity prediction method proposed in Chapter 3 is reliable for carbonated slag-based material.

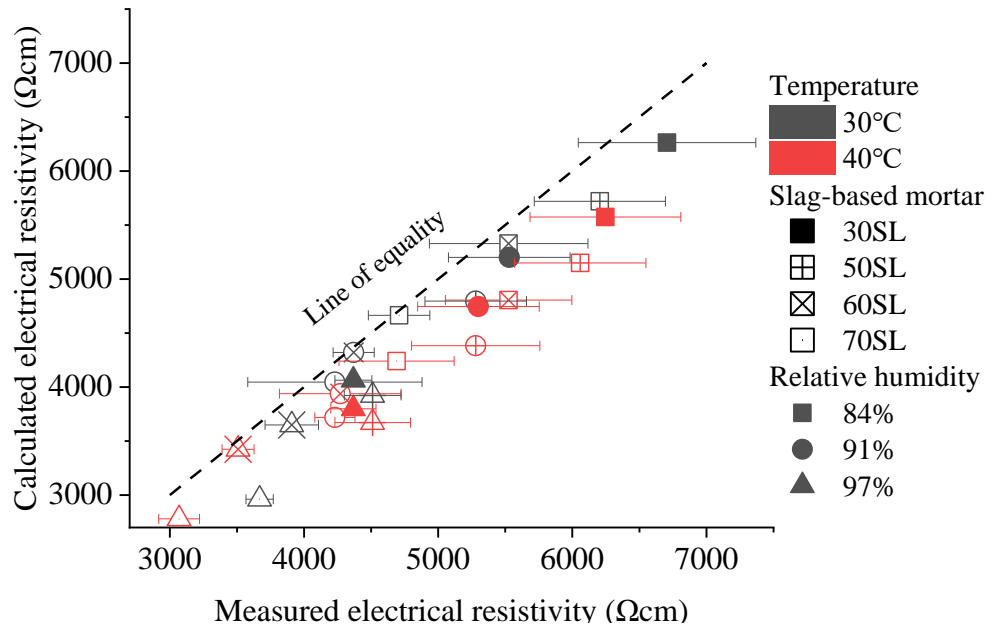


Figure 5.6 Comparison of measured electrical resistivity and predicted electrical resistivity

## VERIFICATION OF CORROSION RATE PREDICTION EQUATION BY CARBONATED SLAG-BASED MORTAR

Consequently, the corrosion rate of steel rebar exposed to variable environmental conditions can be estimated following the linear relationship between corrosion rate and the reciprocal of electrical resistivity in Figure 3.27 by Eq. (3.16).

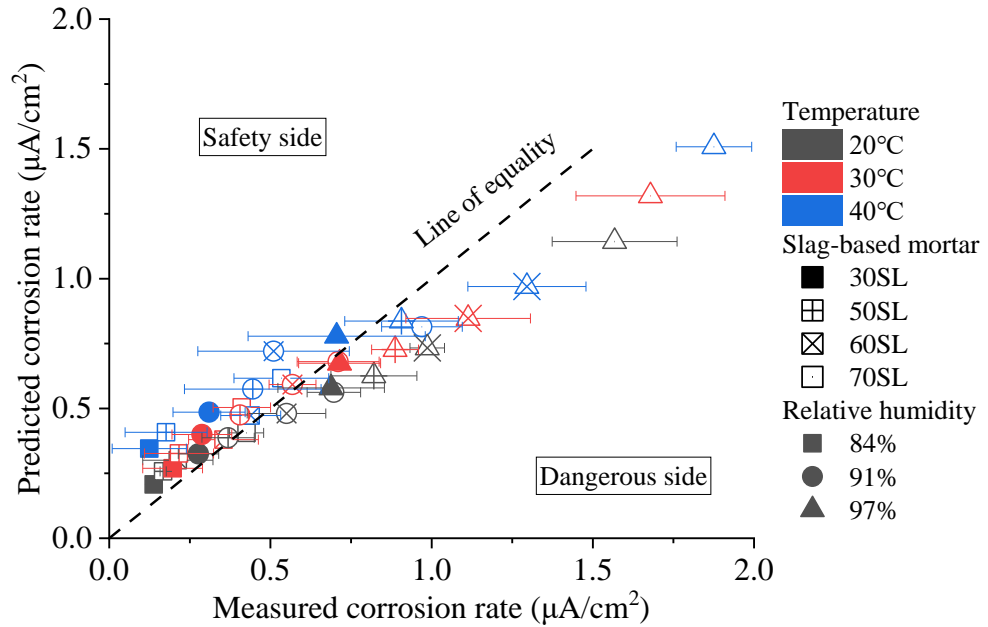


Figure 5.7 Comparison of measured corrosion rate and predicted corrosion rate (measured corrosion rate was overestimated by electrochemical measurement due to the oxidation of sulphide species)

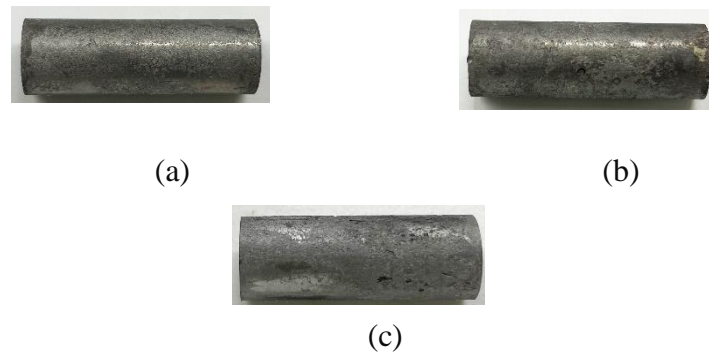


Figure 5.8 Steel rebar removed from the carbonated 60SL (a), 70SL(b) and OPC (c) mortar under 97%RH and 40°C

## VERIFICATION OF CORROSION RATE PREDICTION EQUATION BY CARBONATED SLAG-BASED MORTAR

Figure 5.7 compares the measured corrosion rate and calculated corrosion rate. The part above the equality line is the safety side (predicted corrosion rate values are higher than measured corrosion rate values), and the region below the equality line is the dangerous side (predicted corrosion rate values are lower than measured corrosion rate values). It should be noticed that there is a generally good agreement for 30SL and 50SL, while the corrosion rate values in 60SL and 70SL are falling on the dangerous side and are lack of fitting prediction method, which makes the application of the predicted equation proposed in Chapter 3 is restricted in reinforced slag-based materials. However, Figure 5.8 (a) and (b) show the actual corrosion state of steel rebar surface in 60SL and 70SL under 97%RH and 40°C after the chemical cleaning of the corrosion products followed the steps in[90], and (c) is the surface of steel rebar embedded in carbonated OPC mortar (also show in Figure 3.22 in Chapter 3). The corrosion state of steel rebar in OPC is more serious than in 60SL and 70SL. This means that the corrosion result based on the electrochemical method is not consistent with the corrosion state observed in the steel rebar. Therefore, the electrochemical measurement misinterprets the corrosion behavior and overestimates the corrosion rate. This phenomenon can be explained by the existence of sulfide species ( $S^{2-}$ ,  $S_2O_3^{2-}$ ,  $HS^-$ ) in the pore solution of slag-based mortar. The dissolution and reaction of slag release sulfide ions into the pore solution, which can oxidize into sulfur, consuming locally oxygen on the steel rebar surface. The measured charge transfer resistance ( $R_{ct}$ ) detected in electrochemical measurement will combine the anodic reaction of steel oxidation and sulfide species oxidation. Since the oxidation of reduced sulfide species at the steel rebar surface is not distinguishable from the actual corrosion of steel rebar, so the corrosion rate is overestimated in slag-based materials. Similar misleading results from electrochemical measurement were reported in with a significant decrease of corrosion potential shown in slag-containing material even though no corrosion initiation occurred[106][107][108]. This can also explain that the corrosion rate of steel rebar increases with an increasing replacement ratio of BFS, as shown in Figure 5.4.

The weight loss of the corroded steel rebar after corrosion rust cleaning could correspond to the real corrosion state of the steel rebar. Table 5.5 shows the measured



## VERIFICATION OF CORROSION RATE PREDICTION EQUATION BY CARBONATED SLAG-BASED MORTAR

corrosion weight loss and the corrosion amount calculated from the monitored corrosion rate by electrochemical measurement under 97%RH and 40°C. The average ratio of real corrosion amount to measured corrosion amount is calculated as 0.52, which can be applied to separate the real corrosion rate from the monitored corrosion rate proportionally.

Table 5.5 Comparison between measured weight loss and corrosion amount  
calculated from  $i_{\text{corr}}$

Mortar	60SL	70SL
Measured weight loss (mg)	52.54	94.26
Calculated corrosion amount from monitored $i_{\text{corr}}$ (mg)	113.96	164.98
Ratio	0.46	0.57
Average Ratio	0.52	

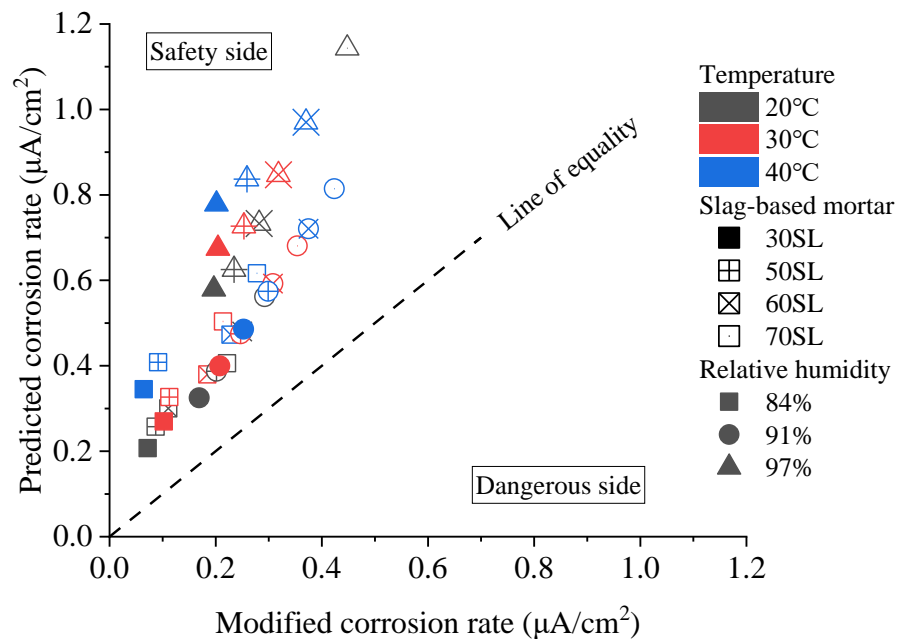


Figure 5.9 Comparison of modified corrosion rate and predicted corrosion rate  
(Real steel corrosion rate can be proportionally separated from the measured  
corrosion rate values)

## VERIFICATION OF CORROSION RATE PREDICTION EQUATION BY CARBONATED SLAG-BASED MORTAR

Figure 5.9 shows the comparison of such modified corrosion rate of steel rebar and the predicted corrosion rate. All the modified corrosion rate values in slag-based mortar fall on the safety side, which indicates that the prediction method of corrosion rate proposed in Chapter 3 is reliable in carbonated reinforced slag-based materials. Furthermore, the detailed and specific oxidation reaction of sulfide species in slag-based material should be further investigated, and appropriate electrochemical measurement methods and calculations for reinforced slag-based materials require consideration.

### 5.4 Summary

The general agreement between the measured corrosion rate data and calculated corrosion rate values shows in 30SL and 50SL, while the measured corrosion rates in cementitious materials with higher replacement ratios of slag (60SL and 70SL) are higher than the predicted values due to the existence of sulfide species oxidation. The electrochemical measure overestimates the corrosion rate of steel rebar in slag-based materials. When the real corrosion rate of steel rebar in slag-based material is separated proportionally from the measured corrosion rate according to the difference between the settle weight loss and calculated corrosion amount from the monitored corrosion rate, modified corrosion rate values are all on the safe side. Therefore, the prediction method of corrosion rate proposed in Chapter 3 is a reliable method for evaluating corrosion behaviors in carbonated slag-based cementitious materials. However, the electrochemical measurement of corrosion behavior and the specific sulfide oxidation reaction for reinforced sulfide-containing mortar should be studied further.

### 6. SOUNDNESS ASSESSMENT FOR RC STRUCTURES

#### 6.1 Motivations

The corrosion rate prediction method has been proposed in Chapter 3 and then can be used as a more accurate prediction method considering the effect of cover thickness in Chapter 4, and its reliability was verified in carbonated slag-based mortar in Chapter 5. Moreover, a soundness assessment for RC members can be proposed based on the corrosion rate prediction method discussed in Chapters 3 to 4.

There are at least two major motivations for assessing the soundness of RC members:

- In a purchase transaction for aged RC buildings, it is necessary for the buyers to capture the overall performance and degradation degree of such old RC members.
- At the request of the building owners, conduct a soundness-related survey, diagnose the deterioration extents and predict the residual service life.

In all the cases, the soundness assessment is requested by owners, users and managers to ensure the safety, maintenance, and preservation of RC buildings.

#### 6.2 Assessment object

The structural properties required for steel rebar in RC members include tensile strength, yield point, cross-sectional area, and attachment strength to concrete. However, the properties needed for RC buildings are not only structural properties, but the safety, habitability, and aesthetics for humans are also important. When cracking or rusty water appears on the concrete surface, it not only affects the aesthetics but also causes panic among the residents. According to the experimental investigations, the structural problems occur at the severe deterioration stage; on the other hand, cracks and rusty water appear at the early stage of the deterioration of RC members[109].

## SOUNDNESS ASSESSMENT FOR RC STRUCTURES

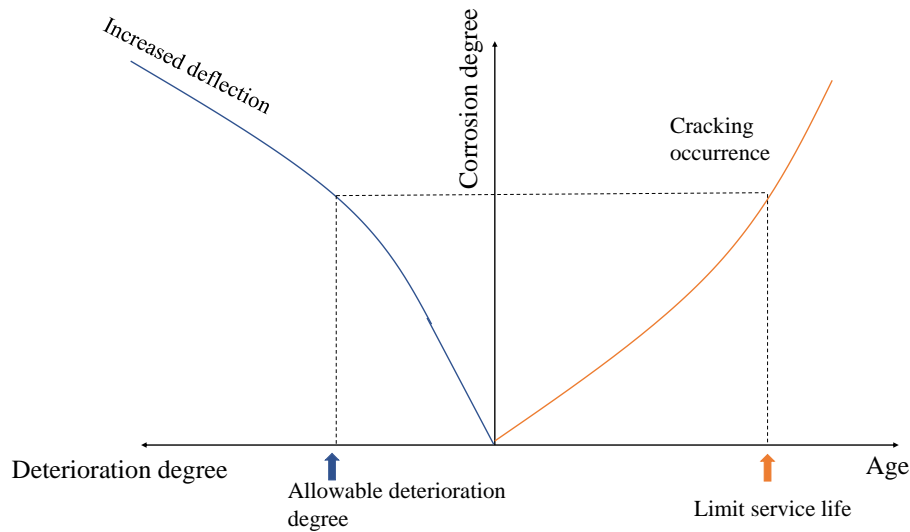


Figure 6.1 Deterioration evolution of RC buildings

As a practical issue, when designers and owners of RC buildings initially receive complaints, they are usually at the stage of deterioration where concrete appears to be cracking or rusty water. If the cover layer of concrete falls off, the falling concrete may cause personal accidents and thus become a social problem, which suggests that the safety and habitability, which are sometimes even more critical than structural properties, should not be ignored. Therefore, for human-occupied dwellings or general buildings, it is reasonable to take the occurrence of cracks in the cover layer of concrete as the allowable deterioration degree and limitation of service life in RC structures, as shown in Figure 6.1.

In the soundness assessment methods described in this chapter, the assessment objects are those concrete members which are affected by carbonation but do not show deterioration in appearance and seem sound.

## SOUNDNESS ASSESSMENT FOR RC STRUCTURES

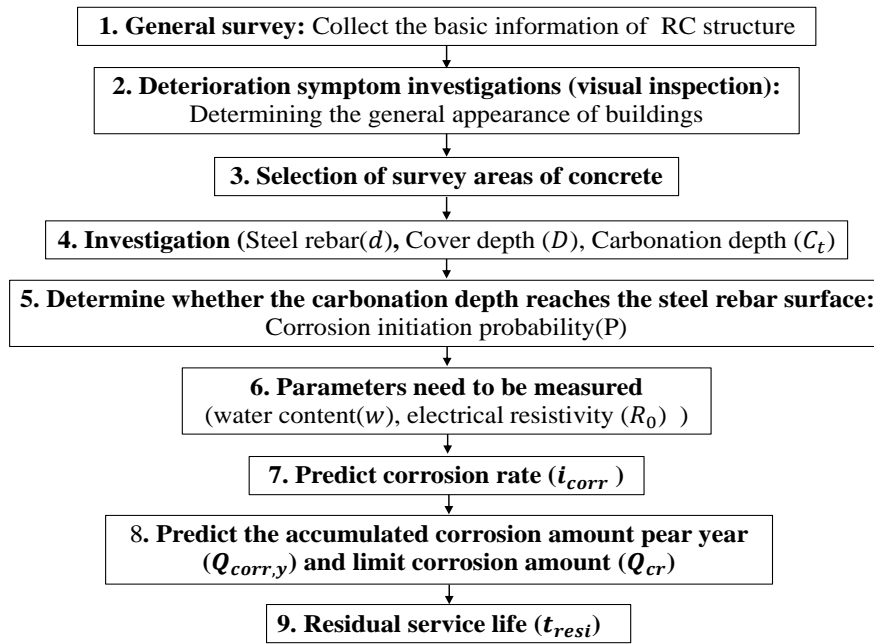


Figure 6.2 Overall soundness assessment process flow

### 6.3 Soundness assessment process

The objective of the soundness assessment of RC buildings is to evaluate the extent of current deterioration and make a prognosis. Figure 6.2 shows the overall flow of the soundness assessment process, and the explanations for each step are presented following.

#### 1. General survey

A general survey for RC buildings is to collect the inherent characteristics, which will be used to investigate the possible causes and process rate of deterioration. The survey items include the scale and construction, usage of the building, elapsed years ( $t_{el}$ ), building drawings, material mix proportions, and finishing types of the buildings. The consideration that the environmental factors are essential for the accurate evaluation of the corrosion rate, and the water content and temperature values depend on the geographic location of the structures and variables due to natural weathering through day-night and seasonal cycles or natural wetting/drying cycles[110][111][112],

## SOUNDNESS ASSESSMENT FOR RC STRUCTURES

therefore, the local meteorological data should be investigated, including local environmental temperature and annual average rainy days.

### 2. Deterioration symptom survey

Deterioration symptom investigation is to investigate whether there are apparent deterioration appearances on the concrete surface and determine the deterioration causes and degrees. The investigation should be conducted visually or with simple instruments such as binoculars, test hammers, etc. Deterioration appearances caused by the carbonation-induced corrosion include rusting (the corrosion products spilling out and adhering to the finish material or concrete surface), cracking (due to expansion pressure of corrosion products, occurring along with the rebar), floating (concrete cover layer is floating due to the expansion pressure of corrosion products.), peeling (floated concrete has been peeled off.), and steel rebar exposure (steel rebars in the concrete exposed due to the falling of the concrete cover layer).

Deterioration of concrete is affected by environmental conditions and the concrete properties and quality. On the other hand, carbonation-induced corrosion is also affected by various environmental factors. Therefore, the carbonation depths and the corrosion states of the rebar should be measured under as many exposed environmental conditions as possible to determine the deterioration stages and corrosion appearance of RC buildings in detail.

Specifically, the concrete members and factors should be investigated in reference to Table 6.1.

Table 6.1 Elements and properties to be considered in selecting survey sites[113]

Elements		Properties
General parts	Locations	Indoors, outdoors, locate directions, wind direction, ocean side or land side, direct rainfall exposure
	Concrete members	Column, beam, wall, floor, eaves, foundation
	Finishing materials	Type, specification, construction period
	Concrete characterization	Aggregate type (normal, lightweight), w/c ratio, construction period (summer/winter)
Defective areas		Cracking areas, joints, rust strain

## SOUNDNESS ASSESSMENT FOR RC STRUCTURES

As mentioned in Section 6.2, the assessment objects focus on those concrete members not showing apparent deterioration in appearance and looking sound. For the concrete members with the obvious deterioration appearances caused by steel corrosion, select the countermeasures according to the deterioration states, as Table 6.2 shows.

Table 6.2 Deterioration states, countermeasures, and standard construction methods[97][114]

Deterioration states	Countermeasures	Standard construction methods
Cracking appearance	Enhanced inspection Repairment	Electric anticorrosion Realkalization Cross-sectional restoration Surface coating
Peeling of concrete occurs with the development of cracks No obvious cross-sectional area loss of steel rebar	Enhanced inspection Repairment Usage limitation	Cross-sectional restoration Surface coating
Peeling of concrete occurs with the development of cracks Loss of cross-sectional area of steel rebar occurs	Repairment Usage limitation Demolition Removal	Cross-sectional restoration Surface coating Copperplate/FPR adhesion

It should be mentioned that the concrete members with the cracks caused by carbonation or drying shrinkage, especially for the interior, should also be included in assessment objects because the water content is not enough to initiate corrosion of steel under drying conditions which are reported in previous research[64][93][115]. Even when the corrosion is initiated when cracking occurs, the formed corrosion products on the steel surface are difficult to penetrate the concrete pores due to the exposure to air, which is accumulated on the steel surface to retard further corrosion process. Therefore, the condition of steel rebar in such RC members is still sound even the cracking appears on the concrete surface.

### 3. Selection of survey areas of concrete

The survey areas of concrete exposed to high RH/temperature conditions should be selected due to their high possibility of corrosion. For the exterior of RC buildings, the concrete members exposed to rainfall directly, including girder support, pole foundation, overhanging slab, the part between adjacent members, concrete near the ground, joints, and auxiliary facilities, may have a higher water content of concrete.

## SOUNDNESS ASSESSMENT FOR RC STRUCTURES

The previous observations of the Japanese structures[2] report that for the elements such as facades and balcony side walls, high moisture conditions occurred due to the exposure to wind-driven rain. The observed local damage at the balcony soffits (sheltered from rain) occurred due to the water access through the water drainage system, which consisted of a gap between the balcony slab and the parapet[116]. For the interior, the concrete parts are often likely to contact water, such as leakage areas; the ceiling in the bathroom, walls, and roof in the kitchen should also be considered.

In addition, concrete members with a low cover thickness or high carbonation depth should be selected due to the high possibility of corrosion initiation. The natural CO<sub>2</sub> concentration exterior is 0.03%, while the CO<sub>2</sub> concentration is 0.1% for the interior, where people gather or use as the oil stoves. In general, the carbonation process rate of the interior concrete members without finishing was estimated to be 1.5 to 3 times higher than that exterior, and the same as the concrete members exterior not exposed to the rainfall. For the concrete interior walls without finishing, it was found that the carbonation depth tended to increase with height. This is because the concrete at the bottom is compacted and dense, while the w/c ratio of concrete above increases due to the bleeding[117].

### **4. Investigation**

After selecting the specific concrete members, the investigation will be conducted, including three necessary parameters: steel rebar diameters, cover thickness, and carbonation depth of concrete.

The diameter of the steel rebar and the cover thickness can be determined using electromagnetic induction, radiometric and electromagnetic wave methods. When there are two layers of reinforcement in the exterior walls or slabs, only the outermost steel rebars can be detected; it is difficult to observe the steel rebars inside. Meanwhile, the cover thickness distribution and the position of steel rebar of concrete members need to be obtained, which will be used in the process of taking cores and corrosion initiation possibility calculation afterward.



## SOUNDNESS ASSESSMENT FOR RC STRUCTURES

For the measurement of carbonation depth, it is necessary to take a core from the selected position. It should be noted that the steel rebar should be avoided according to the results of reinforcement position obtained from radiometric and electromagnetic wave measurements, and the diameter of the core should be as small as possible; the repairs should be conducted immediately right after taking the cores. The detailed process of taking cores is presented in [118]. Wash the surface of the cores after taking, then spray the 1% phenolphthalein solution after it has dried a little bit. The front between the carbonation part and uncarbonated part is obvious and can be identified according to the changed color. If the carbonation is hard to identify, spray the 1% phenolphthalein solution to the holes where the cores are taken from after washing the interior. The detailed process of measuring carbonation depth is presented in [119].

### 5. Determine the limit corrosion initiation probability( $P_0$ )

Suppose we assume that the corrosion of the steel rebar is initiated when carbonation depth reaches the rebar surface. In that case, the relationship between carbonation depth distribution and cover thickness is shown in Figure 6.4. The carbonation depth increases with age, and its variation also increases. On the other hand, the cover thickness of the rebar exists with a certain variation regardless of age. The relationship between the distribution of the carbonation depth progression over time and the distribution of the cover thickness is shown in Figure 6.3 in two dimensions. At certain timing, the distribution of the carbonation depth will partially overlap with the cover thickness distribution, indicating that there is a certain probability of corrosion initiation that carbonation depth has reached the cover thickness[113].

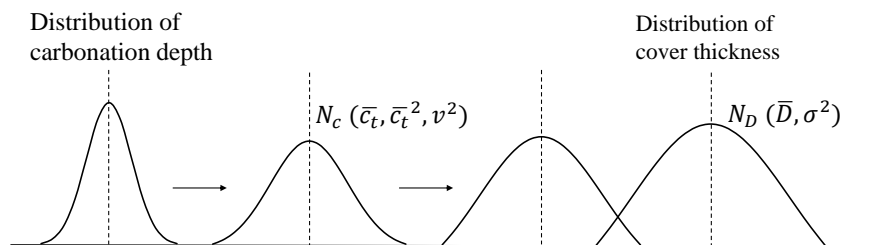


Figure 6.3 The relationship between the distribution of the carbonation depth progression over time and the distribution of the cover thickness

## SOUNDNESS ASSESSMENT FOR RC STRUCTURES

About the calculation of corrosion initiation probability, the distribution of carbonation depth can be expressed as  $N_c(\bar{c}_t, \bar{c}_t^2, v^2)$ , the distribution of cover thickness can be expressed as  $N_D(\bar{D}, \sigma^2)$ , the difference between the distribution of carbonation depth and cover thickness should be  $N_{D-c}[(\bar{D} - \bar{c}_t), (\bar{c}_t^2 v^2 + \delta^2)]$ , and express as (refer to Figure 6.5):

$$f(D - c_t) = \frac{1}{\sqrt{2\pi(\bar{c}_t^2 v^2 + \delta^2)}} \cdot \exp \left[ \frac{-\{(D - c_t) - (\bar{D} - \bar{c}_t)\}^2}{2(\bar{c}_t^2 v^2 + \delta^2)} \right] \quad (6.1)$$

In this case, the corrosion initiation probability (P) evolution with time can be expressed by the probability distribution of carbonation depth with time and cover thickness:

$$P = \int_{-\infty}^0 f(D - c_t) d(D - c_t) \quad (6.2)$$

The value of P represents the ratio of surface area or the total number of the steel rebar corroded by carbonation. The limitation of corrosion initiation probability ( $P_0$ ) is set by considering the importance and safety of the RC structure shown in Table 6.3[120].

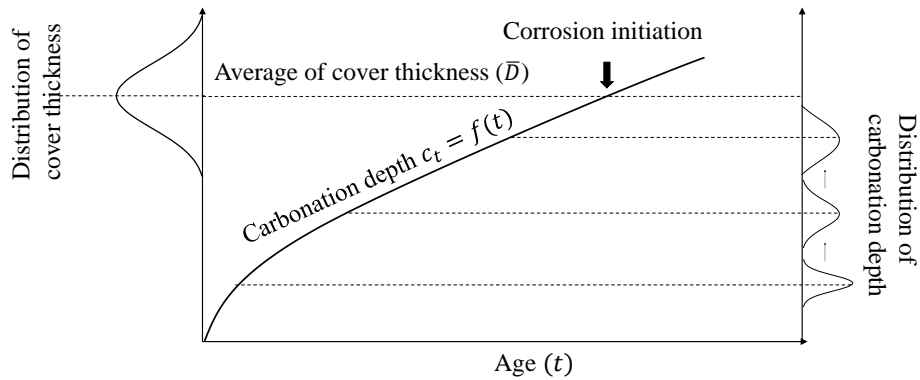


Figure 6.4 Carbonation depth progression and cover thickness

## SOUNDNESS ASSESSMENT FOR RC STRUCTURES

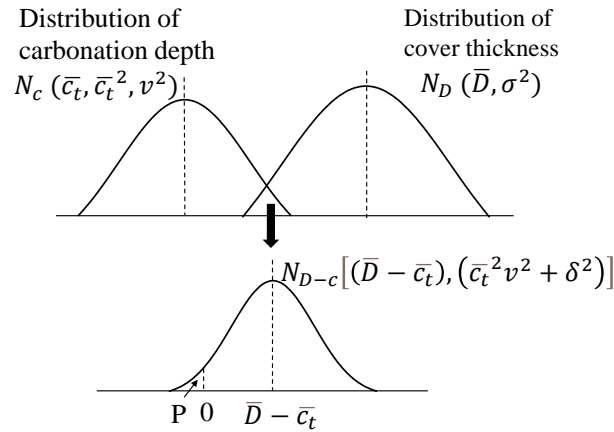


Figure 6.5 Difference between distribution of carbonation depth and cover thickness

Table 6.3 Setting value of $P_0$ considering the number of years of durability			
Reinforcement type	Main reinforcement of columns and beams	Other reinforcement (Hoop bars, stirrup bars, wall bars, slab bars)	
Importance of RC structure	-	yes	no
Very high	<3%	<7%	<15%
High	<5%	<15%	<30%
Normal	<10%	<30%	<50%

### 6. Parameters need to be measured

Before the prediction of corrosion rate, it is necessary to measure the water content ( $w$ ) of concrete or the electrical resistivity ( $R_0$ ) near the steel rebar at 20°C.

The water content of the concrete fragment near the steel rebar should be measured near the water content on the steel rebar surface. The concrete fragment should be saved in an aluminum bag right after taking from the concrete members until the measurement is conducted. The treatment of samples and calculation process has been mentioned in Section 3.2.3 (Chapter 3).

If it is possible, measuring the electrical resistivity of mortar is more precise for predicting the corrosion rate of steel afterward. There are two measurement methods for the electrical resistivity of concrete: the two-point method[66][121] and the four-

## SOUNDNESS ASSESSMENT FOR RC STRUCTURES

point method (Wenner method)[122][123][124]. Either of the two techniques is employed to record the resistance ( $R_c$ ), which is transfer into resistivity ( $R_\Omega$ ) by multiplying it with an appropriate geometrical factor ( $k$ ) with the following equation:

$$R_\Omega = kR_c = k \frac{\Delta V}{I} \quad (6.3)$$

where,

$\Delta V$ : potential difference;

$I$ : injected current.

The two-point measurement should proceed on the concrete cores with a small size or small prism fragment taken near the steel rebar, assuming the specimen is homogenous and isotropic. Two parallel metal plates with a sponge saturated by conductive gel are fixed at the ends of the specimen. The schematic demonstration of the two-electrode method is shown in Figure 6.6. the geometric factor  $k$  is:

$$k = \frac{A}{L} \quad (6.4)$$

where,

$A$ : cross-sectional area

$L$ : the sample length.

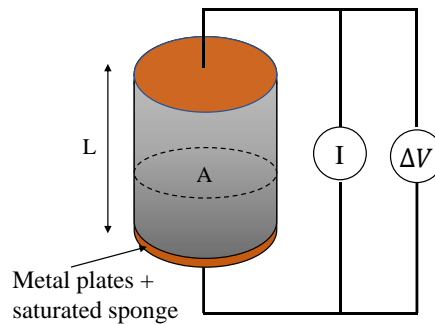


Figure 6.6 Schematic configuration of two-point measurement

## SOUNDNESS ASSESSMENT FOR RC STRUCTURES

The four-point method is a non-destructive measurement that could conduct on the concrete surface with four electrodes (stainless steel probe), as shown in Figure 6.7. Two internal electrodes inject a current, and two external electrodes measure the resulting potential difference, with the same spacing  $a$  (m). The geometric factor is:

$$k = \frac{2\pi}{\frac{1}{a} - \frac{1}{2a} - \frac{1}{2a} + \frac{1}{a}} = 2\pi a \quad (6.5)$$

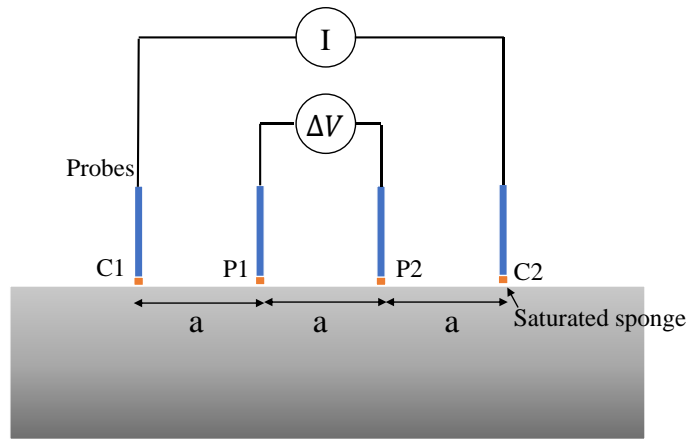


Figure 6.7 Schematic configuration of four-point measurement

However, the presence of rebar affects the measurement of resistivity in a distortion of the current field, or a short-circuit are likely to occur[125][126]. Therefore, the resistivity measurement experiment should be conducted as far as possible from the reinforcement to obtain an accurate value[124].

### 7. Prediction of corrosion rate

After obtaining the water content ( $w$ ), the initial electrical resistivity ( $R_0$ ) could be estimated according to Eq. (3.17). On the other hand, the electrical resistivity could also be electrochemically measured by two-point measurement or four-point measurement. At the same time, the apparent activation energy ( $E_{app}$ ) can be calculated from water content by Eq.(3.18). From the calculated values of  $R_0$  and  $E_{app}$ , the electrical resistivity ( $R$ ) at any given environmental conditions can be estimated according to the

## SOUNDNESS ASSESSMENT FOR RC STRUCTURES

linear relationship between the reciprocal of temperature ( $1/K$ ) and the logarithm of resistivity ( $\log R$ ) with the slope of  $E_{app}$ . Finally, the corrosion rate corresponding to resistivity can be calculated from the linear fitting equation of  $\log R$  and  $\log i_{corr}$ . In addition, the cover thickness can be considered in the prediction process to obtain safe and conservative results, followed by Eq. (4.1) and (4.2). The detailed processes have been presented in Figure 6.2.

### 8. Calculate the corrosion amount during the elapsed years

The accumulated corrosion amount in the concrete members per year can be predicted by integrating the current density over the age as follows:

$$Q_{corr,y} = \int_0^{year} i_{corr} \quad (6.6)$$

When the cracking of the concrete cover layer is initiated, the limit corrosion amount ( $Q_{cr}$ ) can be obtained [30] by combining the results of the experiment of applying the oil pressure to a hollow concrete cylinder until cracking occurs (mechano-physical model) and the experiment of applying the current to steel rebar embedded in concrete until the cracking occurs (accelerated corrosion), and can be expressed as:

$$Q_{cr} = 0.602(1 + 2D/d)^{0.85} \times d \quad (6.7)$$

where,

$Q_{cr}$ : corrosion products amount when concrete cracks ( $10^{-4} \text{ g/cm}^2$ )

$D$ : cover thickness (mm)

$d$ : diameter of steel rebar (mm)

### 9. Predict the residual service life

## SOUNDNESS ASSESSMENT FOR RC STRUCTURES

Figure 6.8 shows a conceptual diagram of the service life of RC buildings affected by carbonation. After the duration that the carbonation front reaches the specific percent ( $P_0$ ) of the surface area of the steel rebar, the corrosion amount is accumulated until the end of the service life that the limit corrosion amount reaches.

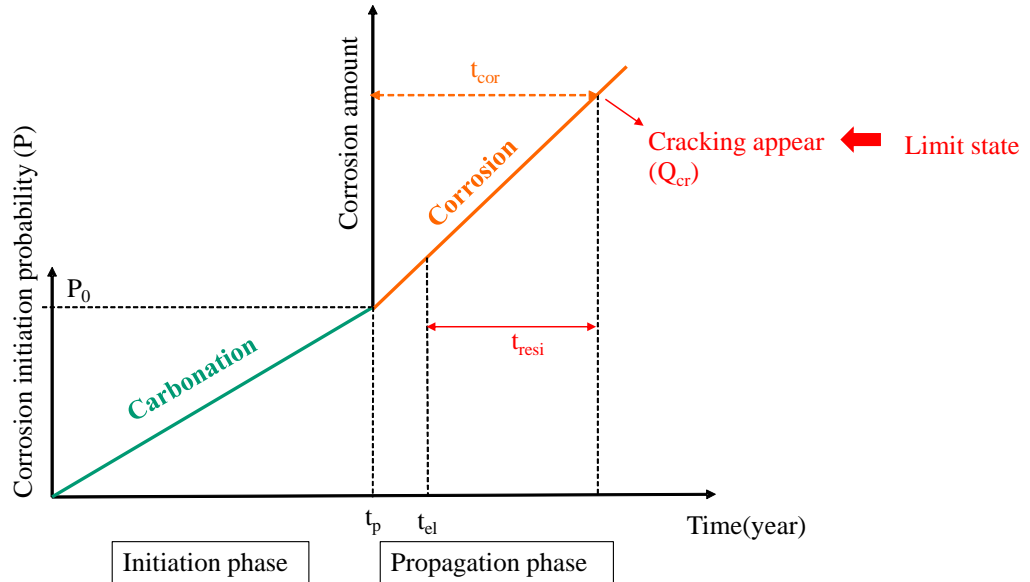


Figure 6.8 A conceptual diagram of service life of RC buildings from carbonation progress

The residual service life ( $t_{resi}$ ) can be expressed by:

$$t_{resi} = (Q_{cr}/Q_{corr,y}) + t_p - t_{el} = t_{cor} + t_p - t_{el} \quad (6.8)$$

where  $t_p$  is the duration for the corrosion initiation probability ( $P$ ) to reach the limit value ( $P_0$ ), and  $t_{el}$  is the elapsed years for the RC structures.

At the end of the residual service life,  $P_0$  of the surface area of steel rebars or  $P_0$  of the total amount of steel rebars will lead to the cracking occurring in the cover layer, and the countermeasures and repairment should be conducted to the concrete members. With the predicted residual service life of concrete members, the performance and maintenance planning of existing RC structures can be determined

In summary, the detailed assessment process is shown in Figure 6.9.

## SOUNDNESS ASSESSMENT FOR RC STRUCTURES

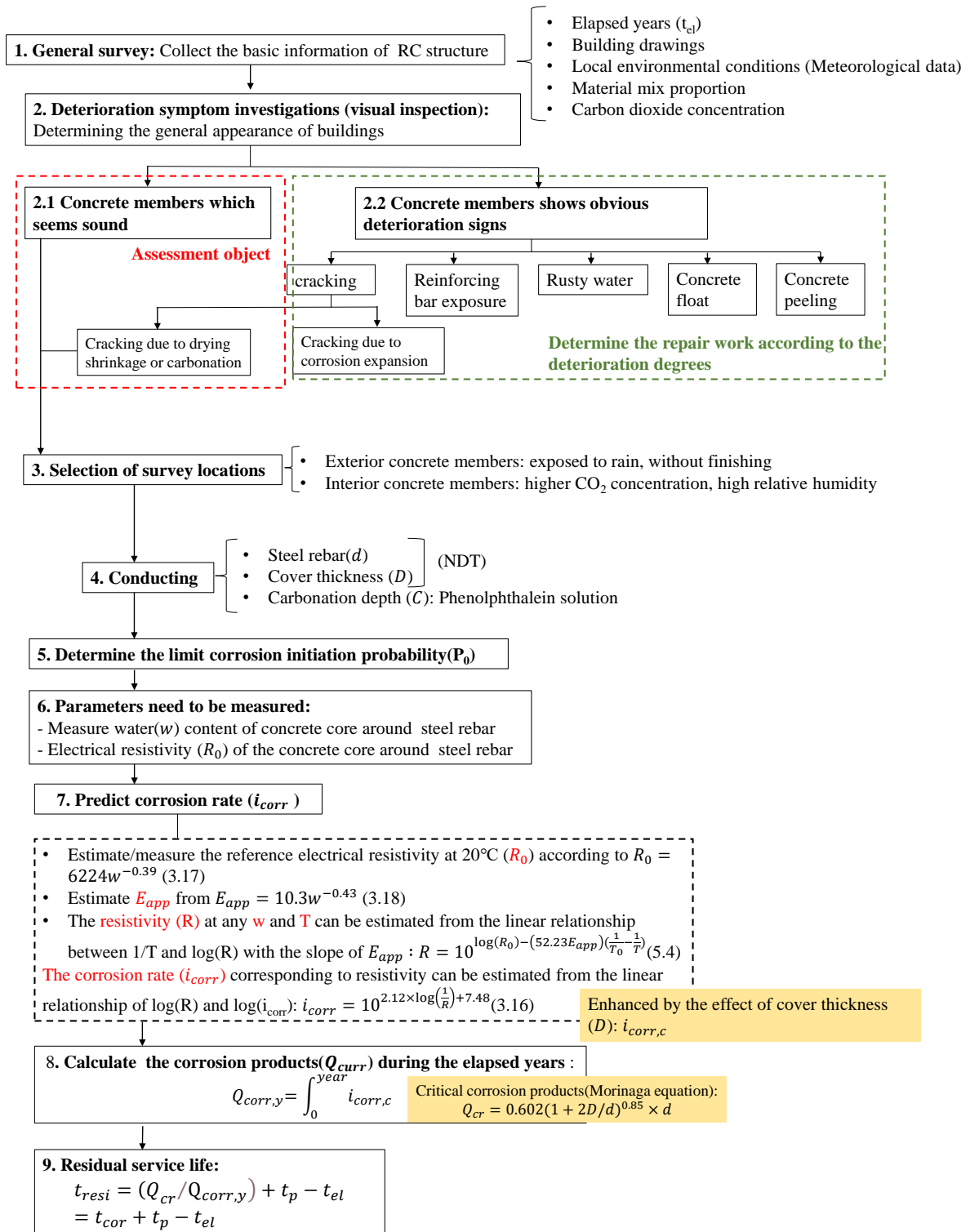


Figure 6.9 Summary of soundness assessment process



## SOUNDNESS ASSESSMENT FOR RC STRUCTURES

### 6.4 An example of residual service life of RC structure.

This section provides an example of the service life prediction for a real RC structure followed the soundness assessment steps described above to illustrate the feasibility of this proposal. An imaginary RC structure is used as the example whose information below is determined based on the investigation data of the real RC structures in Tokyo. And all information can be obtained in the field.

#### 1. General survey

Building name: Elementary school

Location: Bunkyo-ku, Tokyo

Elapsed age: 30 years

Scale: one floor underground and six floors above ground

Structure: RC concrete

Environmental condition: inland

The exposed external temperatures of RC structure per year are investigated and shown in Figure 6.10. And the temperature interior was assumed to be 20°C for simplicity. The investigation of the monthly rainy days in Tokyo is shown in Figure 6.11, and the annual number of rainy days is 117 days.

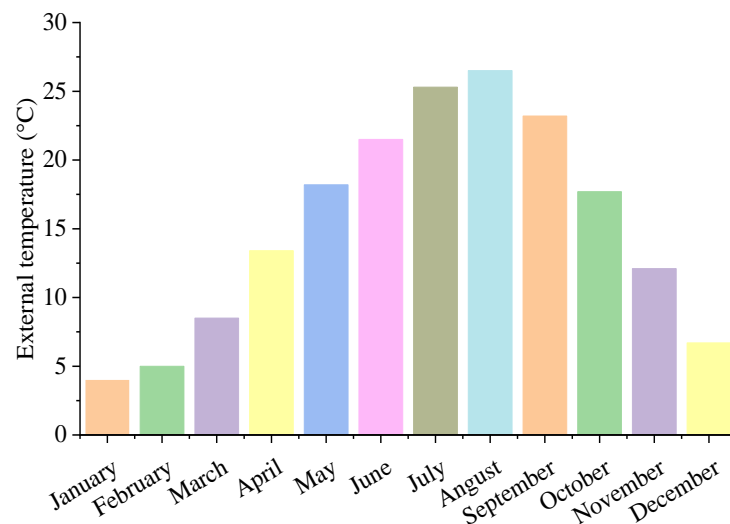


Figure 6.10 Average temperature every month in Tokyo per year

## SOUNDNESS ASSESSMENT FOR RC STRUCTURES

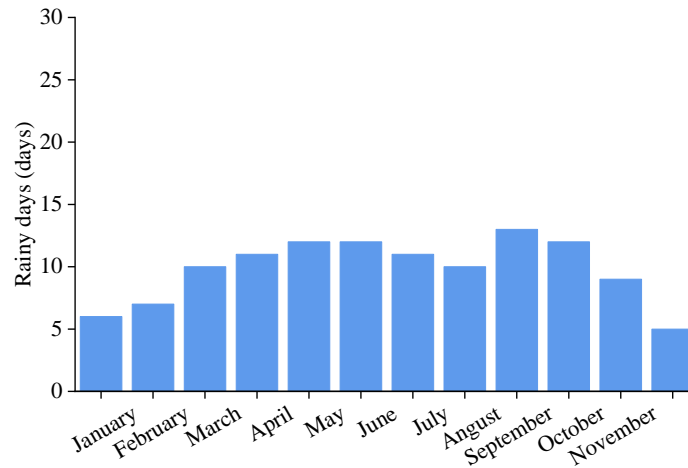


Figure 6.11 Average rainy days in Tokyo

### 2. Deterioration symptom survey

The investigation of deterioration appearance should be conducted for interior and exterior concrete members visually or with simple instruments such as binoculars, test hammers, etc., to make sure the potential assessment objects do not have apparent deterioration appearances on the surface. Exterior concrete members focus on the areas exposed to rain or without finishing, while interior concrete members should consider the CO<sub>2</sub> concentration for each room, especially the spaces where people often gather, such as classrooms and offices. The assessment objects focus on those exposed to high relative humidity or CO<sub>2</sub> concentration environmental conditions. It should be mentioned that the concrete members with the cracks caused by carbonation or drying shrinkage, especially for the interior, should be included in the assessment objects.

### 3. Selection of survey areas of concrete

Since the season with high precipitation in Tokyo is summer, and the prevailing wind direction is southeast monsoon, the investigation exterior will focus on the concrete members located in the southeast of the building, which will be more frequently exposed to rainwater. The investigation results of the finishing condition for the exterior concrete members are summarized in Table 6.4, and three concrete members without finishing are selected as the assessment objects.

## SOUNDNESS ASSESSMENT FOR RC STRUCTURES

Table 6.4 Finishing conditions for the exterior concrete members

Concrete members	Location	Finishing	Selection
Column-1	South	Tile	×
Column-2	South	Artificial Stone	×
Column-3	East	Paint	×
Column-4	East	No finishing	○
Beam-1	South	Tile	×
Beam-2	South	No finishing	○
Beam-3	East	Tile	×
Beam-4	East	Tile	×
Wall-1	South	Plaster	×
Wall-2	South	Tile	×
Wall-3	East	No finishing	○
Wall-4	East	Tile	×

For the investigation of the maximum CO<sub>2</sub> concentration for interior spaces, the results are summarized in Table 6.5, and the concrete members (beam, wall, and floor slab) with the highest CO<sub>2</sub> concentration are selected to be the assessment objects.

Table 6.5 Maximum CO<sub>2</sub> concentration results in interior rooms

Room	CO <sub>2</sub> concentration (ppm)	Selection
Classroom	1200	○
Staff Room	860	×
Office	1100	×
Computer room	800	×
Gymnasium	750	×
Storage	500	×

Twenty areas of columns, beams, and walls with sound surfaces (including cracks caused by carbonization or drying) are selected as interior concrete members. Ten areas of beams, walls and floor slabs with sound surfaces are selected as exterior concrete members. Then the cover thickness distribution and carbonation depth distribution of each concrete member should be measured.

### 4. Investigating results

The investigation results of the cover thickness and carbonation depths are shown in Table 6.6.

## SOUNDNESS ASSESSMENT FOR RC STRUCTURES

Table 6.6 Investigating results of cover thickness and carbonation depth

Location	Concrete members	Cover thickness (cm)	Carbonation depths (cm)
Exterior	Column	4.4 3.0 6.0 3.5 1.9	2.5 1.5 2.9 3.0 1.8
		3.1 4.2 2.7 4.1 2.8	2.4 2.7 1.7 2.6 2.6
		4.3 2.3 3.3 4.0 2.7	2.4 2.0 2.7 2.3 1.8
		4.1 4.7 2.4 3.4 2.9	2.3 3.1 2.8 2.4 2.2
	Beam	4.3 3.2 4.2 4.1 2.9	3.2 1.8 2.7 3.1 2.4
		3.6 4.5 2.3 4.5 3.0	2.9 2.4 2.6 1.6 3.2
		4.4 3.7 5.3 2.4 3.6	2.2 2.7 2.0 2.5 1.4
		4.0 2.6 3.8 4.0 5.2	1.9 3.8 2.6 3.4 2.8
	Wall	5.1 2.5 4.5 1.7 2.9	2.5 2.0 2.2 2.2 2.0
		4.0 1.9 3.5 3.0 5.5	1.6 3.5 2.5 2.6 2.7
		2.7 4.3 1.5 3.4 2.1	3.1 3.0 1.9 1.8 2.4
		3.2 2.4 2.0 4.8 3.8	2.3 2.8 2.0 2.7 2.4
Interior	Beam	3.5 2.2 1.6 2.7 3.0	1.4 0.9 1.3 1.0 1.8
		1.5 2.3 4.3 3.9 4.8	1.1 1.2 1.1 0.9 1.5
	Wall	3.9 1.2 3.1 1.9 3.4	1.7 1.2 1.0 0.9 1.4
		1.7 2.5 2.3 4.3 2.1	1.3 0.9 1.4 1.1 0.7
	Floor slab	3.5 2.5 4.2 2.3 3.3	3.3 3.1 2.1 1.6 2.2
		2.8 3.7 1.9 3.9 3.1	2.9 4.9 2.6 2.6 3.4

Investigation objects are the most outer steel rebars

The average value ( $\bar{c}$ ) and variation coefficient ( $v$ ) of carbonation depth ( $C$ ), and average value ( $\bar{D}$ ) and standard deviation ( $\sigma$ ) of the cover thickness ( $D$ ) can be calculated according to the raw data and shown in Table 6.7.

Table 6.7 Calculated parameters of cover thickness and carbonation depth of exterior and interior concrete members

Location	Concrete members	Cover thickness (cm)	Carbonation depths (cm)
Exterior	Column	$\bar{D} = 3.5$	$\bar{C}_t = 2.4$
		$\sigma = 0.96$	$v = 0.18$
	Beam	$\bar{D} = 3.8$	$\bar{C}_t = 2.6$
		$\sigma = 0.83$	$v = 0.24$
	Wall	$\bar{D} = 3.2$	$\bar{C}_t = 2.6$
		$\sigma = 1.2$	$v = 0.25$

## SOUNDNESS ASSESSMENT FOR RC STRUCTURES

Interior	Beam	$\bar{D} = 3.0$ $\sigma = 1.07$	$\bar{C}_t = 1.22$ $v = 0.22$
	Wall	$\bar{D} = 2.6$ $\sigma = 0.95$	$\bar{C}_t = 1.2$ $v = 0.24$
	Floor slab	$\bar{D} = 3.1$ $\sigma = 0.7$	$\bar{C}_t = 3.3$ $v = 0.30$

### 5. Calculate the corrosion initiation probability of each concrete member

The corrosion initiation probability (P) evolution with time can be expressed by the probability distribution of carbonation depth with time and cover thickness:

$$P = \int_{-\infty}^0 f \frac{1}{\sqrt{2\pi(\bar{C}_t^2 v^2 + \sigma^2)}} \cdot \exp \left[ \frac{-\{(D - C_t) - (\bar{D} - \bar{C}_t)\}^2}{2(\bar{C}_t^2 v^2 + \sigma^2)} \right] d(D - C_t) \quad (6.9)$$

According to Table 6.3, the limited value of corrosion initiation probability ( $P_0$ ) should be set as 15% if the importance of the RC structures in elementary school is high. The calculated corrosion initiation probability values (P) evolution of each concrete member is shown in Figure 6.12, and the duration ( $t_p$ ) when the corrosion initiation probability reached to the limited value can be summarized in Table 6.8.

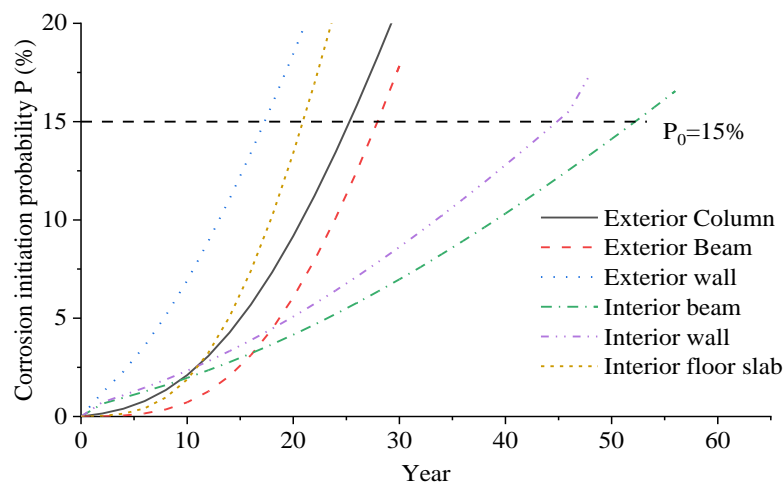


Figure 6.12 Corrosion initiation probability evolution with time for each concrete member

## SOUNDNESS ASSESSMENT FOR RC STRUCTURES

Table 6.8 The duration of the corrosion initiation probability reached to limit value ( $t_p$ ) for each concrete member

Location	Concrete members	$t_p$ (year)
Exterior	Column	26
	Beam	28
	Wall	18
Interior	Beam	54
	Wall	46
	Floor slab	22

### 6. Parameters need to be measured

The water content of concrete fragment near the steel rebar of each concrete member under 20°C are measured and summarized in Table 6.9:

Table 6.9 Water content of concrete near the steel rebar

Location	Concrete members	Water content of concrete (%)
Exterior	Column	3.1
	Beam	2.4
	Wall	2.1
Interior	Beam	2.0
	Wall	1.6
	Floor slab	1.4

Since the water content of mortar is used as the initial parameter in the proposed prediction method, the measured water content of concrete ( $w_c$ ) should be converted to the water content of mortar ( $w_m$ ) following the bulk volume(=0.64) and actual volume fraction (=67.5%) as shown in

Table 6.10[96] with the corresponding coarse aggregate properties, and calculated as below:

$$w_m = \frac{w_c}{1 - (0.64 \times 67.5\%)} = 1.76w_c \quad (6.10)$$

## SOUNDNESS ASSESSMENT FOR RC STRUCTURES

Table 6.10 Standard values of unit coarse aggregate bulk volume for sand and gravel concrete for OPC

w/c (%)	Slump	25			20		
		3.3 (5 mm)	2.8 (2.5 mm)	2.2 (1.2 mm)	3.3 (5 mm)	2.8 (2.5 mm)	2.2 (1.2 mm)
40-60	Below 8-15	0.64	0.69	0.74	0.62	0.67	0.72
	18	0.59	0.64	0.69	0.58	0.63	0.68
65	Below 8-15	0.63	0.68	0.73	0.61	0.66	0.71
	18	0.58	0.63	0.68	0.57	0.62	0.67

The converted water content of mortar for each concrete member is shown in Table 6.11.

Table 6.11 Water content of mortar near the steel rebar

Location	Concrete members	Water content of mortar (%)
Exterior	Column	5.0
	Beam	5.5
	Wall	5.9
Interior	Beam	6.0
	Wall	6.6
	Floor slab	7.0

The initial electrical resistivity values and the apparent activation energy values of each concrete member can be calculated based on the water content according to Eq.(3.17) and (3.18) as follow:

Table 6.12 Initial electrical resistivity ( $R_0$ ) of each concrete member

Location	Concrete members	Water content (%)	$R_0$ ( $\Omega\text{cm}$ )	$E_{app}$ (kJ/mol)
Exterior	Column	5.0	3211.4	4.97
	Beam	5.5	3548.4	5.54
	Wall	5.9	3738.1	5.87
Interior	Beam	6.0	3809.9	6.00
	Wall	6.6	4156.4	6.60
	Floor slab	7.0	4378.5	6.99

## SOUNDNESS ASSESSMENT FOR RC STRUCTURES

In this case, the electrical resistivity of concrete under different temperature conditions per month can be calculated, followed by Eq. (5.4), and summarized as shown in Figure 6.13.

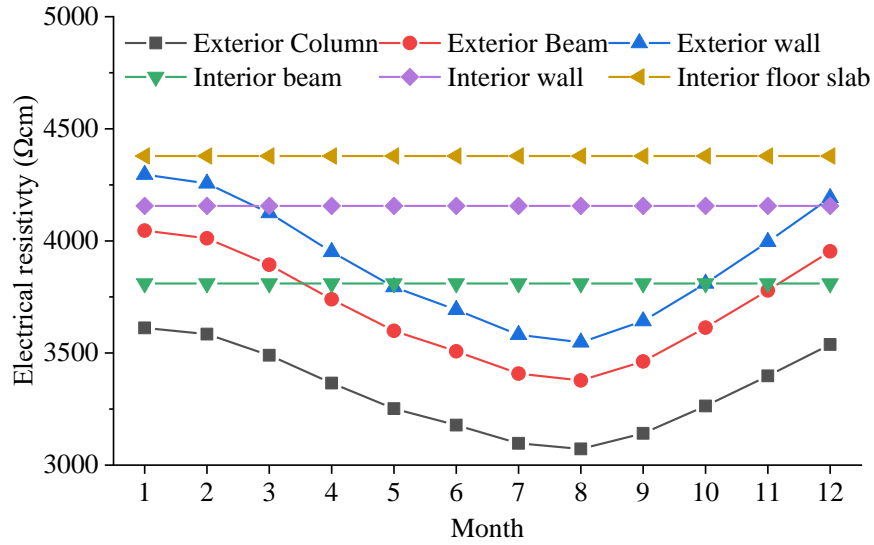


Figure 6.13 Predicted electrical resistivity of concrete members every month

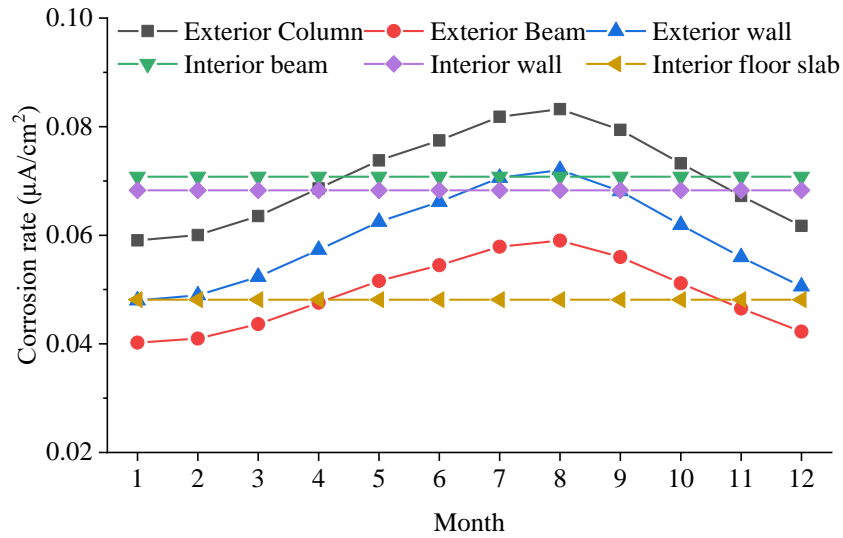


Figure 6.14 Predicted corrosion rate of steel rebar of concrete members every month at the first year



## SOUNDNESS ASSESSMENT FOR RC STRUCTURES

At the same time, the corrosion rate of steel embedded in each concrete member with different cover thicknesses can be predicted based on the electrical resistivity values according to Eqs. (3.16), (4.1), and (4.2), as shown in Figure 6.14. However, the corrosion rate of steel rebar decreases with age and becomes stable within 150 days because the formed corrosion products around steel rebar will inhibit the electrons exchange and decreases the corrosion rate. According to [127], the initial corrosion rate is about three times higher than the stable corrosion rate. Therefore, the stable corrosion rate for each concrete member is assumed to occur from the second year from the corrosion initiation time, as shown in Figure 6.15.

It should be mentioned that rainfall days every month was investigated, as Figure 6.11 shown. Therefore, the corrosion rate of steel rebar in the concrete member during the rainfall should be considered. According to the electrochemical results of the carbonated reinforced mortar sample spayed by water for 24 hours from the author's Master thesis[128], the corrosion rate of steel rebar during the rainy days for each concrete member can be calculated. The details can be found in Appendix D.

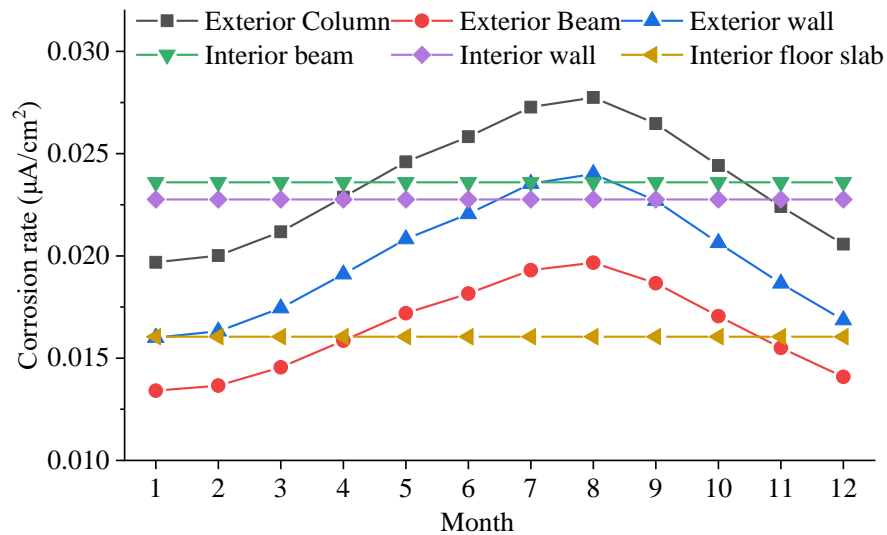


Figure 6.15 Predicted corrosion rate of steel rebar of concrete members every month at the second year

The unit of corrosion current density ( $\mu\text{A}/\text{cm}^2$ ) can be converted to the unit of corrosion amount ( $\text{mg}/\text{cm}^2/\text{day}$ ) by applying Faraday's law:

## SOUNDNESS ASSESSMENT FOR RC STRUCTURES

$$1\mu A/cm^2 = 0.0249mg/cm^2/day \quad (6.11)$$

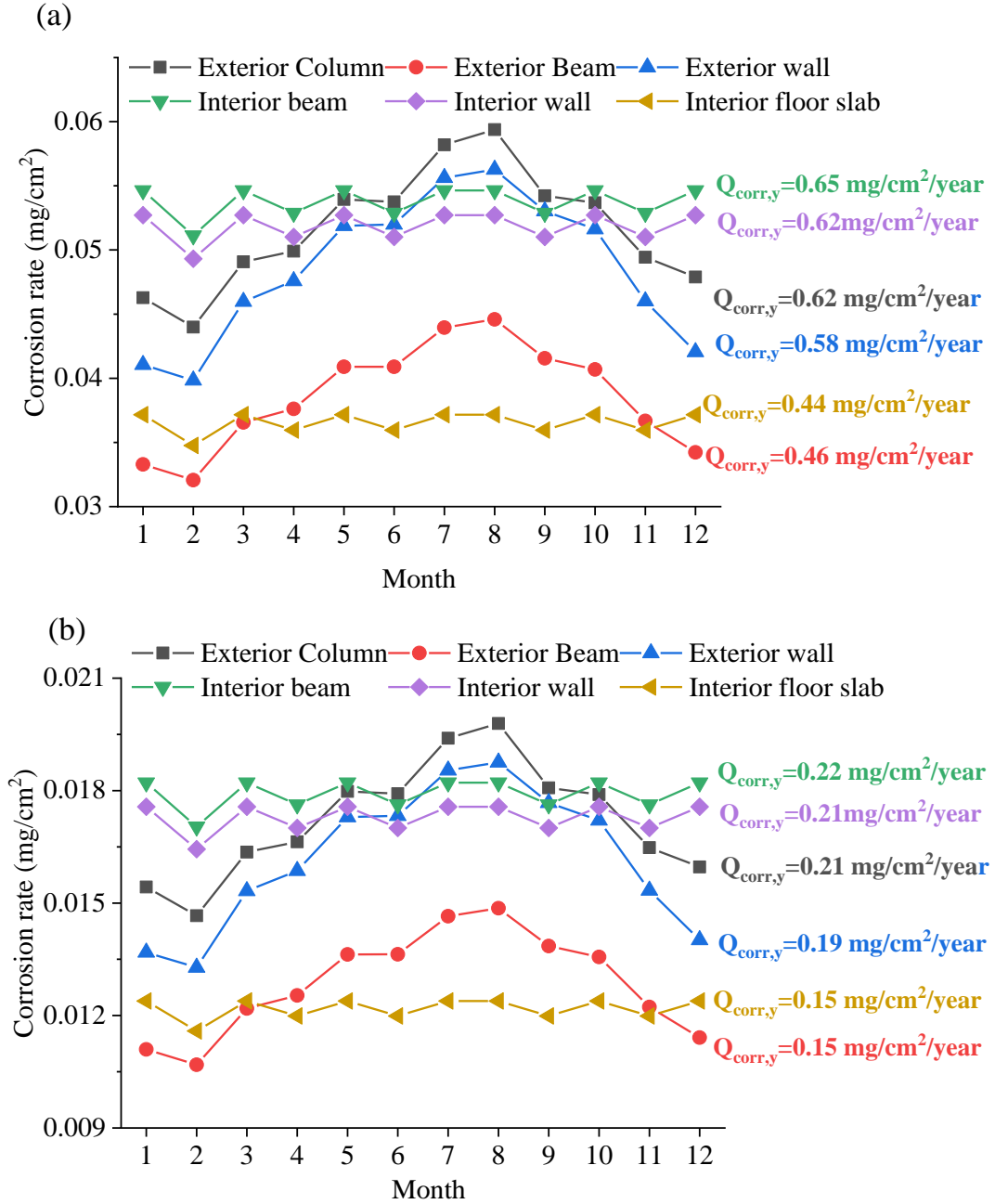


Figure 6.16 Predicted corrosion amount of steel rebar of concrete members every month at the first year (a) and second year (b)

Then, the corrosion amount of each concrete member every month in the first year and the second year can be calculated in Figure 6.16 (a) and (b) shown. The total corrosion

## SOUNDNESS ASSESSMENT FOR RC STRUCTURES

amount of steel rebar per year ( $Q_{corr,y}$ ) for each concrete member are listed below each curve.

The limit corrosion amount ( $Q_{cr}$ ) can be obtained from Eq. (6.7) based on the general information of cover thicknesses and steel rebar diameters of each concrete member. These parameters and calculated results of  $Q_{cr}$  are listed in Table 6.13.

Table 6.13 The limited corrosion amount of each concrete member

Location	Concrete members	Cover thickness (mm)	Steel rebar diameter (mm)	Limited corrosion amount $Q_{cr}$ (mg/cm <sup>2</sup> )
Exterior	Column	$\bar{D} = 36$	$d = 15$	4.02
	Beam	$\bar{D} = 40$	$d = 12$	4.08
	Wall	$\bar{D} = 32$	$d = 12$	3.47
Interior	Beam	$\bar{D} = 29$	$d = 12$	3.23
	Wall	$\bar{D} = 26$	$d = 10$	2.84
	Floor slab	$\bar{D} = 31$	$d = 10$	3.22

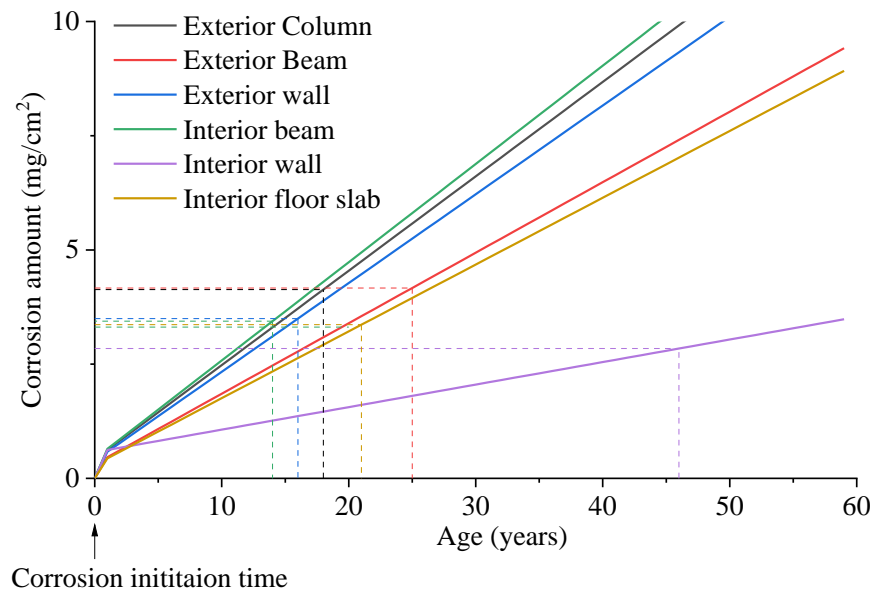


Figure 6.17 Corrosion amount evolution with age of every concrete member

Based on the predicted total corrosion amount per year and the limited corrosion amount of each concrete, the corrosion amount evolutions can be presented from the

## SOUNDNESS ASSESSMENT FOR RC STRUCTURES

time that corrosion initiation probability reached the limit value in Figure 6.17. The horizontal dashed line represents the limit corrosion amount for each concrete member; the vertical dashed line represents the age when corrosion-induced cracking occurred on the concrete members (service life).

The corrosion amount and corrosion year ( $t_{cor}$ ) of every concrete member at the end of service life when corrosion-induced cracking occurs in concrete members are shown in Table 6.14.

Table 6.14 Corrosion amount evolution at the service life of every concrete member

Location	Concrete members	$t_{cor}$ (year)	Corrosion amount (mg/cm <sup>2</sup> )
Exterior	Column	16	3.72
		17	3.92
		18	4.13
		19	4.34
		20	4.54
		23	3.86
	Beam	24	4.01
		25	4.17
		26	4.32
		27	4.48
		14	3.11
	Wall	15	3.30
		16	3.50
		17	3.69
		18	3.89
Interior	Beam	12	3.01
		13	3.23
		14	3.44
		15	3.66
		16	3.87
	Wall	44	2.74
		45	2.79
		46	2.84
		47	2.89
		48	2.94
	Floor slab	19	3.07
		20	3.22
		21	3.36
		22	3.51
		23	3.66

## SOUNDNESS ASSESSMENT FOR RC STRUCTURES

Based on the calculated  $t_p$  and  $t_{cor}$  for each concrete member, the predicted service life (when corrosion-induced cracking occurs) ( $t_{resi}$ ) for the concrete members can be calculated and shown in Table 6.15. 15% of the surface area of the steel rebar or 15% of the total amount of steel rebar will lead to the cracking of the concrete layer occurring at the end of the service life.

Table 6.15 Residual service life of every concrete member

Location	Concrete members	$t_{el}$ (year)	$t_{cor}$ (year)	$t_p$ (year)	$t_{resi}$ (year)
Exterior	Column	30	18	26	14
	Beam		25	28	23
	Wall		16	18	4
	Beam		14	54	38
Interior	Wall	30	46	46	62
	Floor slab		21	22	13

### 6.5 Summary

The process of the soundness assessment method for RC structures is introduced and applied to an imaginary RC structure to illustrate the feasibility of this proposal. For the carbonation-induced corrosion deterioration in RC structures, the carbonation front progress through the cover thickness (initiation period) is considered by the corrosion initiation probability ( $P$ ), and the comprehensive effect of RH and temperate on corrosion behavior (propagation period) are taken into account as well. The corrosion rate prediction method is established based on the corrosion controlling mechanism under different environmental conditions, enhanced by the different cover thicknesses to expand the application filed in practice, and verified by the reinforced supplementary cementitious materials. For the application in the field, the necessary input parameters for corrosion rate prediction are readily available: water content, carbonation depth, and cover thickness. The feasibility, accuracy, operability, and safety of this proposal allow it to be used to predict the service life of concrete members and contribute to the enhancement of the durability of RC structures.

### 7. CONCLUSIONS AND RECOMMENDATIONS FOR FUTURE WORK

#### 7.1 Overview of contributions and conclusions

This study aims to propose a soundness assessment method of RC structures affected by carbonation.

Firstly (in **Chapter 3**), the dependence of RH and temperature on carbonation-induced corrosion behavior and the corresponding corrosion controlling mechanisms were clarified by electrochemical experiments on the carbonated reinforced mortar under various environmental conditions and microstructure characterization analysis of carbonated mortar:

- 1) The decreasing trend of the electrical resistivity of carbonated mortar and the increasing trend of the corrosion rate of steel occurred with increasing temperature and RH conditions because of the mobile ions in the pores and the increased condensed electrolyte. The temperature dependence of electrical resistivity decreased with increasing water content in the mortar. The temperature peak value for the increase in corrosion rate was 40 °C under high RH conditions, caused by the decreased dissolved oxygen content.
- 2) The corrosion control mechanisms were verified by the correlation between the corrosion potential and corrosion rate of the steel rebar, and the correlation between electrical resistivity of the mortar and the corrosion rate. The linear relationship between the reciprocal of electrical resistivity and carbonation-induced corrosion rate, and the increase of the corrosion rate with the corrosion potential shifting more negatively indicate that the corrosion process in carbonated mortar is under resistive control in most cases.
- 3) The regression analysis model of the electrical resistivity of cement materials and the linear correlation between the reciprocal of the electrical resistivity of the mortar and the corrosion rate of the steel rebar enable an engineering application to estimate the corrosion rate of steel rebars under different exposure conditions when the

## CONCLUSIONS AND RECOMMENDATIONS FOR FUTURE WORK

corrosion process is under resistive control within specific exposed conditions (under 68% to 84%RH with temperatures ranging from 20°C to 50°C, and 91% to 97% RH with temperatures ranging from 20°C to 40°C)

In practical cases, the cover thickness is thicker than the cover thickness of 5 mm used in the experiment. Therefore, a more precise and empirical corrosion rate prediction method was proposed considering the effect of cover thickness based on the proposed equation proposed in Chapter 3 (in **Chapter 4**):

- 1) The increase of cover thickness inhibits the corrosion rate of steel rebar due to the increase of effective diffusion layer for oxygen and water content, causing the lack of oxygen and water content for corrosion reaction. When the cover thickness increases, the effect of RH and temperature on corrosion rate decreases due to the water content and oxygen penetration in mortar would remain at a depth ranging from 30 to 40 mm.
- 2) A more precise and safe corrosion rate prediction equation considering the effect of cover thicknesses was proposed based on the reference value of corrosion rate obtained in Chapter 3.

The proposed corrosion rate prediction method was verified by the electrochemical results of the carbonated slag-based mortar with four different replacement ratios of BFS (30%, 50%, 60%, and 70%) in **Chapter 5**, exposing to different RH and temperature conditions: The relationship between the measured corrosion rate and calculated corrosion rate values in reinforced slag-based mortar shows that the estimation based on the prediction method proposed in Chapter 3 is a reliable and safe method for evaluation of corrosion behaviors in carbonated cementitious materials.

Finally, a soundness assessment for RC members has been proposed based on the proposed corrosion rate prediction method discussed in Chapters 3 to 5 in **Chapter 6**, with the references to the related Japanese standard specifications.

### 7.2 Originality

- 1) A miniaturized mortar sample was built, which provided a novel method to minimize the experiment duration, including mortar sample preparation and reaching

## CONCLUSIONS AND RECOMMENDATIONS FOR FUTURE WORK

equilibration at various environmental conditions. All the necessary electrochemical tests were successfully and efficiently carried out to evaluate the corrosion behaviors.

2) The RH and temperature dependence on the corrosion process was clarified, and corrosion controlling mechanisms under different environmental conditions were proposed according to the electrochemical results obtained from miniaturized mortar samples and electrochemical knowledge.

3) A corrosion rate prediction method was proposed according to the obtained corrosion controlling mechanisms under specific environmental conditions.

4) A feasible soundness assessment method for real RC structures was proposed by combining the proposed corrosion rate prediction methods and field investigations.

### 7.3 Recommendations for future work

This study focuses on the soundness assessment of RC structures affected by carbonation based on the laboratory experimental results and electrochemical microstructural analysis. To develop the application of the soundness assessment method, the following aspects are expected to be done in future research:

1) It is necessary to consider the effect of deformed steel rebar on the electrical results, which is usually used in practice. Since crevice corrosion easily occurs due to the existence of ribs, it should develop and take more effort on electrochemical measurement methods with deformed steel rebars in an accurate way.

2) Since the existence of sulfide in reinforced supplementary cementitious materials makes the measured corrosion rate overestimate the real corrosion behavior, the specific oxidation reaction of sulfide species should be studied further to separate the real corrosion rate from the detected corrosion rate. More precise electrochemical measurements for the supplementary cementitious materials are needed, especially for those with higher replacement ratios.

3) It is also necessary to acknowledge that the experimental work involved accelerated carbonation, which may not fully represent natural carbonation. Therefore, the prediction equation of corrosion rate needs to be validated using data from natural carbonation in-service RC members.



## APPENDIX A

### APPENDIX A CARBONATION DEPTH CONFIRMATION AND CARBONATION DEGREES CALCULATED BY X-RAY DIFFRACTION (XRD)/RIETVELD ANALYSIS

The carbonation depth was determined by breaking the specimens diametrically and spraying a 1% phenolphthalein indicator solution onto the broken surface. Figure A.1 shows the phenolphthalein test results of the cross-sections of the non-carbonated and carbonated mortar specimens, which indicates that the mortar had been fully carbonated and sufficient to activate steel corrosion after the accelerated carbonation process.



Figure A.1 Cross-sections ( $20 \times 20 \text{ mm}^2$ ) of reference mortar specimens sprayed with 1% phenolphthalein solution: (a) non-carbonated; (b) carbonated.

To evaluate the carbonation conditions, the part of mortar around the steel rebar was taken and then ground using a ball mill. After grinding, the particle size was checked using a  $75 \mu\text{m}$  sieve. Retained powder, if necessary, was ground manually until all the material passed through the sieve. Retained powder, if necessary, was ground manually until all the material passed through the sieve. The powder was analyzed using a Bruker TG-DTA-2000SA to quantify changes in the amount of calcium hydroxide and calcium carbonate after carbonation. Approximately 20 mg of powder was placed in an alumina crucible. The weight was monitored while the powder was heated from  $25^\circ\text{C}$  to  $1000^\circ\text{C}$  at  $10^\circ\text{C}/\text{min}$  in a nitrogen atmosphere flowing at  $100 \text{ cm}^3/\text{min}$ .

The sample powder was combined with corundum powder (10 mass%) as a standard reference. To identify the phase compositions, powder X-ray diffraction (XRD) was

## APPENDIX A

conducted using a Rigaku Mini Flex diffractometer with Cu K $\alpha$  radiation, using a  $2\theta$  scan range of 5°-70° and a scan speed of 2°/min.

Figure A.2 shows the diffraction patterns for the non-carbonated and carbonated mortar samples. It was found that more portlandite remained in the non-carbonated sample, while calcite and aragonite were mainly formed in the carbonated sample. A Rietveld analysis was conducted to quantify the phase composition related to the carbonation, and the results are summarized in Table A.1. The percentages reported are the ratios of each phase to each gram of cement.

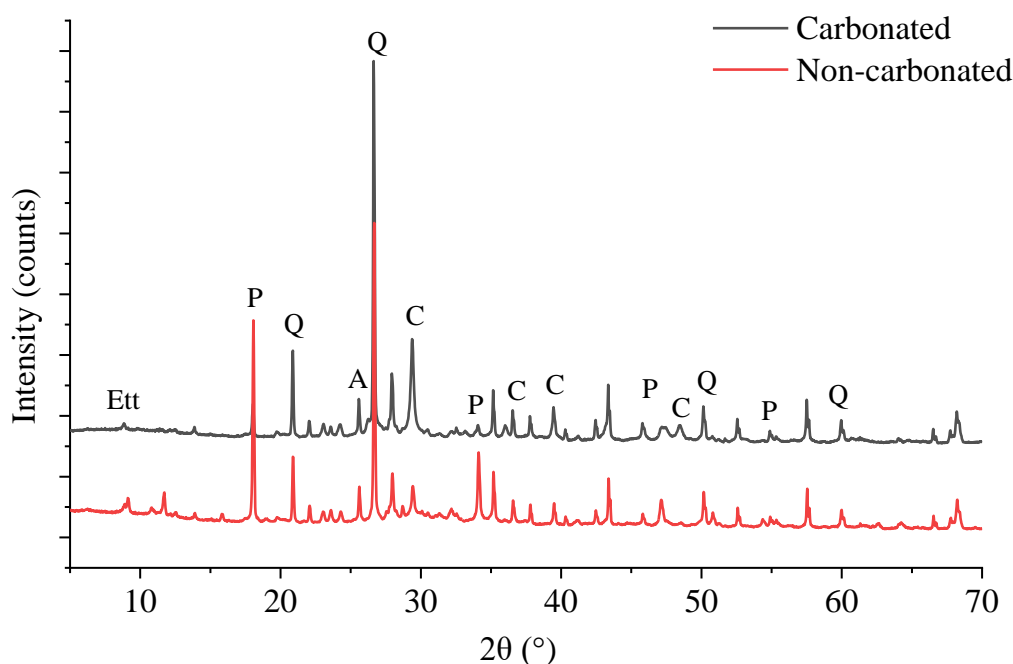


Figure A.2 Diffraction patterns of non-carbonated and carbonated mortar samples (Q: Quartz, C: Calcite, P: Portlandite, Ett: Ettringite, A: Aragonite).

Table A.1 Phase composition determined through XRD/Rietveld analysis of the cement paste (mass%).

	Calcite	Portlandite	Aragonite	Vaterite
Non-carbonated sample	6.80±0.7	18.8±0.1	0.0	0.0

## APPENDIX A

Carbonated sample	31.5±0.5	3.79±0.8	6.64±0.3	0.0
-------------------	----------	----------	----------	-----

Figure A.3 shows the derivative thermogravimetry (DTG) curves for the non-carbonated and carbonated samples, in which the curves are in terms of grams of cement paste rather than grams of mortar for clear comparison. The carbonated sample had a larger calcite content, which can be observed as a peak at 730 °C, while the non-carbonated had a smaller aragonite content, which can be observed as a peak at 580 °C. The non-carbonated samples had a greater portlandite content than the carbonated samples, as seen from the peak at around 430 °C. Furthermore, the greater content of ettringite decomposed at 90 °C in non-carbonated samples.

To evaluate the carbonation conditions, a method for calculating the degree of carbonation  $\alpha_c$  is proposed. The degree of carbonation is defined as the ratio of calcium oxide in calcium carbonate, which is formed during the carbonation process, to the total calcium oxide per gram of cement. Therefore, the degree of carbonation can be expressed as:

$$\alpha_c(\%) = \frac{\frac{R_{cp}}{1-LOI} \times \frac{56}{100} - R_c^0 \times \frac{56}{100}}{R_t} \quad (A.1)$$

where  $R_{cp}$  is the ratio of calcium carbonate (calcite and aragonite) per gram of carbonated cement paste (Table A.1),  $R_c^0$  is the initial ratio of calcium carbonate per gram of cement (Table 3.2),  $LOI$  is the ratio of water loss on ignition, and  $R_t$  is the total ratio of calcium oxide per gram of cement (Table 3.1).

The DTG curve was integrated, and the ratio of phase composition from the XRD analysis was quantified, with the results shown in Table A.2. Thus, from these results, the degree of carbonation can be evaluated.

## APPENDIX A

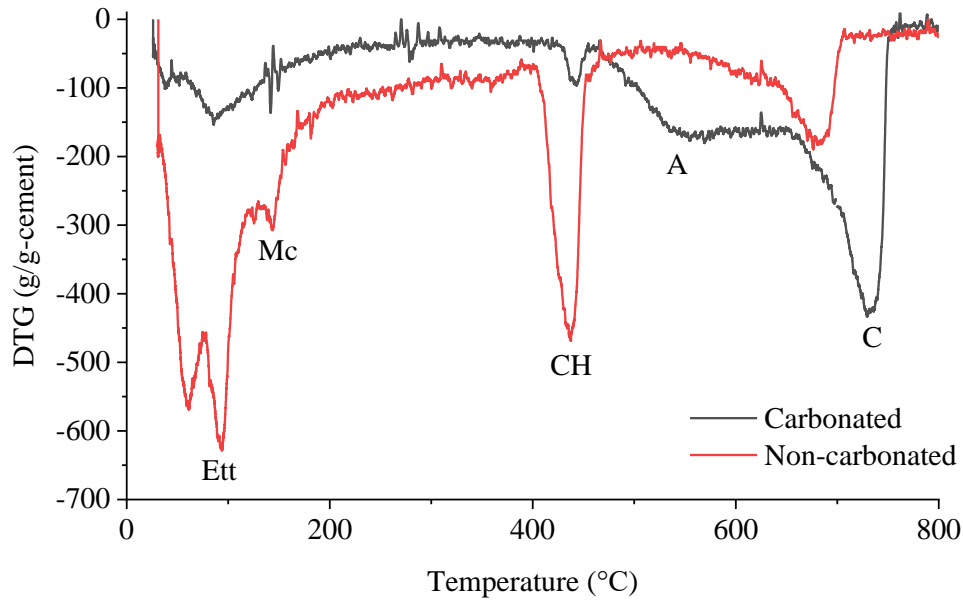


Figure A.3 DTG curves for the non-carbonated and carbonated mortar with the main decompositions labeled (Ett: Ettringite, Mc: Monocarbonate calcium aluminate, CH: Portlandite, A: Aragonite, C: Calcite).

Table A.2 Carbonation degrees calculated from XRD and DTG

	$R_{cp}$		$LOI$	$R_c^0$	$R_t$	$\alpha_c(\%)$
	Calcite	Aragonite				
XRD/Rietveld	31.5±0.5	6.64±0.3	0.248±0.03	3.2±0.1	64.1	41.53.2±0.5
DTG	36.2±0.4					39.33.2±0.2

The analysis clearly shows that the degree of carbonation calculated by the XRD analysis and DTG curves were similar, though the degree of carbonation shown from the XRD analysis is slightly higher. All the data from the DTG curves were consistent with the results of the XRD analysis. From these results, the degree of carbonation was evaluated as approximately 40.43%.

## APPENDIX B

### APPENDIX B SATURATION DEGREE OF CARBONATED MORTAR AT DIFFERENT RH AND TEMPERATURE CONDITIONS

The degree of pore saturation of the mortar was calculated by the following equation:

$$ps = \frac{m_s - m_d}{m_h - m_d} \quad (B.1)$$

where  $m_h$  denotes the weight of saturated mortar at the SSD (water-saturated and surface dry) conditions by immersing it in ionized water inside a desiccator with a low pump pressure. Figure B.1 shows the pore saturation degrees of carbonated mortar and chloride-containing mortar at different RH and Temperature conditions

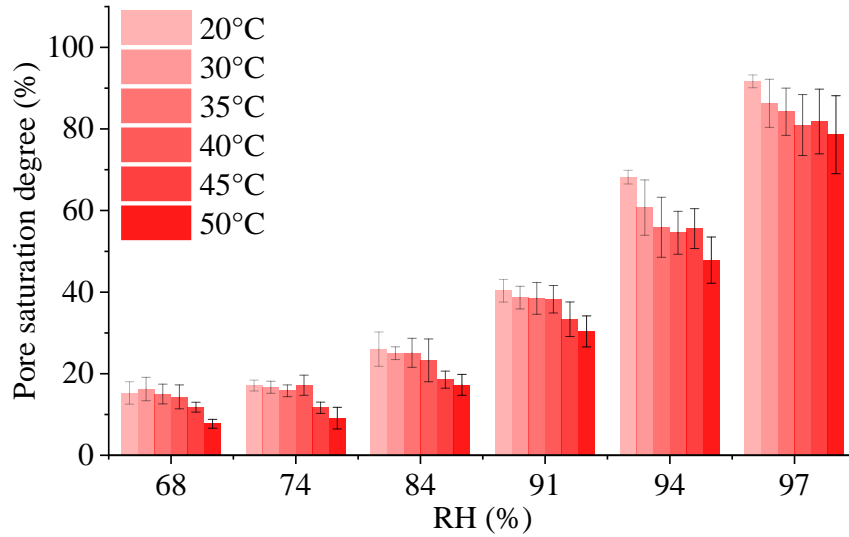


Figure B.1 Pore saturation degrees of carbonated mortar at different RH and temperature conditions

## APPENDIX C

### **APPENDIX C EFFECT OF RH AND TEMPERATURE ON STEEL CORROSION IN CHLORIDE-CONTAINING MORTAR—COMPARISON WITH CARBONATION-INDUCED CORROSION**

#### **C.1 Experimental procedure**

##### **C.1.1 Material and specimen**

Ordinary Portland Cement (OPC) was used in this research. Two sizes of silica sand (UBE INDUSTRIES 5A and 7) with a density of  $2.6 \text{ g/cm}^3$  were used as fine aggregate for all mortar mixes. For the chloride-contained mortar, to reproduce the case that reinforced concrete structures heavily contaminated by chloride, only the chloride ions in the pore solution affect the corrosion of steel rebar; thus, the chloride threshold value can be expressed as a molar concentration ratio of the chloride ion concentration to the hydroxide ion concentration ( $[\text{Cl}^-]/[\text{OH}^-]$ ) in concrete pore solution. As reported in previous related studies, such molar concentration ratios were variable ranged from 0.10 to 5.40[8][9][10][11] due to the different experimental conditions and confirmation methods for corrosion initiation. According to the pH value of OPC mortar (about 13.5) and chloride ions binding isotherms based on hydrated amount[14][129], the total chloride threshold value (the sum of bound and free chloride amount) can be converted to 0.4 to 2.94% by weight of cement (wt% of cement).

On the other hand, the results of investigations of RC structures indicated that the chloride threshold values ranged from 0.2 to 2.2 wt% of cement[130][131][12]. Therefore, considering the difference between the calculated value and the actual measured value, a portion of 2 wt% of cement sodium chloride (NaCl) with 99.9% purity, as a representative value, was used as the source for chloride ions and mixed in water. Polypropylene fibers (length of 6 mm, diameter of 0.028 mm) were used to prevent cracking in the mortar cover caused by corrosion products. The water-to-cement ratio (W/C) of 0.60 and sand-to-cement ratio (S/C) of 2 were held constant throughout the experimental program. The mortar mix proportions as shown in Table C.1.

## APPENDIX C

Table C.1 Mix proportion of chloride-containing mortar

W/C (%)	S/C	Water (kg/m <sup>3</sup> )	Cement (kg/m <sup>3</sup> )	Sand (kg/m <sup>3</sup> )		Fiber (kg/m <sup>3</sup> )	Sodium chloride (2 wt % of cement)
				1.7-0.2 mm	< 0.2 mm		
60	2	320	534	534	534	0.91	12.62

The specimen design (20×20×40 mm) is the same as the mortar samples for accelerated carbonation in Chapter 3 except for the mix proportion.

### C.1.2 Environmental condition control

All the samples were set and hardened in the mold for one day at 20±2°C before being demold, then sealed in a curing room at 20±2°C for 28 days. After 28 days, the samples were placed in sealed boxes with different saturated salt solutions to control the RH of 68%, 75%, 84%, 91%, 94%, and 97%, as shown in Table 3.5 (Chapter 3). Subsequently, the sealed boxes were placed in a temperature-controlled chamber of 20°C, 30°C, 35°C, 40°C, 45°C, and 50°C. The mass of the samples was monitored at regular intervals throughout the exposure period. Once all samples reached mass equilibration during the process, the electrical resistivity of mortar samples was measured. Since different RH conditions for samples require different durations to be stable, it took two weeks to one month.

The water content in chloride-containing mortar under each environmental condition was determined as the same process described in Section 3.2.3 (Chapter 3).

### C.1.3 Electrochemical measurements

The electrical resistivity of the mortar was monitored using an LCR meter (IM3533-HIOKI) over a frequency range of 0.1 Hz to 100 kHz by applying an AC perturbation with an amplitude voltage of 50 mV. Detailed treatment of samples, measurement and calculation processes can be found in Section 3.2.3 (Chapter 3)

## APPENDIX C

### C.1.4 Microstructure of chloride-containing mortar

Mercury intrusion porosimetry tests were conducted to determine the porosity and pore-size distribution of chloride-containing mortar specimens. All samples were initially oven-dried at 80 °C for 24h. Mercury intrusion porosimetry was conducted using an Autopore III 9410 W (Shimadzu) with a peak pressure of 206 MPa. The contact angle and surface tension values used during the measurements were 130° and 0.485 N/m, respectively. Detailed treatment of samples, measurement and calculation processes can be found in Sections 3.2.5 and 3.2.3 (Chapter 3)

## C.2 Experiment Results

### C.2.1 Electrical resistivity of chloride-containing mortar

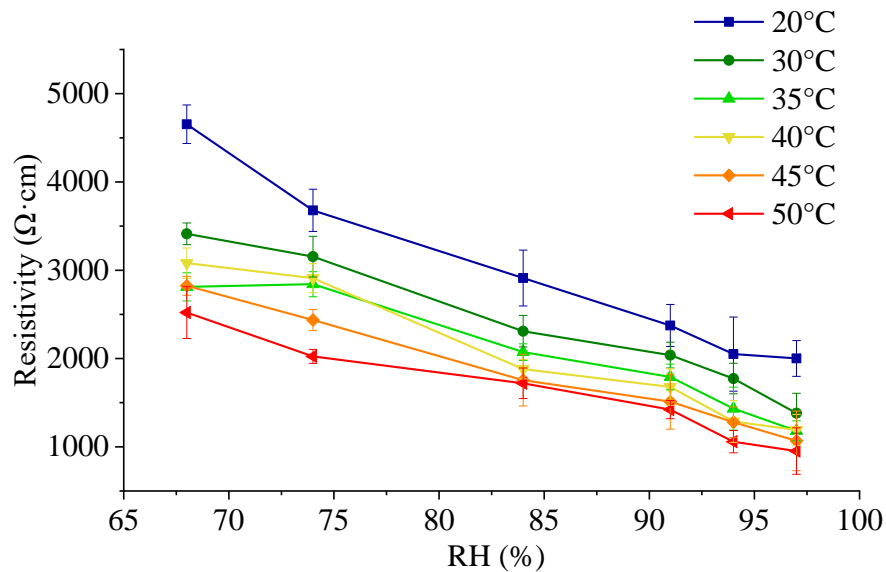


Figure C.1 Electrical resistivity of chloride-containing mortar at different RH and temperature conditions

Figure C.1 shows the electrical resistivity of the chloride-containing mortar under different RH and temperature conditions, in which the data correspond to the average value of two or three replicates. As expected, increases in the relative humidity and temperature were accompanied by decreases in the electrical resistivity of the mortar



## APPENDIX C

specimens. The minimum values of electrical resistivity of  $952 \Omega \cdot \text{cm}$  occurred at the highest RH and temperature conditions (RH=97%, T=50°C), whereas the maximum values of electrical resistivity of  $4654 \Omega \cdot \text{cm}$  were observed at the lowest RH and temperature conditions (RH=68%, T=20 °C). In addition, it should be noticed that the electrical resistivity of the chloride-containing mortar was almost half of that of carbonated mortar (refer to Figure 3.11).

### C.2.2 Microstructure characterization of chloride-containing mortar

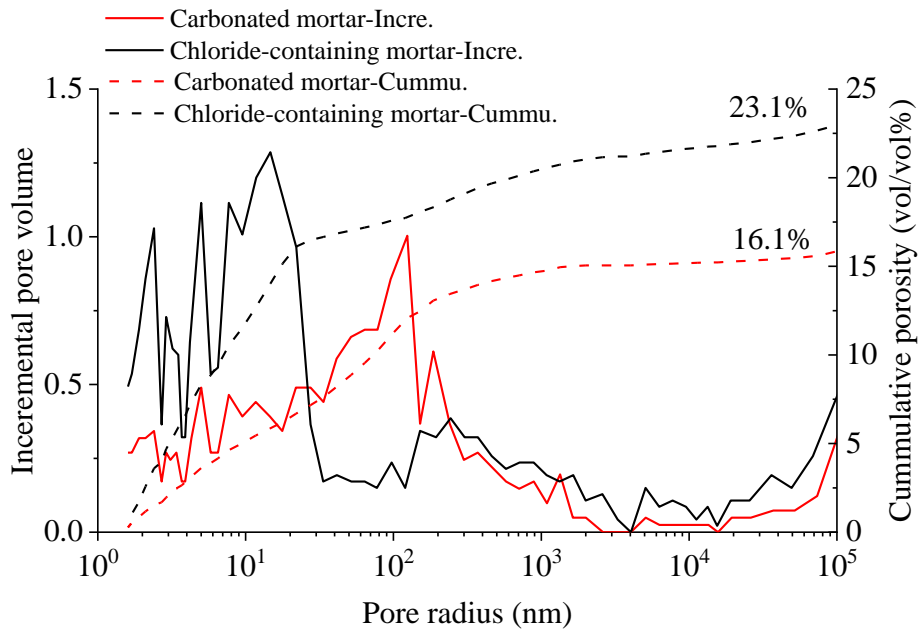


Figure C.2 Pore size distribution and cumulative porosity of chloride-containing mortar and carbonated mortar

Figure C.2 compares the pore size distributions and accumulated pore volumes between chloride-containing mortars and carbonated mortar (data from Figure 3.15). The porosity of the chloride-containing was 23.1%, which is higher than that of the carbonated mortar (16.1%). The volume of the pores ranged from 4-50 nm corresponding to capillary mesopores [69] in carbonated mortar, which is smaller than that in chloride-containing mortar owing to the clogging effect of the pores occupied by the calcium carbonation formed from calcium hydroxide (CH) and calcite-silicate-

## APPENDIX C

hydrate (C-S-H) [70][71]. In addition, carbonation products are also capable of producing larger capillary 50-100 nm pores, which appear between calcium carbonate crystals and the porous structure of silica gel [72][73], increasing the pore volume of the carbonated mortar.

Figure C.3 shows water content changes in the chloride-containing mortar in different RH conditions. As expected, the water content increased with RH due to more liquid water condensed in the pores, while it decreased with temperature because of the increasing water vapor pressure. The water content increased when RH increased, which agrees with the increased capillary pore volume in Figure C.2. Furthermore, the water content under each RH condition in the chloride-containing mortar was higher than in carbonated mortar (refer to Figure 3.17), which is consistent with the higher capillary pore volume in chloride-containing mortar in Figure C.2.

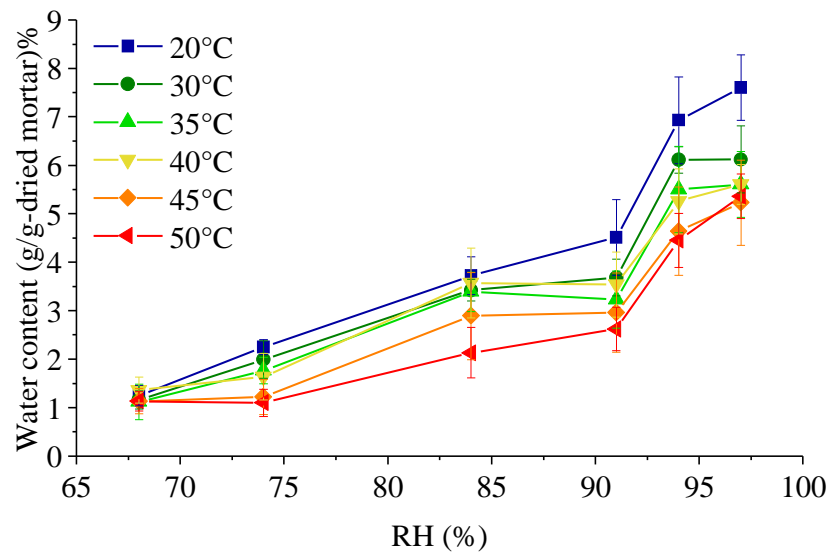


Figure C.3 Water content of chloride-containing mortar at different RH and temperature conditions

Figure C.4 shows the pore saturation degrees of carbonated mortar and chloride-containing mortar at different RH and Temperature conditions

## APPENDIX C

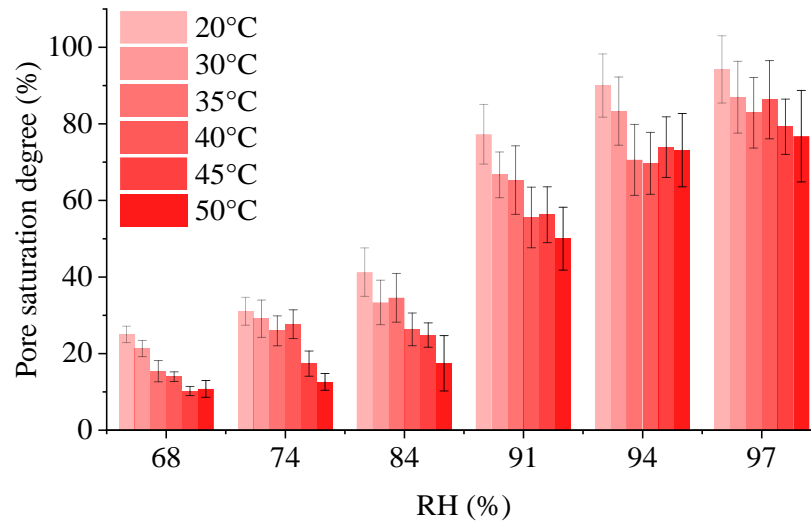


Figure C.4 Pore saturation degrees of chloride-containing mortar at different RH and temperature conditions

Figure C.5 shows the evolution of corrosion rate of steel rebar in the chloride-containing mortar at temperatures ranging from 20 °C to 50 °C under different RH conditions, in which each point refers to the average value obtained from four replicates. As expected, the corrosion rates of the steel rebar increased with increasing RH values.

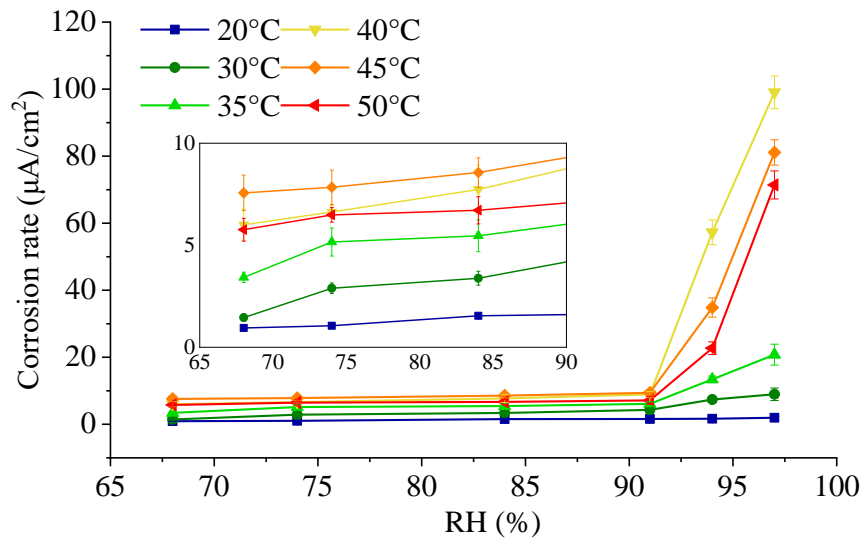


Figure C.5 Relationship of corrosion rate of steel rebar and RH in the chloride-containing mortar under variable temperature conditions

## APPENDIX C

It can be observed that the chloride-induced corrosion rate was approximately 40-50 times higher than the carbonation-induced corrosion rate under all environmental conditions (refer to Figure 3.12 and Figure C.5). A sudden increase in the in chloride-induced corrosion rate was 91% with a much more significant rising trend than which in carbonated mortar. The mortar saturation degree at the turning point of the chloride-containing mortar ranged from 50.0% to 77.3% (refer to Figure C.4).

Figure C.6 shows the evolution of the corrosion rate of the steel rebar in a chloride-containing mortar and carbonated mortar under variable temperature conditions. For chloride-induced corrosion, when the temperature was over 40 °C, the corrosion rate of steel rebar in the chloride-containing mortar under higher RH conditions (91%, 94%, 97%), showed a continuous attenuation, which indicates that the peak value of temperature was 40°C, that exists where the highest corrosion rate had occurred, while the peak value was 45°C at a relatively lower RH range of 68 to 84%. And the corrosion rate increased remarkably by approximately 5-45 times as the temperature increased from 20°C to the peak value.

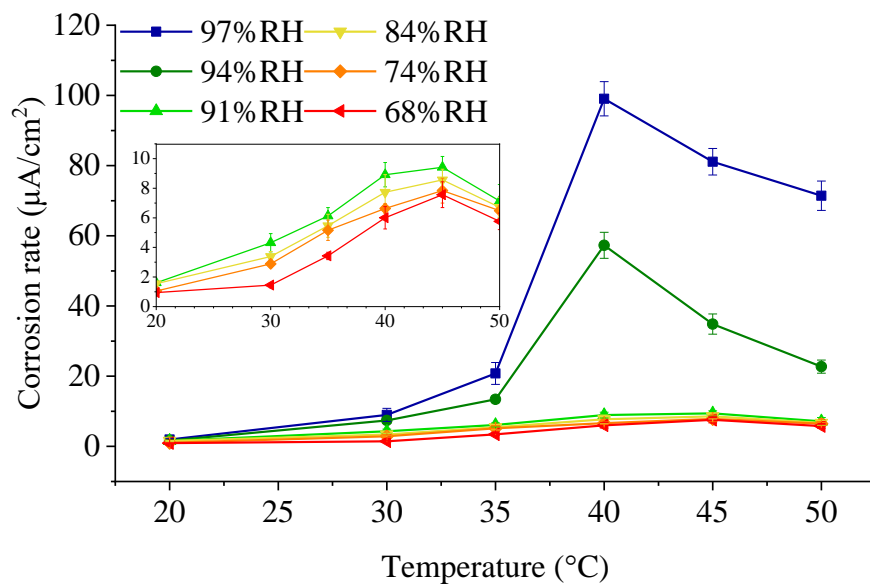


Figure C.6 Relationship of corrosion rate of steel rebar and temperature in the chloride-containing mortar under variable RH conditions

## APPENDIX C

The correlations between the corrosion rate and corrosion potential of steel rebar in the chloride-containing mortar under different environmental conditions are shown in Figure C.7. An increase of the corrosion rate can be generally found with corrosion potential shifting more negatively in spite of exposed environmental conditions. On the other hand, the exceptions occurred under 68%, 74% and 84%RH with 50°C, under 91%, 94% and 97%RH with 45°C and 50 °C conditions, where the corrosion rate decreased while the corrosion potential getting more negative.

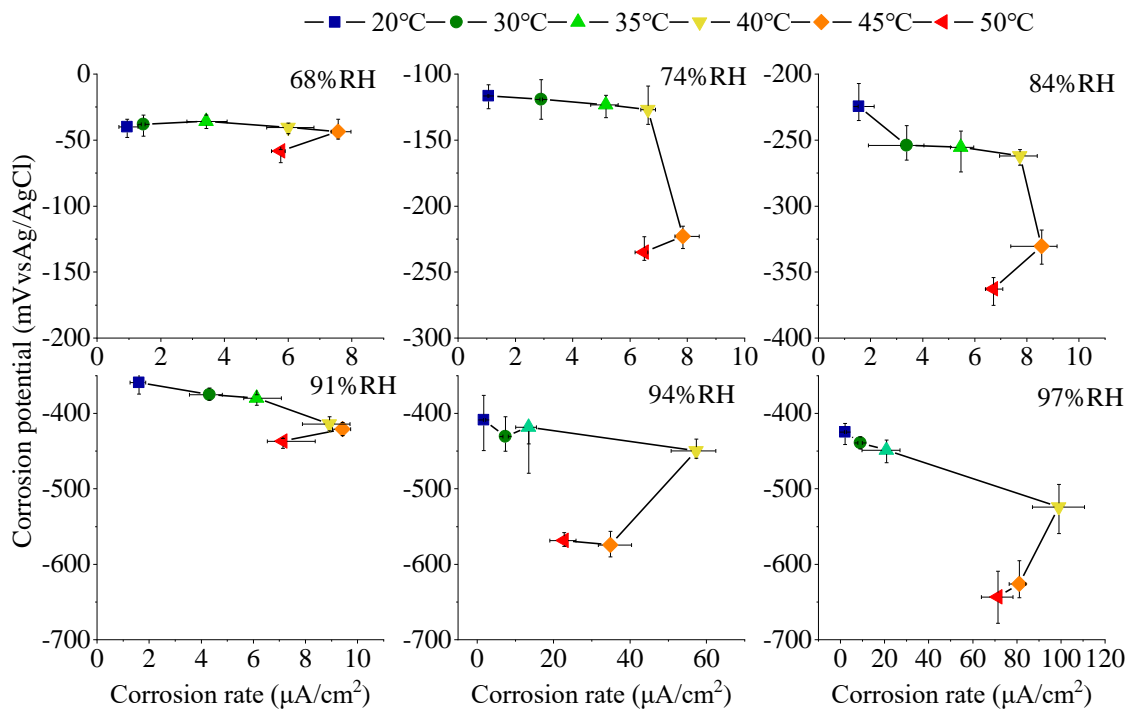


Figure C.7 The correlation between the corrosion rate and corrosion potential of steel rebar in the chloride-containing mortar under different temperatures for each RH condition (error bars represent the measured range)

The distributions of corrosion products in the chloride-containing mortar and carbonated mortar were examined at the steel/mortar interface and along the steel rebar surface.

The development of the corrosion product at the steel/mortar interface was observed and analyzed by means of SEM and EDS (TM4000Plus, HITACHI). Firstly, prismatic

## APPENDIX C

samples containing the steel rebar with a square base of  $20 \times 20 \text{ mm}^2$  were cut to thin slices of approximately 3 mm thickness for SEM observation. All the cuts were made with the precision diamond cut-off machine (ISOMET Low Speed Saw), with a diamond disc running across the prismatic sample. In order to avoid washing the corrosion products, liquid glycerin was used to cool the cutting disc. Secondly, these slices were inserted in a vacuum desiccator until constant weight and then impregnated with a low-viscosity epoxy resin. The resin was hardened for 20 hours. Thirdly, Surface polishing was performed by using a precious polish machine (MA-2000 MUSASHINO DENSHI) to improve imaging quality. In this process, grinding, polishing, and cleaning of the cross-sectional samples were performed without water to avoid the dissolution of rust. In the end, a field-emission scanning electron microscope (TM4000Plus, HITACHI) and operated in backscattered electron (BSE) mode were used to create the element maps of the steel/mortar interface in the chloride-contaminated mortar and carbonated mortar. Two chemical elements, iron and oxygen, were analyzed to examine corrosion products development on the steel/mortar interface.

SEM and Mapping images were adopted to observe the development of corrosion products at the steel/ mortar interface. The corrosion products are visible in the SEM image as a light grey layer on the surface of the steel rebar. The parent metal is in light color, while the dark grey area surrounding is mortar. For mapping images below, the areas with high levels of Fe (iron) are shown in yellow and the O (oxygen) is represented in green. As an example, Figure C.8 shows the mapping of the sectional area of reinforced chloride-containing mortar (a) and carbonated mortar (b) under 97% RH and 20°C condition. Depending on the availability and atomic weight of two elements (Fe and O), the four main layers involved in the corrosion process can be distinguished: steel, accumulated corrosion products, diffused corrosion products, and mortar.

## APPENDIX C

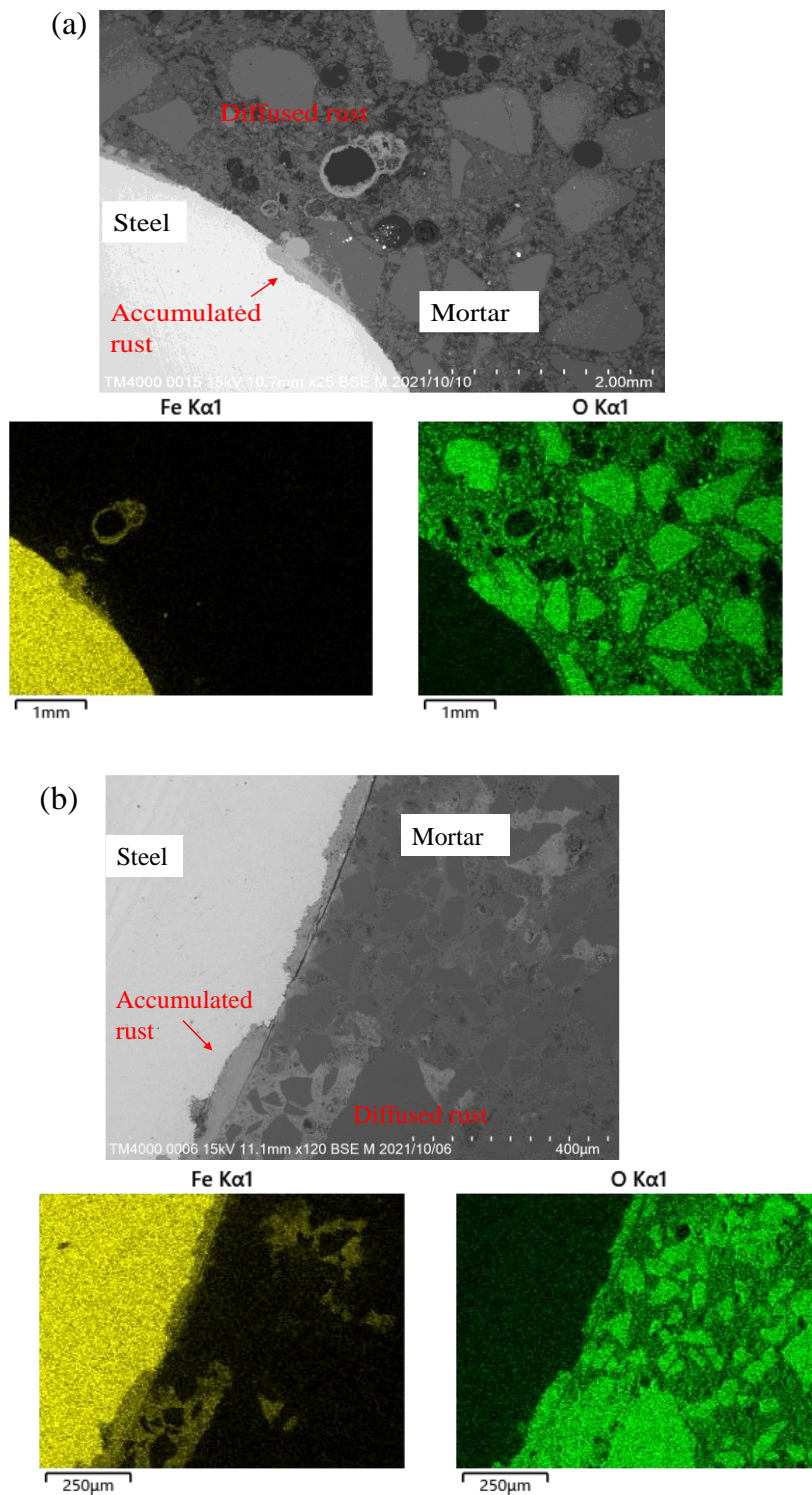


Figure C.8 BSE image at the steel/concrete interface in the chloride-containing mortar (a) and carbonated mortar.

## APPENDIX C

In the image of steel/mortar interface corresponding to chloride-induced corrosion (Figure C.8(a)), it can be observed that most of the formed corrosion product migrate through the mortar and deposited in air voids, while less corrosion products accumulated on the steel surface. In the image of the steel/mortar interface corresponding to carbonation-induced corrosion (Figure C.8(b)), most of the corrosion products are accumulated on the steel/mortar interface, and some were penetrated into the mortar.

### C.3 Discussion

#### C.3.1 The electrical resistivity of chloride-containing mortar

The relationship between the electrical resistivity and water content in the chloride-containing mortar under each temperature condition is shown in Figure C.9. As expected, the electrical resistivities of the chloride-containing mortar decreased as the water content increased, which is similar to the changing trend in carbonated mortar.

The electrical resistivity of the chloride-containing mortar is much lower than that of the carbonated mortar when the exposed conditions are the same (refer to Figure 3.19 and Figure C.9), which can be attributed to different electrolyte compositions and different amounts of electrolyte owing to the different microstructures of the mortars. The carbonated mortar had a lower water content under each RH condition (Figure 3.17 and Figure C.3), resulting from the finer pore system in the carbonated mortar by the clogging effect (Figure C.2). A lower electrolyte amount and finer pore system in the carbonated mortar provided fewer channels for current to pass through, leading to a higher electrical resistivity. Another possible reason is that the C-S-H phase, whose O-



## APPENDIX C

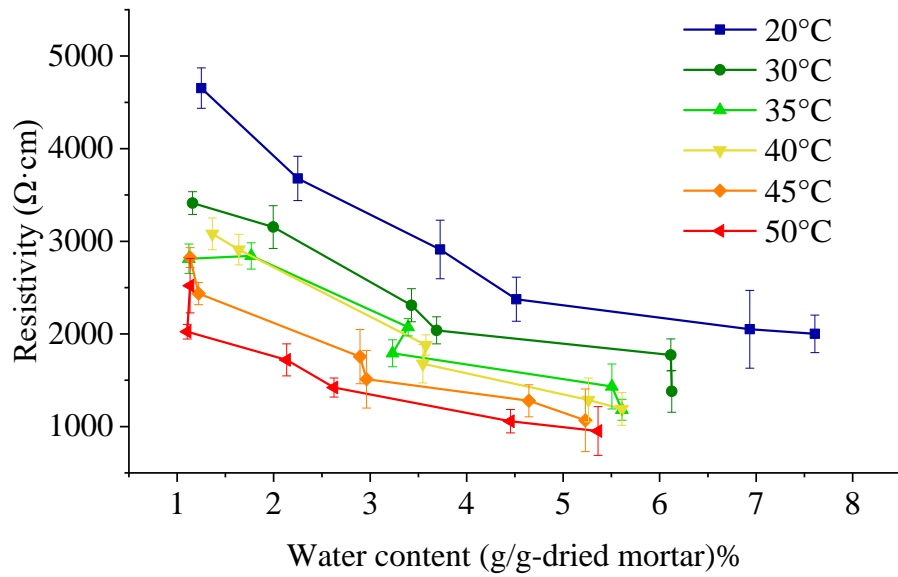


Figure C.9 Relationship of electrical resistivity and water content in the chloride-containing mortar under variable temperature conditions

H groups on the surfaces, including interlayer spaces, contribute to higher ion conductivity [40], is decalcified by the carbonation process. Simultaneously, the conductive free alkali metal content (sodium and potassium) was bounded by decalcified C-S-H [132][133] and decreased in the electrolyte. All these reasons are attributed to the increase in electrical resistivity of the mortar.

In addition, the electrolyte content, including chloride ions, plays an essential role in the conduction of mortar, and the existence of chloride ions increases the ion concentration of the pore solution, providing more ions to carry the current, thus lowering the electrical resistivity. To prove the effect of chloride ions in the pore solution on the electrical resistivity of the mortar, the electrical resistivities of carbonated mortar saturated with sodium chloride solution and ionized water were tested. As shown in Figure C.10, the presence of chloride ions resulted in a decrease in the electrical resistivity of the mortar.

Concerning the effect of temperature on the electrical resistivity of mortar, the elevated temperature increases the mobility of free ions through the pore electrolyte and the conductivity of the silica, alumina, and interlayer calcium ions weakly bound by C-S-H [77] and alkali metal hydroxides (sodium and potassium hydroxide), resulting in a

## APPENDIX C

reduction in the electrical resistivity of chloride-containing mortar (refer to Figure C.9). The temperature dependence of the electrical resistivity can be determined from the value of the apparent activation energy  $E_{app}$  in the Arrhenius equation (refer to Eq. (3.9) and Eq. (3.10).

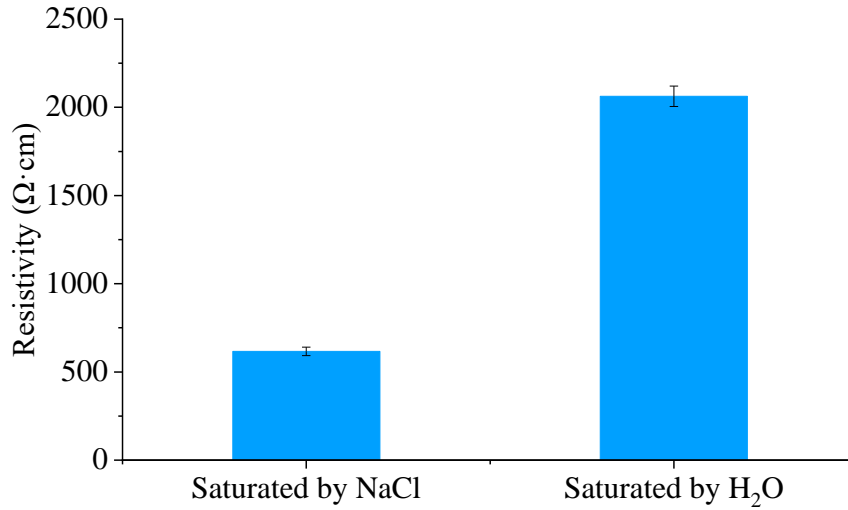


Figure C.10 Electrical resistivity of carbonated mortar saturated by sodium chloride solution with a concentration of 3.8% (consistent with the mix proportion in Table C.1 Mix proportion of chloride-containing mortar) and ionized water

### C.3.2 Prediction of electrical resistivity of chloride-containing mortar under different environmental conditions

Figure C.11 presents the logarithm of the electrical resistivity of mortars against the reciprocal of the absolute temperature ( $1/T$ ) at each water content in chloride-containing mortar, in which the electrical resistivity of mortar at each water content was determined by polynomial curve fitting of the data points in Figure C.9. The linear relationship between the logarithms of the electrical resistivity of the mortars and the reciprocal of the absolute temperature can be explained by the Arrhenius plot (refer to Figure C.11), and the apparent activation energy  $E_{app}$  can be determined from the slope of the regression line.

## APPENDIX C

The apparent activation energy  $E_{app}$  of the electrical resistivity of the chloride-containing mortars with each amount of water content determined by Eq. (3.10) is also presented at the end of each line in Figure C.11. In comparison with the phenomenon that a decreasing tendency of  $E_{app}$  with an increase in water content was observed in carbonated mortar, the  $E_{app}$  values of electrical resistivity in chloride-containing samples did not show any obvious changing trends. As more C-S-H existed in the chloride-containing mortar, the interconnectivity of the electrolyte via the water remaining in the micropores around the C-S-H was relatively stable; thus, the temperature dependence of the electrical resistivity of the chloride-containing mortar remained relatively constant. In addition, the  $E_{app}$  values of chloride-containing mortar were higher than those of carbonated mortar (refer to Figure 3.20 and Figure C.11), which could be attributed to chloride desorption with increasing temperature [134][135]. The bound chloride ions and free chloride ions can be described by the chloride ions binding isotherm, which obeys the Freundlich equation [136], and the increase in the amount of free mobile chloride ions released from the physically absorbed chloride on the hydration product surface will increase the sensitivity to temperature change.

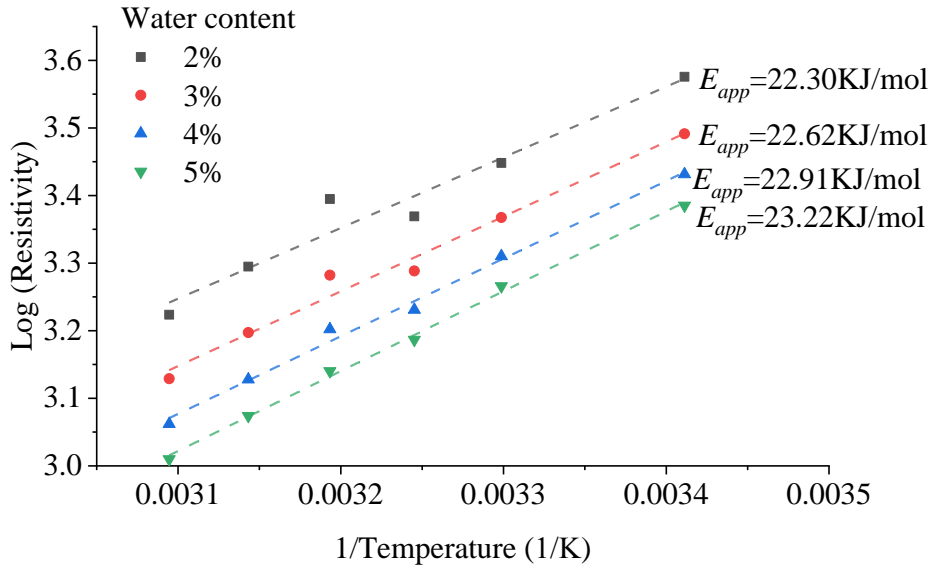


Figure C.11 Arrhenius plots of electrical resistivity of chloride-containing mortars

Therefore, for the prediction of the electrical resistivity of chloride-containing mortar at different RHs and temperatures, the electrical resistivity ( $R_0$ ) of mortar at 20 °C

## APPENDIX C

(273.15 K) can be used as the initial value of the line, whereas the slope is determined by activation energy  $E_{app}$  (Eq. (3.18)) due to the linear relationship between the logarithm of the electrical resistivity ( $\log R$ ) and the reciprocal of temperature ( $1/T$ ). The estimation equations for  $R_0$  in the chloride-containing mortar can be derived using the water content  $w$  as the independent variable:

$$R_0 = 4246w^{-0.48}, R^2 = 0.99 \quad (C.1)$$

Then, following the stable values of  $E_{app}$  in the chloride-containing mortar (Figure C.11), the  $E_{app}$  can be determined by the average value:

$$E_{app} = 22.8\text{KJ/mol} \quad (C.2)$$

Finally, with the known values of the initial value  $R_0$  at 20 °C (273.15K) and apparent activation energy  $E_{app}$ , the electrical resistivity of chloride-containing mortar can be calculated for the given water content and temperature.

It should be mentioned that the amount of chloride content in chloride-containing mortar may influence the presented results. If the total chloride content contained in mortar decreases, the free mobile chloride ions will reduce according to the chloride ions binding isotherm, thus inhibiting the ability to carry the current and increasing the electrical resistivity of mortar. Correspondingly, the free mobile chloride ions released in the pore solution with the elevating temperature will be fewer than those in the mortar sample containing higher total chloride content, which can cause a decrease in sensitivity of the electrical resistivity to temperature changes; in other words, the  $E_{app}$  may decrease with the lower total chloride content amount. Therefore, based on the assumptions above, the effect degree of chloride content amount on the electrical resistivity of mortar will be studied further.

## APPENDIX C

### C.3.3 Effect of RH and temperature on chloride-induced corrosion rate

Figure C.12 shows the relationship between the corrosion rate of the steel rebar and the water content in the chloride-containing mortar. As the ion flow is promoted by the increased water content in the pore system, the corrosion rate increases as expected.

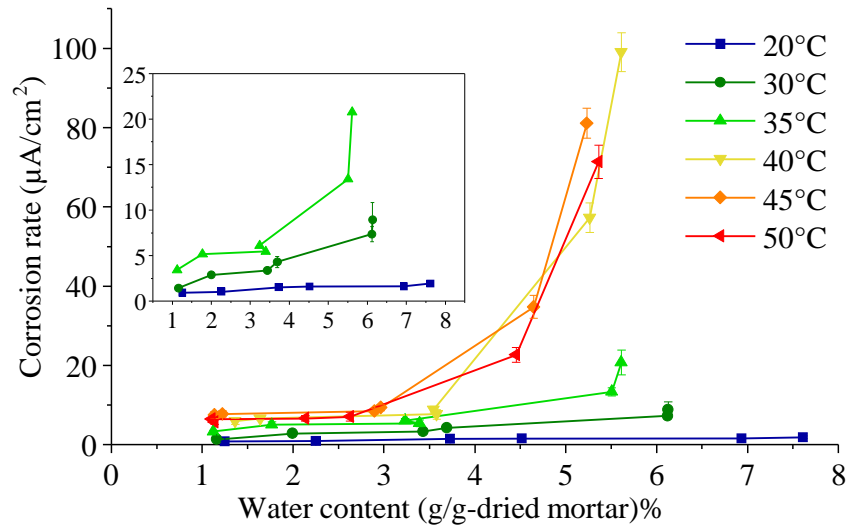


Figure C.12 Relationship of corrosion rate of steel rebar and water content in the chloride-containing mortar (b) under variable temperature conditions

The turning points of 91%RH in chloride-containing mortar are shown in Figure C.5 due to the interconnectivity of electrolytes and anodic reaction in the corrosion process. The concentrations of  $Fe^{2+}$  and  $O_2$  on the steel rebar surface affect the reversible potential of the anodic and cathodic reactions in which they are involved as described by the Nernst equations in Eqs. (3.12) and (3.14) in Chapter 3.

According to Nernst equation Eq. (3.12), when the interconnectivity of electrolytes in the pore system is established under high RH conditions, the formed interconnectivity of the electrolyte drastically increases the possible diffusion of iron ions released by the anodic reaction, leaving the steel rebar surface to the bulk. The reduction of the iron ion concentration at the steel rebar surface decreases the anodic reversible potential,

## APPENDIX C

resulting in a significant increase in the corrosion rate. The chloride-containing mortar had a relatively lower turning point of RH than carbonated mortar (refer to Figure 3.12 and Figure C.5) because of the coarser microstructure and more condensed water content (refer to Figure 3.17, Figure C.2 and Figure C.3), which established the interconnectivity of the electrolyte under a lower RH condition.

The corrosion reaction of steel represents an electrochemical reaction; thus, the ion diffusion rate is dependent on the ambient temperature, that is, the elevated temperature accelerates the corrosion rate of the steel rebar. In addition, an increase in temperature accelerates the permeability of oxygen, which is essential for the cathodic reaction, and increases the corrosion rate when the anodic reaction rate corresponds (Figure C.6). This result was also confirmed by the experimental results of the chloride-containing concrete [52] exposed to the temperature conditions ranging from 20 °C to 40 °C. The temperature peak values were 40-45 °C in chloride-containing mortar (Figure C.6). The decrease in the corrosion rate of steel when the temperature was above the peak temperature could be attributed to the decrease in the concentration of dissolved oxygen in the electrolyte. As the examples of obtained Nyquist plots of steel rebar in chloride-containing mortar under 97% and 50 °C conditions with a border frequency range of 0.0005-10000 Hz shown in Figure C.13, the capacitive semicircle representing the diffusion impedance verifies the limitation of oxygen supply on the steel surface. According to the Nernst equation Eq. (3.14), the decreased concentration of dissolved oxygen leads to a reduction in the cathodic reversible potential  $E_c^0$ , the difference in reversible potential between the anode and cathode decreases, which represents the driving force of the corrosion reaction, thus resulting in a decrease in the corrosion rate.

## APPENDIX C

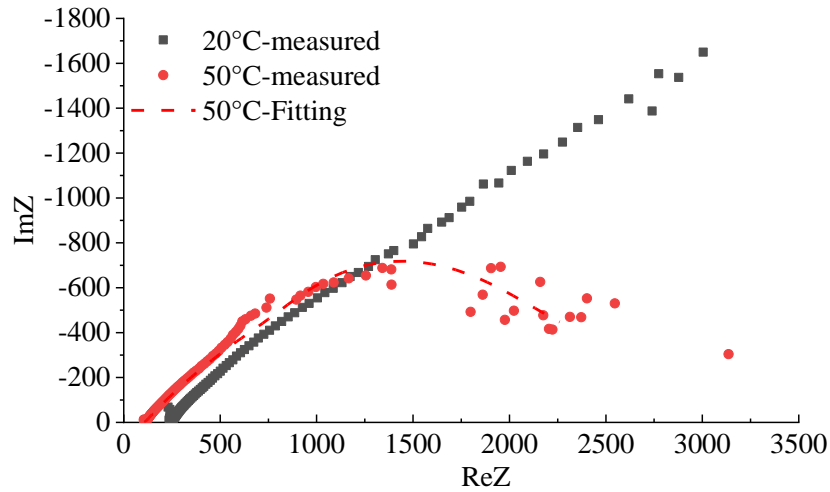


Figure C.13 Nyquist plots of steel rebar in chloride-containing mortar under 97% RH condition with the controlled temperature of 20 °C and 50 °C

For each environmental condition, the chloride-induced corrosion rate of the steel rebar was almost 10-50 times higher than that of the carbonation-induced rebar, as clearly observed in Figure 3.13 and Figure C.6. This phenomenon can be attributed to several factors. First, the difference in the steel corrosion initiation mechanisms of the two types of mortars should be considered. Regarding carbonation-induced corrosion, carbonation in the mortar, which leads to a decrease in pH in the pore solution, destroys the passive layer, exposes the bare steel to a moist environment, and then initiates corrosion. On the other hand, chloride-induced corrosion initiation depends on the ratio of the chloride ion concentration  $[Cl^-]$  that destroys the passive layer to the hydroxide ion concentration  $[OH^-]$  that forms a passive layer on the steel surface [14]. If the ratio  $[Cl^-]/[OH^-]$  is above a threshold value, the passive layer on the steel surface is destroyed, and chloride-induced corrosion is initiated. Chloride ions act as a catalyzer to dissolve iron at the anodic site [137]. Thus, the iron dissolved in the chloride-containing mortar was much faster than that dissolved in the carbonated mortar. In addition, the corrosion products formed during the corrosion reaction also play an essential role. It has been reported that  $\alpha$ -,  $\beta$ -,  $\gamma$ - $FeOOH$ ,  $\gamma$ - $Fe_2O_3$ ,  $Fe_3O_4$ , and amorphous oxyhydroxides are present in rust [26][138], and it was assumed that small rust particles were packed densely to form a tightly adherent film that acted as a barrier

## APPENDIX C

protecting the steel from further corrosion. For carbonation-induced corrosion, ferrous hydroxides are generated homogeneously and further oxidized to lepidocrocite ( $\gamma$ - $FeOOH$ ) and goethite ( $\alpha$ - $FeOOH$ ) [139] with low solubility at near-neutral pH. Thus, solid corrosion products tend to precipitate in the pores near the steel rebar to form an accumulated corrosion product layer as Figure C.8(b) shows, impeding further diffusion of  $Fe^{2+}$ . In comparison, the presence of chloride increases the solubility of  $Fe^{2+}$  ions, which prevents their rapid precipitation and allows their diffusion and migration away from the steel surface [140]. In this case, most of the corrosion products formed by chloride-induced corrosion penetrate through the mortar and precipitate in air voids as detected in Figure C.8(a) and only a little corrosion product accumulated on the steel surface, which does not have obvious effect on iron dissolution



Figure C.14 Steel rebar removed from chloride-containing mortar under 68% RH, 97% RH and 20 °C, 40 °C

A chloride-induced corrosion rate, almost an order of magnitude larger than the carbonation-induced corrosion rate was also detected in previous studies [34][141][142], whereas in this study, much larger differences between the corrosion rates were found owing to the higher variable exposed temperatures. In addition, free chloride ions can be released from the physically absorbed chloride on the C-S-H surface to the pore electrolyte at elevated temperatures [134]; more active chloride ions exist adjacent to the anodic area, promoting iron dissolution and a higher degree of corrosion rate. It should be noted that the dramatic increase in the chloride-induced



## APPENDIX C

corrosion rate occurred under high temperature and high RH conditions (refer to Figure C.6 and Figure C.12), which can be explained by the more severe pitting corrosion caused by the higher chloride concentration with increasing temperature. Figure C.14 shows the steel rebar removed from the chloride-containing mortar under 68%RH and 97%RH with a lower temperature of 20 °C, and higher temperature of 40 °C conditions and the rust on the surface was chemically cleaned following standard systematic step [90]. It can be observed that the corrosion pit deepened and expanded on the steel rebar surface with increasing temperature, which can make the effect of increasing chloride ions on the corrosion rate more prominent with a large amount of electrolyte. A similar trend of chloride-induced corrosion patterns was also reported in [89] by visual observation and SEM images of corrosion products under 85%RH, indicating that the corroded surface of steel rebar was larger at 40 °C than at 30 °C.

As the corrosion of steel was initiated by the chloride content, the step-limiting corrosion (refer to Figure 3.24) can be deduced from the correlation between the corrosion potential and the corrosion rate of steel rebar, and the correlation between the electrical resistivity of the mortar and the corrosion rate.

Two corrosion controlling mechanisms, resistive control and cathodic control, were illustrated in Evans plots as show in Figure 3.25, and mentioned in Section 3.4.3 (Chapter 3). From Figure C.7, the phenomenon that corrosion potential decreased with the decreased corrosion rate occurred under 68%, 74% and 84%RH with 50°C, and 91%, 94% and 97%RH with 45°C and 50 °C conditions, which indicates the corrosion processes were under cathodic control.

## APPENDIX C

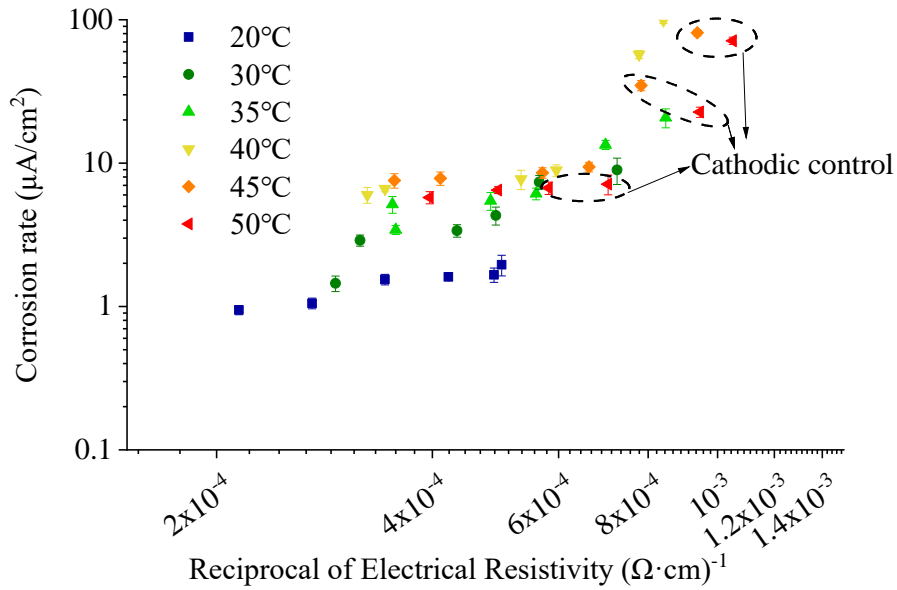


Figure C.15 Relationship between reciprocal of electrical resistivity and corrosion rate in chloride-containing mortar

In addition, as shown in Figure C.15, the correlated linear relationship between the corrosion rate and the reciprocal of electrical resistivity (the data of electrical resistivity of chloride-containing mortar was adopted from Figure C.1) indicates that the corrosion process is under resistive control in most environmental conditions, as suggested by several authors [94][91][95]. However, the temperature effect and comparison between the controlling mechanisms of carbonation-induced and chloride-induced corrosion are scarcely discussed. Some corrosion processes were under cathodic control owing to the limitation of oxygen supply when the temperature was over 40°C to 45°C. with high water content states, which are circled by dashed lines in the figure. The more scattered data in chloride-containing mortar compared to the carbonated mortar (refer to Figure 3.26) indicates that the relationship between the electrical resistivity of mortar and the corrosion rate is less than that in carbonated mortar because RH and temperature not only change the current flow but also alternate the anodic catalytic reaction, anodic reversible potential, and development of pitting shape on the steel rebar surface.

## APPENDIX C

The chloride-induced corrosion that is much severer than the carbonation-induced corrosion can be attributed to the coarser microstructure, more conductive phase in the mortar, catalyzed anodic reaction by chloride ions and increased chloride ions in electrolyte with increasing temperature, and corrosion products with relatively high solubility, finally, the deeper and expanded pit shape on the steel surface (refer to Figure C.14). The regression dashed line ( $\log i_{corr} = slope \cdot \log \left( \frac{1}{R} \right) + constant$ ) with a slope of 2.97 and a correlation coefficient of 0.7 was presented in Figure C.16 when corrosion process is under resistive control in chloride-containing mortar.

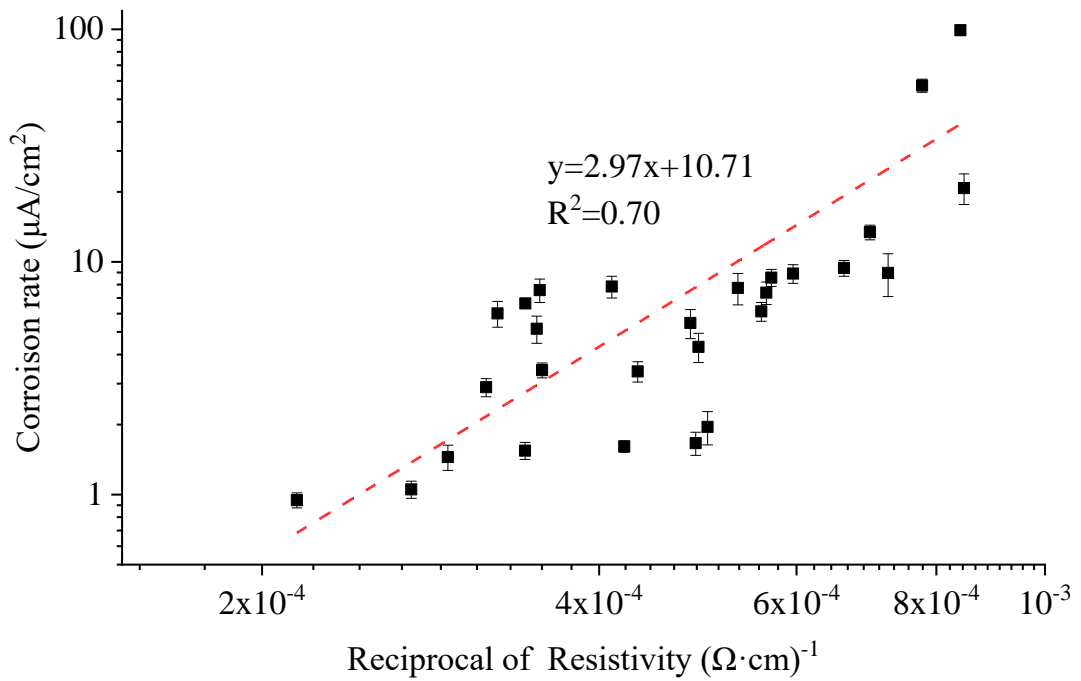


Figure C.16 Relationship between reciprocal of electrical resistivity and corrosion rate

Such a resistive controlling mechanism of the corrosion process can be applied in the estimation of the corrosion rate of steel rebars under different environmental conditions using the relationships among the electrical resistivity of cement materials in RC structures, water content, and temperature.

## APPENDIX C

The electrical resistivity of chloride-containing mortar can be calculated for the given water content and temperature by Eq. (C.1) and (C.2), the corrosion rate of steel rebar in chloride-containing mortar exposed to variable environmental conditions can be estimated following the linear relationship between corrosion rate and the reciprocal of electrical resistivity in Figure C.16.

### C.4 Summary

The changing trends of electrical resistivity of chloride-containing mortar concerning RH (water content) and temperature were similar to those of carbonated mortar, while the electrical resistivity values of chloride-containing mortar were relatively lower because of the larger pore size, higher water content, higher ion concentration, and conductive C-S-H inside.

The temperature dependence of electrical resistivity in the chloride-containing mortar was relatively stable concerning the water content of the mortar. The activation energy values of electrical resistivity in chloride-containing mortar were higher than that in carbonated mortar because the free mobile chloride ion released from the physically absorbed chloride on the hydration product surface will increase the sensitivity to temperature change.

A prediction equation of electrical resistivity of chloride-containing mortar was proposed based on the linear relationship between water content and initial electrical resistivity at 20°C and the stable apparent activation energy.

The corrosion rate in the chloride-containing mortar was always higher than that in the carbonated mortar because of the coarser pore structures with more available channels for ion movement, higher ion concentrations in the electrolyte, and corrosion products with relatively high solubility owing to the existence of chloride. In addition, for the effect of temperature on the higher corrosion rate in chloride-containing mortar, the chloride ions dissolve iron in the catalyzed reaction much faster than anodic reaction in carbonation-induced corrosion process, the elevated temperature released more free chloride ions, and the pitting shape developed and expanded under the high RH and

## APPENDIX C

temperature conditions. The turning point of RH was 91% for the chloride-induced corrosion rate, which is lower than the carbonation-induced corrosion rate owing to the coarser microstructure and higher water content. The decline in corrosion rate occurred when the temperature was over 40-45 °C, which was similar to the carbonation-induced corrosion, indicating that the corrosion process was also limited by supplied oxygen to the steel surface.

The corrosion control mechanisms were verified by the correlation between the corrosion potential and corrosion rate of the steel rebar, and the correlation between electrical resistivity of the mortar and the corrosion rate. The relative less relevance between the electrical resistivity of the mortar and the corrosion rate in chloride-containing mortar could be due to the complex influence of environmental conditions on the anodic catalytic reaction, reversible potential, and development of the pitting shape. The cases of corrosion process under cathodic control under specific conditions can also be verified by the decreased corrosion rate of steel rebar accompanied by a negative shift of corrosion potential.

The linear regression trend line of the data detected in the chloride-containing mortar roughly indicates that the corrosion process is under resistive control. The regression analysis model of the electrical resistivity of cement materials enables an engineering application to estimate the corrosion rate of steel rebars under different exposure conditions. In this study, the resistive controlled corrosion process was under 68% to 91%RH with temperatures ranging from 20 °C to 45 °C, and 94 to 97%RH with temperatures ranging from 20 °C to 40 °C for chloride-induced corrosion.

## APPENDIX D

### APPENDIX D THE ESTIMATION OF CORROSION RATE OF STEEL REBAR IN CARBONATED MORTAR DURING RAINFALL

Figure D.1 shows the corrosion rate of steel rebar evolution in the carbonated reinforced mortar samples exposed to the cyclic wetting-and-drying conditions at 20°C. The average corrosion rate value during the wetting period can be assumed to be the representative value of the corrosion rate of mortar during rainfall. Since the reinforced mortar sample with a cover thickness of 8 mm, the estimated corrosion rate values for each concrete member should consider the effect of different cover thicknesses following the Eqs. (4.1) and (4.2). Consequently, the corrosion rate of steel rebar for each concrete member during the rainfall days can be calculated and summarized in Table D.1.

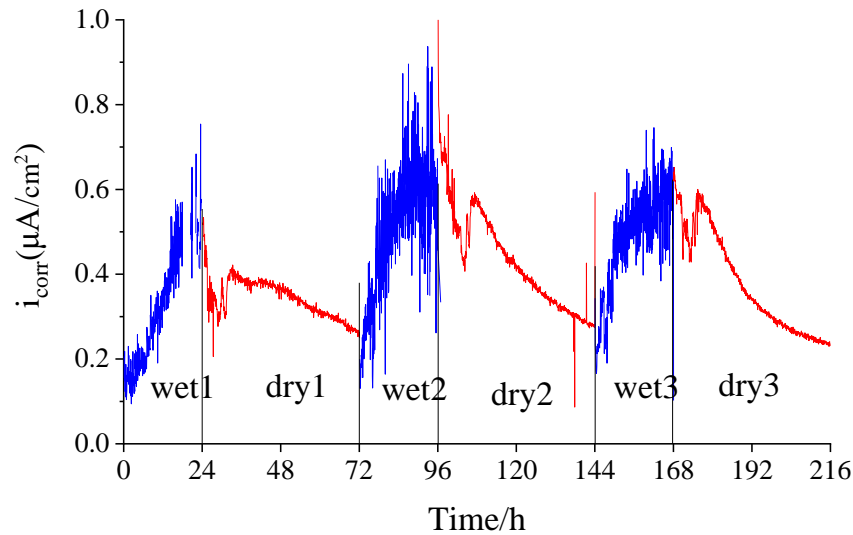


Figure D.1 Corrosion rate evolution during the cyclic wetting-and-drying cycles

Table D.1 The corrosion rate of steel rebar of each concrete member during rainfall days

Location	Concrete members	Cover thickness D(mm)	Corrosion rate during rainfall in the first year ( $\mu\text{A}/\text{cm}^2$ )	Corrosion rate during rainfall in the second year ( $\mu\text{A}/\text{cm}^2$ )
Exterior	Column	36	0.064	0.021
	Beam	40	0.055	0.018
	Wall	32	0.074	0.025
Interior	Beam	29	0.085	0.028
	Wall	26	0.099	0.033
	Floor slab	31	0.078	0.026

## REFERENCE

### REFERENCE

- [1] H. F. W. Taylor, "Cement chemistry," *Cem. Chem.*, 1997, doi: 10.1680/cc.25929.
- [2] U. Angst *et al.*, "Corrosion of steel in carbonated concrete: Mechanisms, practical experience, and research priorities – A critical review by RILEM TC 281-CCC," *RILEM Tech. Lett.*, vol. 5, pp. 85–100, 2020.
- [3] L. Bertolini, B. Elsener, P. Pedeferri, and R. Polder, *Corrosion of Steel in Concrete Corrosion*. 2004.
- [4] A. Poursaei, *Corrosion of Steel in Concrete Structures*. 2016.
- [5] Tuutti, *Corrosion of steel in concrete*. Dissertation. Lund University, Sweden: Swedish Cement and Concrete Research Institute, 1982.
- [6] U. M. Angst, "Challenges and opportunities in corrosion of steel in concrete," *Mater. Struct. Constr.*, vol. 51, no. 1, pp. 1–20, 2018.
- [7] U. M. Angst *et al.*, "Present and future durability challenges for reinforced concrete structures," *Mater. Corros.*, vol. 63, no. 12, pp. 1047–1051, 2012.
- [8] S. E. Hussain, Rasheeduzzafar, A. Al-Musallam, and A. S. Al-Gahtani, "Factors affecting threshold chloride for reinforcement corrosion in concrete," *Cem. Concr. Res.*, vol. 25, no. 7, pp. 1543–1555, 1995.
- [9] S. Ishida, K., Takewaka, K., Yamaguchi, T. and Maeda, "Experimental study on quantitative evaluation of the chloride threshold value," *Proc. Japan Concr. Inst.*, vol. 29, no. 1, pp. 1065–1070, 2007.
- [10] L. Li and A. A. Sagüés, "Chloride corrosion threshold of reinforcing steel in alkaline solutions-effect of specimen size," *Corrosion*, vol. 60, no. 2, pp. 195–202, 2004.
- [11] K. Horiguchi, T. Yamaguchi, T. Maruya, and K. Takewaka, "Study on the method of measuring the chloride threshold value of corrosion and estimation of the values in durability design of concrete structures," *J. Adv. Concr. Technol.*, vol. 18, no. 10, pp. 571–587, 2020.
- [12] G. K. Glass and N. R. Buenfeld, "The presentation of the chloride threshold level for corrosion of steel in concrete," *Corros. Sci.*, vol. 39, no. 5, pp. 1001–1013, 1997.

## REFERENCE

- [13] K. Horiguchi, T. Yamaguchi, T. Maruya, and K. Takewaka, "A Study on the Method of Measuring the Chloride Threshold Value of Corrosion and on the Estimation of the Values," *J. Japan Soc. Civ. Eng.*, vol. 71, no. 2, pp. 107–123, 2015.
- [14] Y. Hosokawa, D. Mori, and K. Yamada, "A Study on the Notation of the Steel Corrosion Limit Concentration of Chloride Ion in Concrete," *Japan Concr. Inst.*, vol. 26, no. 1, pp. 909–914, 2004.
- [15] C. Alonso, M. Castellote, and C. Andrade, "Chloride threshold dependence of pitting potential of reinforcements," *Electrochim. Acta*, vol. 47, no. 21, pp. 3469–3481, 2002.
- [16] R. Gopal and B. Sangoju, "Carbonation-Induced Corrosion: A Brief Review on Prediction Models," *J. Inst. Eng. Ser. A*, vol. 101, no. 2, pp. 247–257, 2020.
- [17] *Standard Specifications for Concrete Structures-Maintenance*. JAPAN SOCIETY OF CIVIL ENGINEERS, 2018.
- [18] I. S. Yoon, O. Çopuroğlu, and K. B. Park, "Effect of global climatic change on carbonation progress of concrete," *Atmos. Environ.*, vol. 41, no. 34, pp. 7274–7285, 2007.
- [19] M. Castellote, L. Fernandez, C. Andrade, and C. Alonso, "Chemical changes and phase analysis of OPC pastes carbonated at different CO<sub>2</sub> concentrations," *Mater. Struct. Constr.*, vol. 42, no. 4, pp. 515–525, 2009.
- [20] Y. Ji, Y. Yuan, J. Shen, Y. Ma, and S. Lai, "Comparison of concrete carbonation process under natural condition and high CO<sub>2</sub> concentration environments," *J. Wuhan Univ. Technol. Mater. Sci. Ed.*, vol. 25, no. 3, pp. 515–522, 2010.
- [21] H. Cui, W. Tang, W. Liu, Z. Dong, and F. Xing, "Experimental study on effects of CO<sub>2</sub> concentrations on concrete carbonation and diffusion mechanisms," *Constr. Build. Mater.*, vol. 93, pp. 522–527, 2015.
- [22] B. Šavija and M. Luković, "Carbonation of cement paste: Understanding, challenges, and opportunities," *Constr. Build. Mater.*, vol. 117, pp. 285–301, 2016.
- [23] G. W. Groves, D. I. Rodway, and I. G. Richardson, "The carbonation of hardened cement pastes," *Adv. Cem. Res.*, vol. 3, no. 11, pp. 117–125, 1990.



## REFERENCE

- [24] T. Grounds, H. G Midgley, and D. V Novell, “Carbonation of ettringite by atmospheric carbon dioxide,” *Thermochim. Acta*, vol. 135, no. C, pp. 347–352, 1988.
- [25] T. D. Marcotte, “Characterization of Chloride-Induced Corrosion Products that form in Steel-Reinforced Cementitious Materials,” 2001.
- [26] J. P. Broomfield, *Corrosion of Steel in Concrete*. Abingdon, UK: Taylor & Francis, 1997.
- [27] K. Kishitani, “Some Consideration on Durability of Reinforced Concrete Structure,” *Trans. Archit. Inst. Japan*, vol. 65, no. 0, pp. 9–16, 1960.
- [28] 依田彰彦, “鉄筋コンクリート造建築物の中性化と耐用年数予測,” *Mater. Raify Gakkaishi*, vol. 17, no. 1, pp. 2–6, 2005.
- [29] 森永繁, “鉄筋の腐食速度に基づいた鉄筋コンクリート建築物の寿命予測に関する研究,” 1986.
- [30] S. Morinaga, “Prediction of service lives of reinforced concrete buildings based on the corrosion rate of reinforcing steel,” in *Durability of Building Materials and Components*, 1990, pp. 5–17.
- [31] S. Ahmad, “Empirical modelling of indicators of chloride-induced rebar corrosion,” *J. Struct. Eng.*, vol. 27, no. 3, pp. 195–207, 2000.
- [32] T. Yonezawa, F. Oshida, Y. Yamaguchi, H. Okamoto, and M. Nakao, “CORROSION RATE OF STEEL REINFORCEMENTS AFTER CARBONATION OF CONCRETE,” *J. Struct. Constr. Eng*, vol. 79, pp. 1405–1414, 2014.
- [33] C. Andrade and R. d’Andrea, “Electrical Resistivity As Microstructural Parameter for the Modelling of Service Life of Reinforced Concrete Structures,” *2nd Int. Symp. Serv. Life Des. Infrastruct.*, no. October, pp. 379–388, 2010.
- [34] K. Hornbostel, C. K. Larsen, and M. R. Geiker, “Relationship between concrete resistivity and corrosion rate - A literature review,” *Cem. Concr. Compos.*, vol. 39, pp. 60–72, 2013.
- [35] A. Lindvall, “Probabilistic Performance Based Durability Design of Concrete

## REFERENCE

- Structures: Statistical Quantification of the Variables in the Limit State Functions,” *Rep. No. BE95-1347*, pp. 1–10, 2000.
- [36] S. G. M. J.H. Bungey, S.G. Millard, J. H. Bungey, *Testing of Concrete in Structures-Spon Press*. 1995.
- [37] W. Morris, A. Vico, M. Vazquez, and S. . de Sanchez, “Corrosion of reinforcing steel evaluated by means of concrete resistivity measurements,” *Corros. Sci.*, vol. 44, no. 1, pp. 81–99, Jan. 2002.
- [38] C.Andrade and C.Alonso, “Corrosion rate monitoring in the laboratory and on-site,” *Science (80-. )*, vol. 10, no. 5, pp. 315–328, 1996.
- [39] T. Saeiki, N. Otsuki, and S. Nagarak, “Quantitative Estimation of Steel Corrosion in Mortar due to Carbonation,” *J. Japan Soc. Civ. Eng.*, vol. 30, pp. 55–66, 1996.
- [40] J. Gulikers, “Theoretical considerations on the supposed linear relationship between concrete resistivity and corrosion rate of steel reinforcement,” *Mater. Corros.*, vol. 56, no. 6, pp. 393–403, 2005.
- [41] G. K. Glass, C. L. Page, and N. R. Short, “Factors affecting the corrosion rate of steel in carbonated mortars,” *Corros. Sci.*, vol. 32, no. 12, pp. 1283–1294, 1991.
- [42] S. Feliu, J. A. González, S. Feliu, and C. Andrade, “Relationship between conductivity of concrete and corrosion of reinforcing bars,” *Br. Corros. J.*, vol. 24, no. 3, pp. 195–198, 1989.
- [43] M. Stefanoni, U. M. Angst, and B. Elsener, “Electrochemistry and capillary condensation theory reveal the mechanism of corrosion in dense porous media,” *Sci. Rep.*, vol. 8, no. 1, pp. 1–10, 2018.
- [44] M. Stefanoni, U. M. Angst, and B. Elsener, “Kinetics of electrochemical dissolution of metals in porous media,” *Nat. Mater.*, vol. 18, no. 9, pp. 942–947, 2019.
- [45] R. R. Hussain and T. Ishida, “Enhanced electro-chemical corrosion model for reinforced concrete under severe coupled action of chloride and temperature,” *Constr. Build. Mater.*, vol. 25, no. 3, pp. 1305–1315, 2011.
- [46] S. C. Kranc and A. A. Sagüés, “Detailed modeling of corrosion macrocells on steel reinforcing in concrete,” *Corros. Sci.*, vol. 43, no. 7, pp. 1355–1372, 2001.

## REFERENCE

- [47] G. Balabanić, N. Bićanić, and A. Dureković, “The influence of w/c ratio, concrete cover thickness and degree of water saturation on the corrosion rate of reinforcing steel in concrete,” *Cem. Concr. Res.*, vol. 26, no. 5, pp. 761–769, 1996.
- [48] Z. P. Bazant, “Physical Model for Steel Corrosion in Concrete Sea Structures - Application,” *ASCE J Struct Div*, vol. 105, no. 6, pp. 1155–1166, 1979.
- [49] O. B. Isgor and A. G. Razaqpur, “Advanced modelling of concrete deterioration due to reinforcement corrosion,” *Can. J. Civ. Eng.*, vol. 33, no. 6, pp. 707–718, 2006.
- [50] P. Ghods, O. B. Isgor, and M. Pour-Ghaz, “A practical method for calculating the corrosion rate of uniformly depassivated reinforcing bars in concrete,” *Mater. Corros.*, vol. 58, no. 4, pp. 265–272, 2007.
- [51] Y. A. Villagrán Zaccardi, J. F. García, P. Huélamo, and Á. A. Di Maio, “Influence of temperature and humidity on Portland cement mortar resistivity monitored with inner sensors,” *Mater. Corros.*, vol. 60, no. 4, pp. 294–299, 2009.
- [52] N. Otsuki, M. S. Madlangbayan, T. Nishida, T. Saito, and M. A. Baccay, “Temperature dependency of chloride induced corrosion in concrete,” *J. Adv. Concr. Technol.*, vol. 7, no. 1, pp. 41–50, 2009.
- [53] V. Živica, L. Krajči, L. Bágel, and M. Vargová, “Significance of the ambient temperature and the steel material in the process of concrete reinforcement corrosion,” *Constr. Build. Mater.*, vol. 11, no. 2, pp. 99–103, 1997.
- [54] M. Stefanoni, U. Angst, and B. Elsener, “Innovative Sample Design for Corrosion Rate Measurements in Carbonated Blended Concrete,” in *International Concrete Sustainability Conference*, 2016, pp. 1–12.
- [55] M. C. García-Alonso *et al.*, “Corrosion behaviour of innovative stainless steels in mortar,” *Cem. Concr. Res.*, vol. 37, no. 11, pp. 1562–1569, 2007.
- [56] *JIS G3132: Cold finished carbon and alloy steel bars*. Tokyo, Japan: Japanese Standard Association, 2018.
- [57] L. Cheng, I. Maruyama, and Y. Ren, “Novel accelerated test method for RH dependency of steel corrosion in carbonated mortar,” *J. Adv. Concr. Technol.*, vol. 19, no. 3, pp. 207–215, Mar. 2021.

## REFERENCE

- [58] L. B. Rockland, "Saturated Salt Solutions for Static Control of Relative Humidity between 5° and 40° C.," *Anal. Chem.*, vol. 32, no. 10, pp. 1375–1376, 1960.
- [59] "JSCE Standards 'Test Method for Electrical Resistivity of Concrete By Four Electrodes Method,'" *J. Japan Soc. Civ. Eng. Ser. E2 (Materials Concr. Struct.*, vol. 74, no. 4, pp. 260–274, 2018.
- [60] B. J. Christensen *et al.*, "Impedance Spectroscopy of Hydrating Cement-Based Materials: Measurement, Interpretation, and Application," *J. Am. Ceram. Soc.*, vol. 77, no. 11, pp. 2789–2804, 1994.
- [61] D. M. Bastidas, "Interpretation of impedance data for porous electrodes and diffusion processes," *Corrosion*, vol. 63, no. 6, pp. 515–521, 2007.
- [62] J. M. Bastidas, J. L. Polo, C. L. Torres, and E. Cano, "Study on the stability of AISI 316L stainless steel pitting corrosion through its transfer function," *Corros. Sci.*, vol. 43, no. 2, pp. 269–281, 2001.
- [63] M. . Stern, "Electrochemical Polarization, 1. A Theoretical Analysis of the Shape of Polarization Curves'," *J. Electrochem. Soc.*, vol. 104, no. 12, p. 751, 1957.
- [64] C. Alonso and C. Andrade, "Corrosion of steel reinforcement in carbonated mortar containing chlorides," *Adv. Cem. Res.*, vol. 1, no. 3, pp. 155–163, 1988.
- [65] J. E. B. Randles, "Kinetics of rapid electrode reactions," *Discuss. Faraday Soc.*, vol. 1, no. 13, p. 11, 1947.
- [66] W. John McCarter, G. Starrs, S. Kandasami, R. Jones, and M. Chrisp, "Electrode configurations for resistivity measurements on concrete," *ACI Mater. J.*, vol. 106, no. 3, pp. 258–264, 2009.
- [67] B. Edward and W. Washburn, "Note on a method of determining the distribution of pore size in porous material," *Proc. Nat. Acad. Sci.*, vol. 7, pp. 115–116, 1921.
- [68] A. C. A. Muller *et al.*, "Characterization of porosity & C-S-H in cement pastes by 1H NMR," *Ec. Polytech. Fed. Lausanne*, vol. 52, no. 3, p. 246, 2014.
- [69] A. C. A. Muller *et al.*, "Characterization of porosity & C-S-H in cement pastes by 1H NMR," in *Ecole Polytechnique Federale de Lausanne*, 2014, vol. 52, no. 3, p. 246.
- [70] V. G. Papadakis, C. G. Vayenas, and M. N. Fardis, "A reaction engineering

## REFERENCE

- approach to the problem of concrete carbonation,” *AIChE J.*, vol. 35, no. 10, pp. 1639–1650, 1989.
- [71] L. Black, C. Breen, J. Yarwood, K. Garbev, P. Stemmermann, and B. Gasharova, “Structural features of C-S-H(I) and its carbonation in air-A Raman spectroscopic study. Part II: Carbonated phases,” *J. Am. Ceram. Soc.*, vol. 90, no. 3, pp. 908–917, 2007.
  - [72] S. T. Pham and W. Prince, “Effects of Carbonation on the Microstructure of Cement Materials: Influence of Measuring Methods and of Types of Cement,” *Int. J. Concr. Struct. Mater.*, vol. 8, no. 4, pp. 327–333, 2014.
  - [73] M. Thiéry *et al.*, “Effect of carbonation on the microstructure and the moisture properties of cement-based materials,” *Int. Conf. Durab. Build. Mater. Components*, vol. 55, no. 1, pp. 1–8, 2011.
  - [74] L. G. Joyner, E. P. Barrett, and R. Skold, “The Determination of Pore Volume and Area Distributions in Porous Substances. II. Comparison between Nitrogen Isotherm and Mercury Porosimeter Methods,” *J. Am. Chem. Soc.*, vol. 73, no. 7, pp. 3155–3158, 1951.
  - [75] B. S. Brunauer and P. H. Emmett, “Adsorption of Gases in Multimolecular Layers,” no. 1c, 1938.
  - [76] N. Aschan, “Determining the setting time of cement paste, mortar and concrete with a copper-lead electrode,” *Mag. Concr. Res.*, vol. 18, no. 56, pp. 153–160, 1966.
  - [77] M. Nagao, K. Kobayashi, Y. Jin, I. Maruyama, and T. Hibino, “Ionic conductive and photocatalytic properties of cementitious materials: Calcium silicate hydrate and calcium aluminoferrite,” *J. Mater. Chem. A*, vol. 8, no. 30, pp. 15157–15166, 2020.
  - [78] C. A. J. Appelo, “The anion exchange properties of AFm (hydrocalumite-group) minerals defined from solubility experiments and crystallographic information,” *Cem. Concr. Res.*, vol. 140, p. 106270, 2021.
  - [79] R. von Helmholtz, “Investigations of vapors and mists, especially of such things from solutions,” *Ann. der Phys. und Chemie*, vol. 263, no. 4, pp. 508–543, 1886.
  - [80] O. E. Gjörv, V. Øystein, and A. H. S. El-Busaidy, “Electrical resistivity of

## REFERENCE

- concrete in the oceans,” in *Proceedings of the Annual Offshore Technology Conference*, 1977, pp. 581–588.
- [81] J. K. Su, C. C. Yang, W. B. Wu, and R. Huang, “Effect of moisture content on concrete resistivity measurement,” *J. Chinese Inst. Eng. Trans. Chinese Inst. Eng. A/Chung-kuo K. Ch'eng Hsueh K'an*, vol. 25, no. 1, pp. 117–122, 2002.
  - [82] A. Coyle, R. Spragg, A. Amirkhanian, and J. Weiss, “Measuring the Influence of Temperature on Electrical Properties of Concrete,” *Int. RILEM Conf. Mater.*, vol. 51, no. August, p. 626, 2016.
  - [83] C. Paper, F. Presuel, and Y. Liu, “Temperature Effect on Electrical Resistivity Measurement on Mature Saturated Concrete Conference,” no. January 2012, 2016.
  - [84] V.T.Ngala and C.L.Page, “Effects of Carbonation on Pore Structure and Diffusional Properties of Hydrated Cement Pastes,” *Cem. Concr. Res.*, vol. 27, no. 7, pp. 995–1007, 1997.
  - [85] E. G. Swenson and P. J. Sereda, “Mechanism of the carbonation shrinkage of lime and hydrated cement,” *J. Appl. Chem.*, vol. 18, no. 4, pp. 111–117, 1968.
  - [86] W. Nernst, “Die elektromotorische Wirksamkeit der Ionen,” *Zeitschrift für Phys. Chemie*, vol. 4, no. 1, pp. 129–181, 1889.
  - [87] M. A. Baccay, N. Otsuki, T. Nishida, and S. Maruyama, “Influence of cement type and temperature on the rate of corrosion of steel in concrete exposed to carbonation,” *Corrosion*, vol. 62, no. 9, pp. 811–821, 2006.
  - [88] N. Otsuki, S. Maruyama, T. Nishida, and B. M. Alibuyog, “Influence of Temperature on Corrosion Concrete Rate of Steel Bar in Carbonated Members,” *J.Soc.Mat.Sci.,Japan*, vol. 53, pp. 108–113, 2004.
  - [89] A. Alhozaimy, R. R. Hussain, R. Al-Zaid, and A. Al-Negheimish, “Coupled effect of ambient high relative humidity and varying temperature marine environment on corrosion of reinforced concrete,” *Constr. Build. Mater.*, vol. 28, no. 1, pp. 670–679, 2012.
  - [90] *Standard Practice for Preparing, Cleaning, and Evaluating Corrosion Test Specimens.*, vol. 90, no. Reapproved. 1999, pp. 1–8.
  - [91] C. Alonso, C. Andrade, and J. A. González, “Relation between resistivity and

## REFERENCE

- corrosion rate of reinforcements in carbonated mortar made with several cement types,” *Cem. Concr. Res.*, vol. 18, no. 5, pp. 687–698, 1988.
- [92] M. Stefanoni, U. Angst, and B. Elsener, “The mechanism controlling corrosion of steel in carbonated cementitious materials in wetting and drying exposure,” *Cem. Concr. Compos.*, vol. 113, no. July, p. 103717, 2020.
- [93] J. A. González and C. Andrade, “Effect of Carbonation, Chlorides and Relative Ambient Humidity on the Corrosion of Galvanized Rebars Embedded in Concrete,” *Br. Corros. J.*, vol. 17, no. 1, pp. 21–28, 1982.
- [94] E. Chávez-Ulloa, R. Camacho-Chab, M. Sosa-Baz, P. Castro-Borges, and T. Pérez-López, “Corrosion process of reinforced concrete by carbonation in a natural environment and an accelerated test chamber,” *Int. J. Electrochem. Sci.*, vol. 8, no. 7, pp. 9015–9029, 2013.
- [95] M. Saleem *et al.*, “Effect of moisture, chloride and sulphate contamination on the electrical resistivity of Portland cement concrete,” *Constr. Build. Mater.*, vol. 10, no. 3, pp. 209–214, 1996.
- [96] *Japanese Architectural Standard Specification for Reinforced Concrete Work, JASS5*. 2009.
- [97] *Standard specifications for concrete structures (2018)-Maintenance*. 2018.
- [98] S. Asamoto, J. Sato, S. Okazaki, P. J. Chun, R. Sahamitmongkol, and G. H. Nguyen, “The cover depth effect on corrosion-induced deterioration of reinforced concrete focusing on water penetration: Field survey and laboratory study,” *Materials (Basel)*, vol. 14, no. 13, 2021.
- [99] P. Duxson, J. L. Provis, G. C. Lukey, and J. S. J. van Deventer, “The role of inorganic polymer technology in the development of ‘green concrete,’” *Cem. Concr. Res.*, vol. 37, no. 12, pp. 1590–1597, 2007.
- [100] O. Kayali, M. S. H. Khan, and M. Sharfuddin Ahmed, “The role of hydrotalcite in chloride binding and corrosion protection in concretes with ground granulated blast furnace slag,” *Cem. Concr. Compos.*, vol. 34, no. 8, pp. 936–945, 2012.
- [101] V. G. Papadakis, “Effect of supplementary cementing materials on concrete resistance against carbonation and chloride ingress,” *Cem. Concr. Res.*, vol. 30, no. 2, pp. 291–299, 2000.

## REFERENCE

- [102] M. Thomas, “The effect of curing and concrete quality on the durability of concrete with high-volumes,” *UNB*, no. March, 2004.
- [103] T. H. Vu, N. Gowripalan, P. De Silva, P. Kidd, and V. Sirivivatnanon, “Carbonation and chloride induced steel corrosion related aspects in fly ash/slag based geopolymers - A critical review,” *FIB 2018 - Proc. 2018 fib Congr. Better, Smarter, Stronger*, no. October, pp. 3061–3076, 2019.
- [104] P. Termkhajornkit, T. Nawa, and K. Kurumisawa, “Effect of water curing conditions on the hydration degree and compressive strengths of fly ash-cement paste,” *Cem. Concr. Compos.*, vol. 28, no. 9, pp. 781–789, 2006.
- [105] R. ISHIKAWA, T. NAWA, and T. SAGAWA, “A study on validation of combined method of crystallization by heat treatment and quantitative XRD-Reitveld method for determining hydration degree of blast-furnace-slag in slag-blended cement,” *Cem. Sci. Concr. Technol.*, vol. 69, no. July, pp. 1–23, 2016.
- [106] M. Criado and J. L. Provis, “Alkali Activated Slag Mortars Provide High Resistance to Chloride-Induced Corrosion of Steel,” *Front. Mater.*, vol. 5, p. 34, 2018.
- [107] C. Tennakoon, A. Shayan, J. G. Sanjayan, and A. Xu, “Chloride ingress and steel corrosion in geopolymer concrete based on long term tests,” *Mater. Des.*, vol. 116, pp. 287–299, 2017.
- [108] K. Y. Yeau and E. K. Kim, “An experimental study on corrosion resistance of concrete with ground granulate blast-furnace slag,” *Cem. Concr. Res.*, vol. 35, no. 7, pp. 1391–1399, 2005.
- [109] S. Morinaga, “Durability design approach from the cause of deterioration,” *Durab. Des. Concr. Struct.*, vol. 26, no. 11, pp. 25–28, 1988.
- [110] C. Andrade, C. Alonso, and J. Sarfa, “Corrosion rate evolution in concrete structures exposed to the atmosphere,” *Cem. Concr. Compos.*, vol. 24, no. 1, pp. 55–64, 2002.
- [111] R. Rodrigues, S. Gaboreau, J. Gance, I. Ignatiadis, and S. Betelu, “Reinforced concrete structures: A review of corrosion mechanisms and advances in electrical methods for corrosion monitoring,” *Constr. Build. Mater.*, vol. 269, p. 121240, 2021.



## REFERENCE

- [112] C. Andrade, “Propagation of reinforcement corrosion: principles, testing and modelling,” *Mater. Struct. Constr.*, vol. 52, no. 1, pp. 1–26, 2019.
- [113] 岸谷孝一, 中性化. 1986.
- [114] *Japan architectural maintenance standard-6-RC.pdf*. JCI.
- [115] J. A. Gonzalez, W. Lopez, and P. Rodriguez, “Effects of moisture availability on corrosion kinetics of steel embedded in concrete,” *Corrosion*, vol. 49, no. 12, pp. 1004–1010, 1993.
- [116] 洋上田, “水の動きからみたコンクリート構造物のメンテナンス,” *RRR*, vol. 68, no. 4, pp. 22–25, 2011.
- [117] 福島敏夫, 鉄筋コンクリート造建築物の寿命. 1990.
- [118] *JCI Standard-DD1 Method of taking core samples from concrete structures*. Japan Concrete Institute.
- [119] *JCI A 1152 Method for measuring carbonation depth of concrete*. JCI.
- [120] 和泉意登志, “鉄筋コンクリート造建築物の耐久設計手法,” *Mater. life*, vol. 3, no. 3, pp. 147–152, 1991.
- [121] R. Du Plooy, S. Palma Lopes, G. Villain, and X. Dérobert, “Development of a multi-ring resistivity cell and multi-electrode resistivity probe for investigation of cover concrete condition,” *NDT E Int.*, vol. 54, pp. 27–36, 2013, doi: 10.1016/j.ndteint.2012.11.007.
- [122] J. Gulikers, R. Weidert, and M. Raupach, “RILEM TC 154-EMC : ELECTROCHEMICAL TECHNIQUES FOR MEASURING Test methods for on site measurement of resistivity of concrete Prepared by R . Polder , with contributions from C . Andrade , B . Elsener , O . Vennesland ,” *Corrosion*, vol. 33, pp. 603–611, 2001.
- [123] “Jsce Standards ‘Test Method for Electrical Resistivity of Concrete By Four Electrodes Method’土木学会規準「四電極法によるコンクリートの電気抵抗率試験方法（案）（Jsce-G 581-2018）」の制定,” *J. Japan Soc. Civ. Eng. Ser. E2 (Materials Concr. Struct.)*, vol. 74, no. 4, pp. 260–274, 2018.

## REFERENCE

- [124] Gulikers, J., Weidert, R., and Raupach, M., “RILEM TC 154-EMC : ELECTROCHEMICAL TECHNIQUES FOR MEASURING Test methods for on site measurement of resistivity of concrete,” *Mater. Struct. Constr.*, vol. 33, pp. 603–611, 2001.
- [125] P. Azarsa and R. Gupta, “Electrical Resistivity of Concrete for Durability Evaluation: A Review,” *Adv. Mater. Sci. Eng.*, vol. 2017, pp. 1–30, 2017.
- [126] A. Q. Nguyen, G. Klysz, F. Deby, and J. P. Balayssac, “Evaluation of water content gradient using a new configuration of linear array four-point probe for electrical resistivity measurement,” *Cem. Concr. Compos.*, vol. 83, pp. 308–322, 2017.
- [127] W. Wang and C. Lu, “Time-varying law of rebar corrosion rate in fly ash concrete,” *J. Hazard. Mater.*, vol. 360, no. July, pp. 520–528, 2018.
- [128] L. CHENG, “Effect of Moisture Content on Steel Corrosion in Concrete under Cyclic Wetting-and-drying,” the University of Tokyo, 2019.
- [129] L.Tang, “On chloride diffusion coefficients obtained by using the electrically accelerated methods,” in *1st RILEM workshop on Chloride Penetration into Concrete*, 1995, vol. 126, no. october, pp. 126–134.
- [130] A. Yosuke, M. Shinichi, N. Kyoji, Y. Kazuo, and M. Toyoaki, “Influence of chloride ion concentration and stress on steel corrosion in cement paste grout,” vol. 65, no. 1, pp. 103–117, 2009.
- [131] B. H. Oh, S. Y. Jang, and Y. S. Shin, “Experimental investigation of the threshold chloride concentration for corrosion initiation in reinforced concrete structures,” *Mag. Concr. Res.*, vol. 55, no. 2, pp. 117–124, 2003.
- [132] S. Y. Hong and F. P. Glasser, “Alkali binding in cement pastes : Part I. The C-S-H phase,” *Cem. Concr. Res.*, vol. 29, no. 12, pp. 1893–1903, 1999.
- [133] E. L’Hôpital, B. Lothenbach, K. Scrivener, and D. A. Kulik, “Alkali uptake in calcium alumina silicate hydrate (C-A-S-H),” *Cem. Concr. Res.*, vol. 85, pp. 122–136, 2016.
- [134] S. E. Benjamin, “Effect of temperature and ph on the binding of chloride by calcium aluminate,” in *Pakistan Engineering Congress, 70th Annual Session Proceedings*, 2006, no. 671, pp. 320–335.

## REFERENCE

- [135] H. Zibara, “Binding of solids Binding of Solids Binding of Solids,” University of Toronto, 2001.
- [136] T. Luping and L. O. Nilsson, “Chloride binding capacity and binding isotherms of OPC pastes and mortars,” *Cem. Concr. Res.*, vol. 23, no. 2, pp. 247–253, 1993.
- [137] D. B. McDonald, *Corrosion of Steel in Concrete Structures*. 2016.
- [138] S. J. Jaffer and C. M. Hansson, “Chloride-induced corrosion products of steel in cracked-concrete subjected to different loading conditions,” *Cem. Concr. Res.*, vol. 39, no. 2, pp. 116–125, 2009.
- [139] A. Köliö, M. Honkanen, J. Lahdensivu, M. Vippola, and M. Pentti, “Corrosion products of carbonation induced corrosion in existing reinforced concrete facades,” *Cem. Concr. Res.*, vol. 78, pp. 200–207, 2015.
- [140] U. Angst, B. Elsener, A. Jamali, and B. Adey, “Concrete cover cracking owing to reinforcement corrosion - Theoretical considerations and practical experience,” *Mater. Corros.*, vol. 63, no. 12, pp. 1069–1077, 2012.
- [141] J. A. Gonzalez and C. Andrade, “Effect of carbonation, chlorides and relative ambient humidity on the corrosion of galvanized rebarsembedded in concrete,” *Br. Corros. J.*, vol. 17, no. 1, pp. 21–28, 1982.
- [142] M. Moreno, W. Morris, M. G. Alvarez, and G. S. Duffó, “Corrosion of reinforcing steel in simulated concrete pore solutions effect of carbonation and chloride content,” *Corros. Sci.*, vol. 46, no. 11, pp. 2681–2699, 2004.